


August 2017

Interaction with Nitric Oxide of the Nitrosomonas Europaea Tetraheme Protein Cytochrome C554, and Two of Its Variants, in Increasingly Reducing Environments

Jennifer M. McGarry
University of Wisconsin-Milwaukee

Follow this and additional works at: <https://dc.uwm.edu/etd>

 Part of the [Biochemistry Commons](#), and the [Inorganic Chemistry Commons](#)

Recommended Citation

McGarry, Jennifer M., "Interaction with Nitric Oxide of the Nitrosomonas Europaea Tetraheme Protein Cytochrome C554, and Two of Its Variants, in Increasingly Reducing Environments" (2017). *Theses and Dissertations*. 1667.
<https://dc.uwm.edu/etd/1667>

This Dissertation is brought to you for free and open access by UWM Digital Commons. It has been accepted for inclusion in Theses and Dissertations by an authorized administrator of UWM Digital Commons. For more information, please contact open-access@uwm.edu.

**INTERACTION WITH NITRIC OXIDE OF THE
NITROSOMONAS EUROPAEA TETRAHEME PROTEIN
CYTOCHROME C554, AND TWO OF ITS VARIANTS, IN
INCREASINGLY REDUCING ENVIRONMENTS**

by

Jennifer M. McGarry

A Dissertation Submitted in
Partial Fulfillment of the
Requirements for the Degree of

Doctor of Philosophy
in Chemistry

at

The University of Wisconsin-Milwaukee

August 2017

ABSTRACT

INTERACTION WITH NITRIC OXIDE OF THE NITROSOMONAS EUROPAEA TETRAHEME PROTEIN CYTOCHROME C554, AND TWO OF ITS VARIANTS, IN INCREASINGLY REDUCING ENVIRONMENTS

by

Jennifer McGarry

The University of Wisconsin-Milwaukee, 2017
Under the supervision of Professor A. Andrew Pacheco

A re-investigation of the interaction with NO of the small tetraheme protein cytochrome *c*₅₅₄ (C₅₅₄) from *Nitrosomonas europaea* has shown that the 5-coordinate heme II of the 2-electron or 4-electron reduced protein will nitrosylate reversibly. The nitrosylation process was found to be first order in C₅₅₄, first-order in NO, and second-order overall. The rate constant for NO binding to the heme was determined to be $3000 \pm 140 \text{ M}^{-1}\text{s}^{-1}$, while the rate constant for dissociation was $0.034 \pm 0.009 \text{ s}^{-1}$; the degree of protein reduction does not appear to significantly influence the nitrosylation rate. In contrast to a previous report, [Upadhyay, A. K., et al. (2006), *J. Am. Chem. Soc.* 128, 4330-4337] this study turned up no evidence of C₅₅₄-catalyzed NO reduction, either with C₅₅₄²⁻ or with C₅₅₄⁴⁻. Some sub-stoichiometric oxidation of the lowest potential heme IV was detected when C₅₅₄⁴⁻ was exposed to an excess of NO, and this could in principle be part of a process that yields N₂O, though alternative explanations are equally plausible.

The vacant heme II site of C₅₅₄ is sterically crowded by three non-bonding hydrophobic amino acids, Thr 154, Pro 155 and Phe 156. Replacing Phe156 with a protonatable but still bulky histidine residue did not significantly alter the reactivity of the F156H mutant with NO, though the NO binding rate appeared to increase 10-fold. On the other hand, when Phe156 was

replaced with the smaller but still hydrophobic alanine, the 6-coordinate low-spin hemes of the 4-electron reduced mutant oxidized over the course of several minutes after exposure to NO. Two-electron reduced F156A²⁻ nitrosylated, but did not oxidize, upon exposure to NO. Notably, the nitrosylation rate for F156A²⁻ and F156A⁴⁻ was about 400× faster than for the wild type or for the F156H mutant, though the rate of the reverse denitrosylation process was almost the same for the three C₅₅₄ variants.

The midpoint potentials of C₅₅₄, and of the F156A and F156H variants, were determined for all the hemes in these tetraheme proteins, using spectropotentiometric analysis. The heme II midpoint potential of F156H was profoundly altered from the wild type value, shifting about 170 mV to the negative. This is taken as evidence that the histidine ligand in the variant binds to the erstwhile vacant ferric heme II axial site, thus stabilizing the oxidized state. Consistent with this interpretation, the UV/Visible spectrum of fully oxidized F156H exhibited increased absorbance at 409 nm relative to the wild type, which suggests that the mutant protein has 4 low-spin ferrihemes, rather than three low-spin and one high-spin as seen in the wild type. Upon reduction of heme II though, the spectrum of F156H exhibited a band at 430 nm characteristic of high-spin ferrohemes, which suggests that His156 dissociates from the heme when this reduces.

In contrast to the case with F156H, the midpoint potentials of hemes I and II in F156A were only slightly shifted relative to the wild type. On the other hand, the midpoint potentials of the low-potential hemes III and IV were shifted about 100 mV to the negative by mutating Phe156 to Ala, whereas mutation of Phe156 to His had minimal impact on these hemes. It appears that the substitution of bulky Phe by the small Ala significantly alters the conformation of the protein backbone, which in turn affects the environment of distant hemes enough to substantially alter their midpoint potentials. The lower heme III and IV midpoint potentials of

F156A, together with the increased solvent access to the heme II vacant site in this variant, may work together in changing its reactivity to bound NO. The more strongly reducing hemes could more readily reduce bound NO, while increased solvent access could now allow protonation to accompany reduction of the bound nitrogen moiety.

TABLE OF CONTENTS

Chapter	Page Number
1. Introduction.....	1
1.1. The nitrogen cycle and cytochrome <i>c₅₅₄</i> 's purported roles in it.....	1
1.2. Structure and properties of <i>N. europaea</i> C ₅₅₄	4
1.3. The reported interaction of <i>N. europaea</i> C ₅₅₄ with NO.....	9
1.4. The ecological importance of nitrite reduction path control.....	11
1.5. Nitric oxide reduction during dissimilatory denitrification.....	13
1.6. N ₂ O generation by way of nitric oxide – hydroxylamine comproportionation.....	16
1.7. Ammonification vs. denitrification.....	20
1.8. References.....	24
2. Spectropotentiometric analysis of cytochrome <i>c₅₅₄</i> and selected variants.....	33
2.1. Introduction.....	33
2.2. Materials and Methods.....	34
2.2.1. General materials.....	34
2.2.2. Protein purification and handling.....	35
2.2.3. UV-Vis spectropotentiometric titrations of C ₅₅₄ and its variants.....	37
2.3. Results.....	39
2.3.1. A spectropotentiometric study of wild type C ₅₅₄	39
2.3.2. A spectropotentiometric study of the F156A C ₅₅₄ mutant.....	43
2.3.3. A spectropotentiometric study of the F156H C ₅₅₄ mutant.....	50
2.4. Discussion.....	70
2.4.1. Wild type C ₅₅₄	53
2.4.2. F156A mutant of C ₅₅₄	56
2.4.3. F156H mutant of C ₅₅₄	59
2.5. Summary.....	60
2.6. References.....	62
3. The reaction of wild type cytochrome <i>c₅₅₄</i> , at various stages of reduction, with photo-generated nitric oxide.....	65

3.1. Introduction	65
3.2. Materials and Methods	66
3.2.1. General materials	66
3.2.2. General instrumentation	67
3.2.3. Protein handling	67
3.2.4. Laser-initiated time-resolved spectroscopic experiments.....	68
3.2.5. Data analysis.....	69
3.3. Results	70
3.3.1. The reaction of photo-generated NO with two-electron reduced C ₅₅₄	70
3.3.2. The reaction of photo-generated NO with four-electron reduced C ₅₅₄	76
3.4. Discussion	81
3.4.1. The reaction of photo-generated NO with two-electron reduced C ₅₅₄	81
3.4.2. The reaction of photo-generated NO with four-electron reduced C ₅₅₄	84
3.5. Summary	87
3.6. References	88
4. The reaction of the cytochrome <i>c</i> ₅₅₄ mutant F156A, at various stages of reduction, with photo-generated nitric oxide.....	92
4.1. Introduction	92
4.2. Materials and Methods	92
4.2.1. General materials	92
4.2.2. General instrumentation.	93
4.2.3. Protein handling.....	93
4.2.4. Laser-initiated time-resolved spectroscopic experiments.....	94
4.2.5. Denitrosylation stopped-flow experiments.....	94
4.2.6. Data analysis.....	94
4.3. Results	95
4.3.1. The reaction of photo-generated NO with two-electron reduced F156A	98
4.3.2 Stopped-flow investigation of C ₅₅₄ ²⁻ (NO) and F156A ²⁻ (NO) denitrosylation.	98
4.3.3. The reaction of photo-generated NO with four-electron reduced F156A.....	106
4.4. Discussion	106
4.4.1. The reaction of photo-generated NO with two-electron reduced F156A.....	106

4.4.2. The reaction of photo-generated NO with four-electron reduced F156A.	107
4.5. Summary	108
4.6. References	109
5. The reaction of the cytochrome C ₅₅₄ mutant F156H, at various stages of reduction, with photo-generated nitric oxide.....	112
5.1. Introduction	112
5.2. Materials and Methods.....	112
5.2.1. General materials.....	112
5.2.2 General instrumentation	112
5.2.3 Protein handling.....	112
5.2.4. Experiments with DEANO-generated NO.	114
5.2.5. Laser-initiated time-resolved spectroscopic experiments.....	115
5.2.6. Data analysis.....	115
5.3. Results	115
5.3.1. Net reaction of NO with two-electron reduced F156H.	115
5.3.2. Net reaction of NO with one-electron reduced F156H.....	116
5.3.3. The reaction of photo-generated NO with one-electron reduced F156H.	117
5.3.4. The reaction of photo-generated NO with four-electron reduced F156H.	120
5.4. Discussion	123
5.4.1. The reaction of NO with one and two-electron reduced F156H	123
5.4.2. The reaction of photo-generated NO with four-electron reduced F156H.	124
5.5. Summary	125
5.6. References	109
6. Conclusions.....	126

Appendices

1. Supplementary material to chapter 2	129
A1.1 Spectropotentiometric analysis for a generic four heme system.....	129
A1.1.1. Derivation of Equation 2.8.	129
A1.1.2. Beer's law for difference spectra.....	130

A1.2. Special case: wild type C ₅₅₄	132
A1.2.1. Derivation of the Nernstian equations in exponential form.....	132
A1.2.2. Beer's law for difference spectra.....	133
A1.3. References	134
2. Supplementary Material for Chapter 3	135
A2.1 Derivation of rate law for C5542- nitrosylation.....	135
A2.2 Derivation of ϵ^0_{cell} for Scheme 3.3.....	139
Curriculum Vitae.....	142

LIST OF FIGURES

Figure 1.1. The biological nitrogen cycle, with the reactions discussed in this chapter highlighted in red. Abbreviations: AMO, ammonia mono-oxygenase; HAO, hydroxylamine oxidase; ccNiR, cytochrome *c* nitrite reductase; Nir, nitrite reductase; NOR, nitric oxide reductase.....1

Figure 1.2. Proposed pathway for ammonia oxidation to nitrite, catalyzed by HAO and AMO. The substrates and products are shown in blue, the electron flow in green. C₅₅₄ is believed to transfer electrons from HAO to membrane-bound cytochrome *c*_{m552} two at a time, after which the electrons enter the membrane-associated quinone pool. Note that two electrons ultimately end up at terminal oxidases, but the other two are needed for the AMO process.....3

Figure 1.3. Typical *c*-heme, showing the covalent attachments to cysteine residues and bis-histidine coordination to the iron center. Notice that one of the histidines is adjacent to one of the cysteines, forming part of a characteristic C-X-Y-C-H motif.....5

Figure 1.4. (a) Arrangement of the hemes within C₅₅₄, with the midpoint potentials reported in ref. ⁷. The numbering system is that used in in the text. (b) The hemes in relation to the surrounding protein6

Figure 1.5. (a) The vacant site of heme II, with the bulky Thr154, Pro155, Phe156 labeled. Note that the iron is pulled out of the heme plane in the opposite direction by the histidine ligand. (b) Same as (a), but with Thr154, Pro155, and Phe156 rendered in space-filling model.....7

Figure 1.6. Proposed steps in the cNOR-catalyzed reduction of NO to N₂O.....15

Figure 1.7. Proposed steps in the cyt P460-catalyzed comproportionation of NO and NH₂OH. This comproportionation is often known as the “hydroxylamine pathway” for N₂O formation in AOB.....18

Figure 1.8. Proposed steps in the fungal cyt P450_{nor}-catalyzed comproportionation of NO and NH₂OH. Note the similarities with the scheme proposed in Fig. 1.7 for the bacterial P460 enzyme. In both cases the primary mechanistic evidence is spectroscopic, but it is easy to imagine that the enzymes and proposed mechanisms could switch depending on reaction conditions.....19

Figure 1.9. Schematic view of the putative activation barrier that makes enzyme-catalyzed reduction of hydroxylamine to ammonia slow, unless an overpotential is supplied to overcome it.....22

Figure 2.1. UV-Vis extinction coefficient spectra for wild-type C₅₅₄, and for the F156A and F156H mutants. The values at the 406 nm maximum were determined to be 3.97×10⁵ M⁻¹cm⁻¹ for wild type C₅₅₄, 3.81×10⁵ M⁻¹cm⁻¹ for F156A, and 5.00×10⁵ M⁻¹cm⁻¹ for F156H, by cross-reference to a pyridine heme assay (see text for details).....37

Figure 2.2. UV/Vis cell used for the spectropotentiometric titration of C₅₅₄ and its variants. The quartz cuvette is a short pathlength (nominally 0.2 mm) demountable flow cell available commercially from Starna. The optically transparent gold mesh was obtained from Precision E-Forming, was sandwiched between the cuvette plates, and was connected to a copper wire using a conductive silver-containing glue (from GC Electronics). The edges of the cuvette were sealed with silicone adhesive (RTV108, Momentive). The cuvette could be filled from its lower filling port using a syringe. A small cup connected to the upper port by silicone tubing was partially filled with the protein solution, and provided a spot where the reference and auxiliary electrodes could make electrical contact. The actual pathlength of the cell with the gold foil in place was determined using a cytochrome *c* solution of known concentration. Note: for very long experiments the cup at the top should be covered to minimize evaporation of the protein solution.....38

Figure 2.3. (a) SVD-processed difference spectra obtained for 100 μM wild-type C₅₅₄ at applied potentials of 122, 102, 92, 82, 62, 42, 22, 2, -118, -178, -218, -258, -298, -358 mV versus the standard hydrogen electrode (SHE). Solid blue lines show the experimental data, whereas the dashed red lines show the calculated fits obtained using Eqs. 2.1 – 2.3. (b) A slice through the spectra from (a) taken at 424 nm, where the biggest changes in absorbance were observed; the solid blue trace represents the experimentally obtained data, the dashed red one the least-squares best fit using Eqs.2.1-2.3.....41

Figure 2.4. (a) Extinction coefficient difference spectra obtained by fitting the Fig. 2.3 data using Eqs. 2.1 – 2.3. (b) Absolute extinction coefficient spectra obtained by adding Δε_{HP} and Δε_{LP} to the previously obtained extinction coefficient spectrum of fully oxidized C₅₅₄ (Fig. 2.1).....43

Figure 2.5. (a) SVD-processed difference spectra obtained for 60.8 μM of the F156A C₅₅₄ mutant at applied potentials of 92, 72, 52, 32, 12, -8, -28, -48, and -68 mV versus SHE. Solid blue lines show the experimental data, whereas the dashed red lines show the calculated fits obtained using Eqs 2.4 and 2.5. (b) A slice through the spectra from (a) taken at 430 nm, where absorbance changes due to the high-spin 5-coordinate heme predominate. The solid blue trace represents the experimentally obtained data, the dashed red one the least-squares best fit using Eqs. 2.4 and 2.5.....45

Figure 2.6. (a) Extinction coefficient difference spectra associated with formation of C₁ and C₂ (Scheme 2.2), obtained by fitting the Fig. 2.5 data using Eqs. 2.4 and 2.5. (b) Absolute extinction coefficient spectra of C₁ and C₂, obtained by adding $\Delta\epsilon_1$ and $\Delta\epsilon_2$ to the previously obtained extinction coefficient spectrum of fully oxidized F156A C₅₅₄ mutant (Fig. 2.1).....46

Figure 2.7. (a) SVD-processed difference spectra obtained for 60.5 μM of the F156A C₅₅₄ mutant at applied potentials of -80 (flat line), -120, -160, -200, -240, -280, -320, -400, and -480 mV versus SHE. Solid blue lines show the experimental data, whereas the dashed red lines show the calculated fits obtained using Eqs 2.6 and 2.7. (b) A slice through the spectra from (a) taken at 423 nm, where largest absorbance changes are observed. The solid blue trace represents the experimentally obtained data, the dashed red one the least-squares best fit using Eqs. 2.6 and 2.7.....48

Figure 2.8. (a) Extinction coefficient difference spectra associated with formation of C₃ and C₄ of F156A (Scheme 2.3), obtained by fitting the Fig. 2.7 data using Eqs. 2.6 and 2.7. (b) Absolute extinction coefficient spectra of C₃ and C₄, obtained by adding $\Delta\epsilon_3$ and $\Delta\epsilon_4$ to ϵ_2 (shown in Fig. 2.6b).....49

Figure 2.9. Fractional abundance of each reduced F156A species as a function of applied potential, calculated using Eqs. 2.4 and 2.6, and the midpoint potential parameter set from Table 2.2. Based on the calculations, the 2-electron reduced species will constitute ~94% of the total C₅₅₄ at $\epsilon_{app} = -80$ mV, with the remaining 6% being 1-electron reduced.....50

Figure 2.10. (a) SVD-processed difference spectra obtained for 52 μM of the F156H C₅₅₄ mutant at applied potentials of 38.5, -2.5, -122.5, -162.5, -202.5, -242.5, -285.5, -322.5, -362.5 and -482.5 mV versus SHE. Solid blue lines show the experimental data, whereas the dashed red lines show the calculated fits obtained using Eqs 2.8 and 2.9. (b) A slice through the spectra from (a) taken at 424 nm, where the largest absorbance changes are observed. The solid blue trace represents the experimentally obtained data, the dashed red one the least-squares best fit using Eqs. 2.8 and 2.9.....51

Figure 2.11. (a) Extinction coefficient difference spectra associated with formation of $C_1 - C_4$ of F156H (Scheme 2.4), obtained by fitting the Fig. 2.10 data using Eqs. 2.8 and 2.9. (b) Absolute extinction coefficient spectra of $C_1 - C_4$, obtained by adding $\Delta\epsilon_1 - \Delta\epsilon_4$ to the mutant's ϵ_{ox} spectrum. Note that the split Soret seen in the Fig. 2.4a and 2.8a difference spectra are not seen in (a) above. This is because $\Delta\epsilon_3$ and $\Delta\epsilon_4$ in this case are obtained by subtraction of the fully oxidized spectra, whereas in the earlier cases the reduced difference spectra were relative to partially reduced intermediates.....53

Figure 3.1. (a) Spectral changes at selected times observed when a solution initially containing 0.9 mM of the NO generating species **1**, 6 μM C_{554} and 200 μM $\text{Ru}(\text{NH}_3)_6^{2+}$ was exposed to a 500 nm, 5 ns laser pulse, which fragments **1** to release NO. The purple traces track the first 1500 ms at 100 ms intervals, the blue traces are at one-second intervals, the orange traces are at two-second intervals, and the green traces are at 10-second intervals. The red traces are the least-squares best fits using Eq. 3.1. (b) Changes in absorbance vs time are plotted for 415 nm, 430 nm and 500 nm, where individual species make significant contributions; the red traces are from the least-squares best fits using Eq. 3.1.....71

Figure 3.2. The spectral components Λ_0 - Λ_2 generated by fitting the SVD-processed Fig. 3.1 data to Eq 3.1(blue traces). The red traces were generated with the independently known extinction coefficient spectrum of species **1** and small admixtures of Λ_1 . From the fit of Λ_0 (a) one can calculate that 31 μM of NO were generated by the laser pulse in this experiment. The fit of Λ_2 (c) mainly reflects the amount of **1** photolyzed per second due to the spectrophotometer probe beam; the NO so generated then nitrosylates additional C_{554}72

Figure 3.3. Plot of k_{obs} associated with appearance of the exponential component Λ_1 (Eq. 3.1), versus NO concentration obtained by fitting the corresponding t_0 component Λ_0 . Red trace: least-squares fit of the data to a straight line (Eq. 3.2). Slope = $3000 \pm 140 \text{ M}^{-1}\text{s}^{-1}$; Intercept = $0.034 \pm 0.009\text{s}^{-1}$; these are assigned as k_{on} and k_{off} , respectively as defined in Scheme 3.2 and Eq. 3.2.....74

Figure 3.4. Blue circles: $\Lambda_{1(415)} - \Lambda_{1(433)}$ differences obtained from the Λ_1 components, plotted against the NO concentrations obtained by fitting the corresponding t_0 components Λ_0 (see text for details). The red and green traces were least-squares best fits to Eq. 3.4. For the red trace the value of K_{eq}^{-1} was fixed using the k_{-1}/k_1 ratio obtained from the Fig. 3.3 fit to Eq. 3.2, while for the green trace both K_{eq}^{-1} and $\Delta\Lambda_{1max}$ in Eq. 3.4 were treated as adjustable parameters.....76

Figure 3.5. (a) Spectral changes at selected times observed when a solution initially containing 0.75 mM of the NO generating species **1**, 4 μM C_{554} and 3 μM MV_{red} was exposed to a 500 nm, 5 ns laser pulse which fragments **1** to release NO. The purple traces are at 100-ms intervals for the

first 1000 ms, the blue traces are at one-second intervals, and the green traces are at 10-second intervals. The red traces are the least-squares best fits using Eq. 3.5. (b) Changes in absorbance vs time are plotted for 398 nm, 409 nm, 420 nm, 434 nm and 500 nm, where individual species make significant contributions; the red traces are from the least-squares best fits using Eq. 3.5....77

Figure 3.6. The spectral components Λ_0 - Λ_3 generated from the cleaned SVD absorbance matrix when fit to Eq. 3.5 (blue traces). The red traces in (a) and (b) were fit with the known extinction coefficient of species **1** and small admixtures of Λ_1 from Fig. 3.2b. The red trace in (d) was fit with the known extinction coefficient spectrum for MV_{red} . The red trace in (c) was fit with the difference spectrum $\Delta\epsilon_\lambda = \epsilon_{red\lambda} - \epsilon_{ox\lambda}$ obtained in Section 2.3.1.....79

Figure 4.1. Blue trace: Spectral change observed immediately (within 16 ms) after a solution initially containing approximately 900 μM of the NO generating species **1**, 5 μM F156A and 200 μM $Ru(NH_3)_6^{2+}$ was exposed to a 500 nm, 5 ns laser pulse, which fragments **1** to release NO. Red trace: least-squares best fit using the independently known extinction coefficient spectrum of **1** and the extinction coefficient difference spectrum for wild type C_{554}^{2-} nitrosylation obtained as described in Chapter 3. From the fit one can estimate that the laser pulse photogenerated about 48 μM NO.....95

Figure 4.2. Change in absorbance at 430 nm over 1 s observed after a solution initially containing 12 μM F156A, 200 μM $Ru(NH_3)_6^{2+}$ and 48 μM of the NO generating species **1** was irradiated with a 500 nm, 5 ns laser pulse. Red trace: least-squared best fit to an exponential function.....96

Figure 4.3. Blue circles: plot of k_{obs} associated with the exponential absorbance decrease at 430 nm vs $F156A^{2-}$ concentration. Red trace: least-squares fit of the data to a straight line (Eq. 4.1). Slope = $(1.23 \pm 0.09) \times 10^6 M^{-1}s^{-1}$; Intercept = $0.5 \pm 1 s^{-1}$. Note that the intercept is zero within the precision of the measurement.....97

Figure 4.4. (a) Blue trace: change in absorbance at 430 nm observed after a solution initially containing 2.1 μM wild type $C_{554}^{2-}(NO)$ was mixed by stopped-flow with a second solution containing 200 μM of the NO trapping compound $[Ru(EDTA)OH_2]^-$. Red trace: least-squares fit of the data with a two-exponential function. (b) Similar to (a), but syringe 1 contained 1.5 μM nitrosylated F156A instead of wild type protein. In both cases the concentration of $[Ru(EDTA)OH_2]^-$ was sufficient to remove free NO as well as NO being released from nitrosylated protein.....100

Figure 4.5. (a) Spectral changes at selected times observed when a solution initially containing 0.57 mM of the NO generating species **1**, 7 μM F156A and 3 μM MV_{red} was exposed to a 500 nm, 5 ns laser pulse which fragments **1** to release NO. The purple traces are representative of the first

second, the blue traces are taken at 1-s intervals, and the green ones at 10-s intervals. The red traces are the least-squares best fits using Eq. 4.3. (b) Changes in absorbance vs time at the representative wavelengths stated, with the least-squares best fits using Eq. 4.3 overlaid as red traces.....102

Figure 4.6. The spectral components Λ_0 - Λ_2 generated from the SVD-cleaned absorbance matrix when fit to Eq. 4.3 (blue traces). The red traces in (a) were fit with the known extinction coefficient of species **1** and the extinction coefficient difference spectrum of F156A²⁻(NO), obtained by analyzing nitrosylation of the 2-electron reduced protein. The red trace in (c) was fit with the F156A²⁻(NO) extinction coefficient difference spectrum, and admixtures of the $\Delta\epsilon_3$ and $\Delta\epsilon_4$ extinction coefficient difference spectra obtained for the low potential hemes III and IV of F156A by UV/Vis spectropotentiometry (Section 2.3.2).....104

Figure 4.7. Plot of the first 10 (black trace) and first 50 (green trace) averaged SVD-cleaned spectra after the laser pulse from experiment shown in Fig 4.5a.....105

Figure 5.1. (a) Black trace: spectrum of 1 μ M F156H reduced by two electrons with 30 μ M indigo carmine; red trace: after the two-electron reduced F156H is exposed to 40 μ M NO. (b) The difference spectrum obtained by subtracting the black trace from the red trace from (a).....115

Figure 5.2. (a) Black trace: spectrum of 1 μ M F156H reduced by one electron with 200 μ M Ru(NH₃)₆²⁺; red trace: after the one-electron reduced F156H is exposed to 40 μ M NO. (b) The difference spectrum obtained by subtracting the black trace from the red trace from (a).....116

Figure 5.3. (a) Spectral changes observed when a solution initially containing 0.3 mM of the NO generating species **1**, 5 μ M F156H and 25 μ M indigo tetrasulfonate reduced at a potential of -70 mV vs SHE, was exposed to a 500 nm, 5 ns laser pulse which fragments **1** to release NO. The purple traces are representative of the first second, the blue traces are taken at 1-s intervals, and the green ones at 10-s intervals. The red traces are the least-squares best fits using Eq. 5.1. (b) Changes in absorbance vs time at the representative wavelengths stated, with the least-squares best fits using Eq. 5.1 overlaid as red traces.....118

Figure 5.4. The spectral components Λ_0 - Λ_2 generated from the SVD-cleaned absorbance matrix when fit to Eq. 5.1 (blue traces). The red traces in (a) were fit with the known extinction coefficient of species **1**. The red trace in (c) was fit with the known extinction coefficient spectra of species **1** and admixtures of Λ_0 and Λ_1119

Figure 5.5. (a) Spectral changes observed when a solution initially containing 0.1 mM of the NO generating species **1**, 3 μ M F156H and 3 μ M of Zn-reduced methyl viologen was exposed to a 500 nm, 5 ns laser pulse which fragments **1** to release NO. The purple traces are representative of the first second, the blue traces are taken at 1-s intervals, and the green ones at 20-s intervals. The red traces are the least-squares best fits using Eq. 5.1. (b) Changes in absorbance vs time at the representative wavelengths stated, with the least-squares best fits using Eq. 5.1 overlaid as red traces.....121

Figure 5.6. The spectral components Λ_0 - Λ_2 generated from the SVD-cleaned absorbance matrix when fit to Eq 5.1 (blue traces). The red trace in (a) is a fit with the known extinction coefficient of species **1**. The red trace in (b) is a fit with 4-3 electron reduced extinction coefficient spectrum obtained by UV/Vis spectropotentiometry (Chapter 2).....122

LIST OF TABLES

Table 2.1. Mediators used for spectropotentiometry.....	34
Table 2.2. Midpoint potentials of wild type and variant C ₅₅₄ hemes (in volts vs. the standard hydrogen electrode) obtained in this work, and in previous investigations.....	54

LIST OF SCHEMES

Scheme 1.1. Fe-NO species is represented in terms of two resonance structures, depicted by the corresponding Enemark-Feltham description $\{\text{Fe}(\text{NO})\}^n$. In this notation, the superscript n is the sum of the d electrons from the Fe, and the π^* electrons from the NO moiety ⁶	10
Scheme 1.2.....	13
Scheme 1.3. Energetics of hydroxylamine disproportionation.....	21
Scheme 2.1. Reduction of fully oxidized wild type C ₅₅₄ (<i>Ox</i>) to the apparently 3-electron reduced form (<i>C</i> ₃) in 1-electron steps (see text for details).....	40
Scheme 2.2. First two steps in the reduction of fully oxidized F156A mutant (<i>Ox</i>) in 1-electron steps.....	41
Scheme 2.3. Reduction of 2-electron reduced F156A mutant (<i>C</i> ₂) to the 4-electron reduced moiety (<i>C</i> ₄) in 1-electron steps.....	47
Scheme 2.4. Reduction of fully oxidized F156H mutant (<i>Ox</i>) to the 4-electron reduced moiety in 1-electron steps.....	52
Scheme 3.1. Photolytic cleavage of 1 to produce an aquo species and free NO.....	66
Scheme 3.2. Equilibrium between two-electron reduced C ₅₅₄ and its nitrosylated form.....	81
Scheme 3.3. One proposed mechanism for the reaction of NO with fully reduced C ₅₅₄ . IET, intramolecular electron transfer.....	85
Scheme 3.4. An alternative mechanism for the reaction of NO with fully reduced C ₅₅₄ , which allows for sub-stoichiometric production of N ₂ O. Note that free nitroxyl anion is expected to be in the triplet state ^l	87

Scheme 4.1.	98
Scheme 4.2.	98
Scheme 4.3.	108
Scheme 5.1. Red is the reducing agent present in excess, $\text{Ru}(\text{NH}_3)_6^{2+}$ or reduced indigo tetrasulfonate.....	117

ACKNOWLEDGMENTS

I would like to thank Karl Koebke for his work on the NO generator and his general willingness to discuss any experiment at length, Matthew Youngblut for teaching me everything he knows about molecular biology and continuing support, and Josh Kostera for helping me in my first years. A special thanks to all the undergraduate students whom I have worked with over the years, especially David Koltermann, and Jason Van Roo for his work on creating the C₅₅₄ mutants. Thank you to several University of Wisconsin-Milwaukee professors: Prof. Marius Schmidt for his support during my undergraduate degree, Prof. Joeseeph Aldstadt for helping with continuous culture set up, Prof. Nicholas Silvaggi for use of his lab's centrifuge and Fast Protein Liquid Chromatography system, Prof. Graham Moran for use of his lab's stopped-flow system and Prof. Dennis Bennett for serving on my committee. Thank you to Prof. John Coats from University of California-Berkeley for sharing the WM3064 cells. Finally, thank you to my advisor Prof. A. Andrew Pacheco who is the best mentor ever.

I am grateful for funding from the University of Wisconsin Milwaukee's Research and Growth initiative and the National Science Foundation under grants MCB 1121770, MCB 1330809 and MCB 1616824.

Lastly, I would like to thank my family and friends who have supported me throughout my graduate career particularly, Connor Sperry.

Chapter 1

Introduction

1.1. The nitrogen cycle and cytochrome *c554*'s purported roles in it

Nitrogen is an essential element to all forms of life. However, the vast majority of terrestrial nitrogen (79% of air) is in the form of dinitrogen, which is inert and unusable to most organisms. Specialized microorganisms called “nitrogen fixing” bacteria and archaea are capable of converting nitrogen to ammonia (Fig. 1.1), and until the Haber-Bosch process was developed in the early 20th century, this was the only significant route by which nitrogen could become bioavailable to the vast majority of life forms.¹⁻⁵

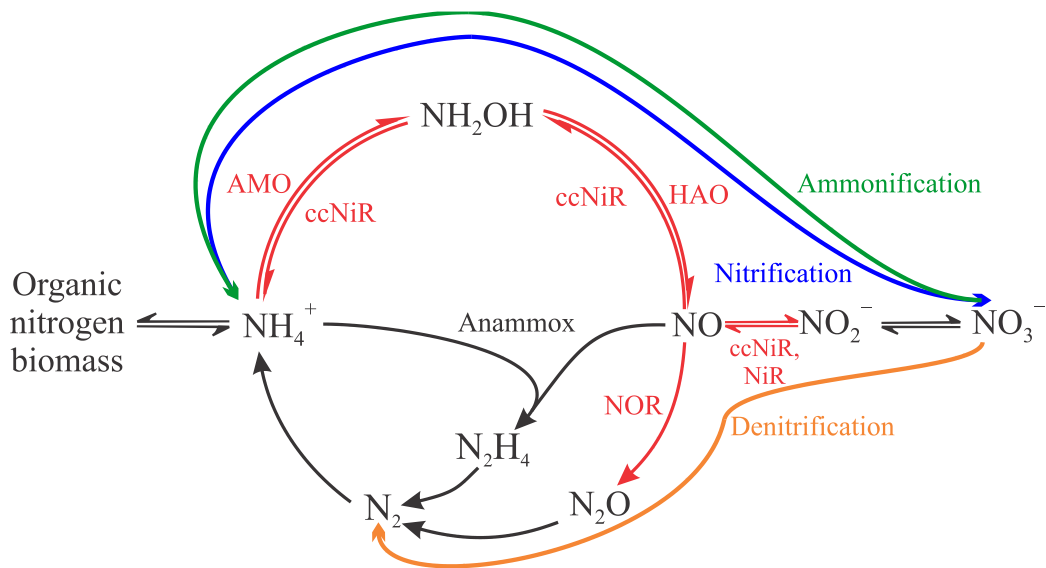


Figure 1.1. The biological nitrogen cycle, with the reactions discussed in this chapter highlighted in red. Abbreviations: AMO, ammonia mono-oxygenase; HAO, hydroxylamine oxidase; ccNiR, cytochrome *c* nitrite reductase; Nir, nitrite reductase; NOR, nitric oxide reductase.

Once ammonia has been generated it is readily interconverted with a variety of other so-called “reactive nitrogen” species, as shown in Fig. 1.1. Ammonia oxidizing microbes use ammonia as an electron source in aerobic respiration, generating nitrite in the process. Nitrite in turn can be oxidized to nitrate by nitrite oxidizers, a separate group of aerobically respiring bacteria. The net conversion of ammonia to nitrate is known as nitrification. In the absence of air nitrate and nitrite can act as electron acceptors for many anaerobically respiring microbes. Nitrite reduction can take two paths. Denitrifying microbes close the nitrogen cycle loop by reducing nitrite stepwise back to dinitrogen, generating nitric oxide and nitrous oxide as isolable intermediates. Nitrite ammonifiers reduce nitrite to ammonia in one single 6-electron step, with no release of intermediates.¹⁻⁵ In one other respiratory process, known as “anammox”, certain microorganisms can extract energy from the comproportionation of ammonia and nitrite. Hydrazine is an intermediate in this process.^{8, 9}

It should be noted that plants can also reduce nitrite and nitrate to ammonia. In this case nitrate and nitrite are not being used as electron sinks in respiration, but rather as sources of biomass nitrogen. Thus, although nitrogen-fixing microbes provide the only natural entry point to reactive nitrogen, nitrate initially generated from fixed ammonia by ammonia oxidizers is an important store of biomass nitrogen in the biosphere. Nitrite reduction as a respiratory process is sometimes referred to as “dissimilatory”, while nitrite reduction to generate biomass is known as “assimilatory”.^{3, 5}

The protein cytochrome *c₅₅₄* (C₅₅₄) that is the subject of this dissertation is an electron transport protein from the ammonia oxidizing bacterium *Nitrosomonas europaea*. In ammonia oxidizers such as *N. europaea* ammonia oxidation to nitrite is a two-step process (Figs. 1.1, 1.2). In the first step, catalyzed by the enzyme ammonia monooxygenase (AMO), ammonia is

oxidized to hydroxylamine, a process that is coupled with reduction of dioxygen to water. In the second step, catalyzed by hydroxylamine oxidase (HAO), hydroxylamine is oxidized by four electrons to nitrite. It has been proposed that C₅₅₄ accepts the electrons released from hydroxylamine oxidation two at a time, and passes them on to cytochrome *c*_{m552}, an electron transporter anchored to the periplasmic side of the cytoplasmic membrane (Fig. 1.2).^{10, 11}

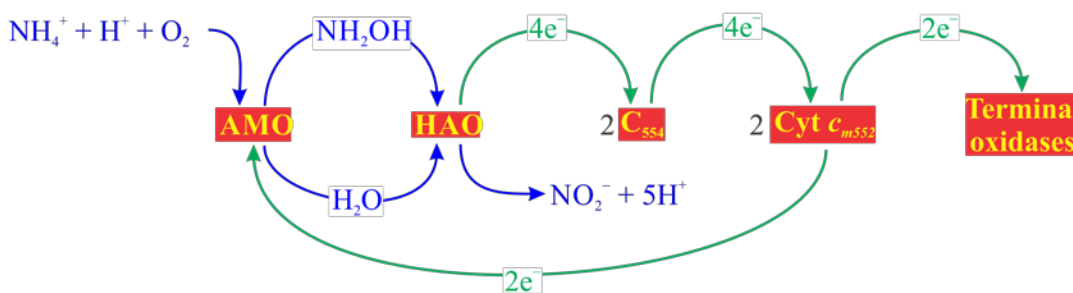


Figure 1.2. Proposed pathway for ammonia oxidation to nitrite, catalyzed by HAO and AMO. The substrates and products are shown in blue, the electron flow in green. C₅₅₄ is believed to transfer electrons from HAO to membrane-bound cytochrome *c*_{m552} two at a time, after which the electrons enter the membrane-associated quinone pool. Note that two electrons ultimately end up at terminal oxidases, but the other two are needed for the AMO process.

Until eleven years ago C₅₅₄ was assumed to be purely an electron transport protein as just described. However, in 2006 Upadhyay and coworkers published a paper in which they reported that C₅₅₄ was capable of binding nitric oxide and catalytically reducing it to nitrous oxide,⁷ which raised the prospect of an ancillary role as an NO reductase for the protein. Exploration of this possibility was the major objective of the project described herein.

We became interested in C₅₅₄'s purported NO reductase activity for two reasons. At the most fundamental level we were curious about the reaction mechanism, which would have to be

very different from that of NO reductases from denitrifying bacteria, given that these are structurally very different from C₅₅₄. The basic mechanistic question also led us to wonder about the factors that determine the direction of nitrate and nitrite reduction in the nitrogen cycle. As can be seen in Fig. 1.1, NO sits at the branch point for two reduction options, back to dinitrogen by way of the denitrification pathway, or to ammonia via ammonification. The fact that a protein as simple as C₅₅₄, with a very small hydrophobic binding pocket, could catalyze NO reduction to N₂O, raised the possibility of using the protein as a simple model for probing the structural factors that determine the direction taken at the branch point. For example, if C₅₅₄ could be tailored to reduce NO to either N₂O or NH₄⁺ simply by making judicious changes to the NO binding pocket, this could provide valuable mechanistic information. What makes such an idea particularly attractive is the fact that the mechanisms of nitrification and ammonification enzymes are already a central area of study for the Pacheco research group. Section 1.7 briefly returns to the NO branch point question; however, the scope of the dissertation is narrower, focusing strictly on better understanding C₅₅₄'s basic interactions with NO. The ecological importance of NO reduction, and of reactive nitrogen species control in general, is further discussed in Sections 1.4 – 1.6. Sections 1.2 and 1.3, immediately below, provide an overview of C₅₅₄'s structure and chemical properties, as they are currently understood.

1.2. Structure and properties of *N. europaea* C₅₅₄

C₅₅₄ is a small (26 kDa) monomeric soluble periplasmic protein containing four *c*-type hemes. The protein derives its name from a characteristic absorbance band at 554 nm that appears in the UV/Vis spectrum of the reduced state.¹² Reduced *c*-type hemes typically have a band, referred to as the α -band, in the region around 550 nm, and it is fairly common to name the proteins according to the exact wavelength of this band. C₅₅₄ has a very different amino acid

sequence from other *c*-type hemes, including other tetrahemes, and is considered to be in its own class.¹³

As is characteristic of *c*-hemes, each of the four hemes of C₅₅₄ is attached to the protein by two thioether linkages with cysteines that have a characteristic binding motif C-X-Y-C-H (Fig. 1.3). In this motif, the histidine residue that ends the sequence is one of the heme axial ligands (Fig. 1.3). As shown in Fig. 1.4, three hemes (I, III, and IV) are six-coordinate with bis-

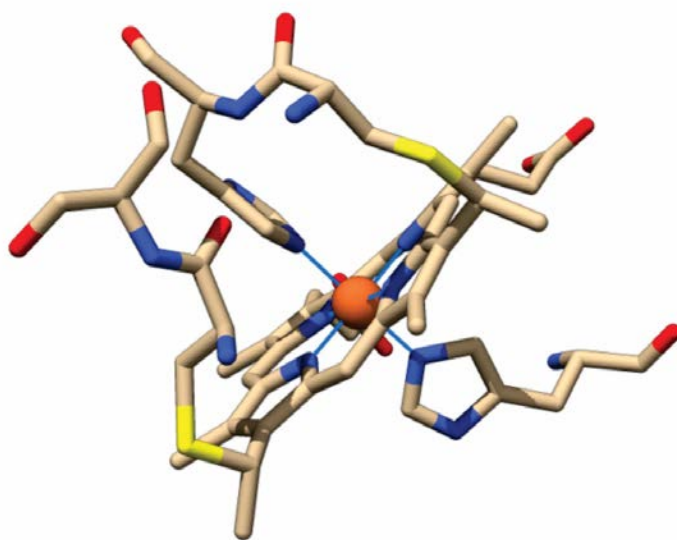


Figure 1.3. Typical *c*-heme, showing the covalent attachments to cysteine residues and bis-histidine coordination to the iron center. Notice that one of the histidines is adjacent to one of the cysteines, forming part of a characteristic C-X-Y-C-H motif.

histidine axial ligation, while the fourth (heme II in Fig. 1.4) is five-coordinate with a single histidine axial ligand.^{14, 15} The three 6-coordinate hemes are all low-spin ferric in the as-isolated protein, while the 5-coordinate heme II is high-spin ferric.¹⁶ Notice that hemes I and IV have

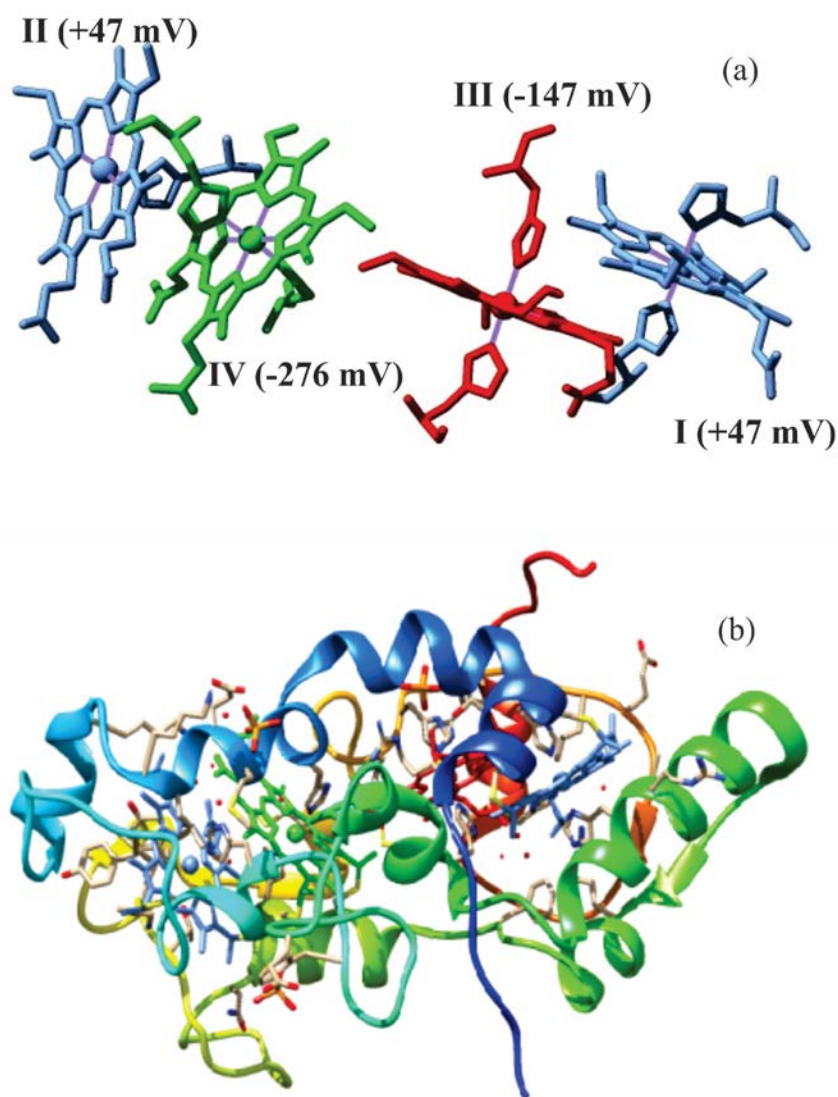


Figure 1.4. (a) Arrangement of the hemes within C_{554} , with the midpoint potentials reported in ref. ⁷. The numbering system is that used in the text. (b) The hemes in relation to the surrounding protein.

histidine imidazole planes in a perpendicular orientation whereas heme III has histidine imidazole planes in the parallel orientation (Fig. 1.4).^{14, 15} This is important because the two arrangements give rise to distinct EPR spectra, a fact that can be used to assign heme midpoint

potentials to specific hemes (Chapter 2).¹⁷⁻²⁰ Another notable feature in the heme coordination environment is the unusual distal histidine attachment to Heme I (Fig. 1.4). His 102 is covalently attached through N δ instead of the more common N ϵ . In turn N ϵ forms a hydrogen bond network to Glu 126 through water to N δ of His 96, which is the proximal ligand of heme III. This could be a stabilizing factor for His 102 in an otherwise sterically unfavorable conformation.¹⁴ A final notable feature in the heme coordination environment, which is particularly relevant to this work, is the vacant coordination site of heme II (Fig. 1.4). Though vacant, this open site is shielded by three residues Thr 154, Pro 155 and Phe 156. These residues are not close enough to coordinate to the iron, but leave only a small hydrophobic pocket, which

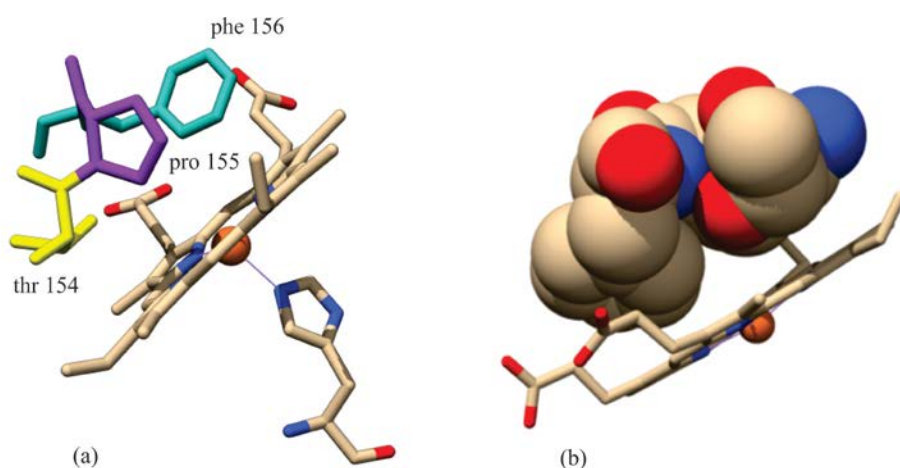


Figure 1.5. (a) The vacant site of heme II, with the bulky Thr154, Pro155, Phe156 labeled. Note that the iron is pulled out of the heme plane in the opposite direction by the histidine ligand. (b) Same as (a), but with Thr154, Pro155, and Phe156 rendered in space-filling model.

is not large enough to readily accommodate common heme ligands (Fig. 1.5).¹⁶ Nonetheless this is the site of NO coordination in the reduced protein,⁷ as will be discussed in more detail throughout this document.

The crystallographic studies of C₅₅₄ revealed the hemes to be stacked into two parallel but offset pairs (Fig. 1.4).^{14, 15} Thus, heme III is adjacent to heme I in a parallel-offset packing motif, and this heme pair is perpendicular but adjacent to the parallel-offset heme II - heme IV pair. All adjacent hemes are within Van der Waals contact, with the distance between heme edges of each heme pair being 3.5-3.8 Å. The distance between the iron centers of any given heme pair is roughly 9 Å.¹⁴ Interestingly, the two heme pairs of C₅₅₄ overlay remarkably well on heme pairs in other multi-heme proteins, notably HAO, despite the total lack of primary sequence similarity between C₅₅₄ and these proteins.^{14, 15}

C₅₅₄ and HAO have complementary isoelectric points (pIs), 10.7 and 3.4, respectively.^{12, 21} This, plus the fact that the genes for the two proteins form identifiable gene clusters,¹³ provided an early basis for the hypothesis that C₅₅₄ is the physiological electron acceptor for HAO (Fig. 1.2). This hypothesis is further supported by the crystallographic data.¹⁴ There is a large positively charged ridge above the solvent-exposed C₅₅₄ heme I, which could potentially be the site of docking to a large acidic patch that surrounds HAO heme 1. Both the positively charged region of C₅₅₄ and the negatively charged cavity of HAO are roughly 30 Å wide. In simulated docking the iron of solvent-exposed C₅₅₄ heme I is 20 Å from the iron of the solvent-exposed HAO heme 1, while the closest distance of the heme rings is 8 Å. In an early study of *N. europaea* *c*-hemes a small monoheme protein with pI of 3.7, cytochrome *c*₅₅₂, was proposed to be the electron acceptor for C₅₅₄.¹² A role for cytochrome *c*₅₅₂ can't be entirely discounted;¹⁴ however, there is no crystallographic evidence of complementary surfaces between the proteins,¹⁴ and the cytochrome *c*₅₅₂ gene is not part of the same gene cluster as HAO and C₅₅₄.²² For this reason more recent reports have suggested that the tetraheme cytochrome *c*_{m552}, which is a part of the same gene cluster, is C₅₅₄'s accepting partner, as shown in Fig. 1.2.^{10, 11} As this

protein is anchored to the periplasmic side of the cytoplasmic membrane, it would provide a plausible electron transfer pathway to the intramembrane quinone pool.

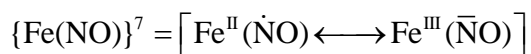
The midpoint potentials of the C₅₅₄ hemes have been determined by UV/Vis spectropotentiometry,²³ and correlated to specific hemes in the structure through EPR and Mossbauer spectroscopy.¹⁶ The midpoint potential assignments are +47, +47, -147, and -276 mV, as shown in Fig. 1.4. During HAO's catalytic cycle C₅₅₄ is only reduced by two electrons, and the generation of a one- or three-electron reduced C₅₅₄ is prevented.²⁴ Though the midpoint potentials of hemes I and II appear to be degenerate in spectropotentiometric titrations, a more recent protein film voltammetry study by the Elliot group of Boston University showed that they are in fact distinct though very similar, with hemes II and I having values of +32 mV and +50 mV, respectively.²⁵ The electrochemistry of C₅₅₄ and its variants is described in more detail in Chapter 2.

1.3. The reported interaction of *N. europaea* C₅₅₄ with NO

As mentioned above, many aspects of the heme arrangement in C₅₅₄ are replicated in other multi-heme proteins. Notably, the parallel-offset heme II-heme IV pair overlays remarkably well on the P₄₆₀-heme 6 pair in HAO.¹⁴ P₄₆₀ is the active site of HAO where NH₂OH binds and is oxidized, and like C₅₅₄ heme II it is a 5-coordinate iron complex. P₄₆₀ is heme-like, but it has an sp³ center at one of the meso carbons of the macrocycle.^{26, 27} In C₅₅₄ the vacant site is shielded by Thr 154, Pro 155 and Phe 156 as shown in Fig. 1.5, which prevents it from accommodating common heme ligands such as CO or CN⁻. Surprisingly though, a 2006 paper reported that not only will reduced C₅₅₄ bind NO at heme II, but under certain conditions it will

catalyze its reduction to N₂O.⁷ This section summarizes the results of the previous report, which provided the starting point for the work presented in this dissertation.

The first evidence for C₅₅₄ nitrosylation came from experiments in which the protein was 2-electron reduced by hydroxylamine in the presence of catalytic amounts of HAO. X- and Q-band EPR spectra of the reduced C₅₅₄ showed frequency-dependent signals that could be assigned to antiferromagnetically coupled low-spin hemes (S₁ = 1/2, S₂ = 1/2). Simulation of these signals in turn showed that the g values for one of the coupled hemes were characteristic of nitrosyl species referred to as {Fe(NO)}⁷, which can also be described by the two resonance structures shown in Scheme 1.1.⁶ Mössbauer analysis of the 2-electron reduced C₅₅₄ supported the presence of an {Fe(NO)}⁷ moiety. Furthermore, the same species could be generated in the absence of hydroxylamine and HAO by first reducing C₅₅₄ electrochemically, and then adding an equivalent of NO. The authors of the study concluded that, in the HAO-catalyzed process, NO generated from hydroxylamine oxidation bound to heme II of C₅₅₄.⁷ Though the product for HAO-catalyzed hydroxylamine oxidation is commonly assumed to be nitrite, there is substantial evidence that, under anaerobic conditions, NO is the actual product released.²⁸⁻³⁰



Scheme 1.1. Fe-NO species is represented in terms of two resonance structures, depicted by the corresponding Enemark-Feltham description {Fe(NO)}ⁿ. In this notation, the superscript n is the sum of the d electrons from the Fe, and the π* electrons from the NO moiety.⁶

Upadhyay et al. reported that addition of a second equivalent of NO to the electrochemically-generated two-electron reduced C₅₅₄ resulted in nearly complete oxidation of heme I, but left heme II in the {Fe(NO)}⁷ state. From these results they surmised that a

bimolecular reaction between bound and free NO was giving rise to N₂O production, with the electrons for NO reduction coming from oxidation of the C₅₅₄ heme I.⁷ When fully reduced C₅₅₄ was exposed to one equivalent of NO heme II was once again nitrosylated, but the nitrosylated product was re-reduced in the presence of excess reductant (dithionite). Conversely, if excess NO was added to fully reduced C₅₅₄ in the absence of excess reductant, then hemes I, III, and IV were rapidly oxidized. Again, these results were consistent with NO reduction by the C₅₅₄ hemes, and/or excess dithionite reducing agent. Based on rough single-turnover kinetics experiments, Upadhyay et al. estimated the turnover number for reduction of NO by C₅₅₄ to be at least 16 s⁻¹, which is on the same order of magnitude as known nitric oxide reductases (NORs).³¹⁻³³ Based on these results Upadhyay et al. concluded that, in addition to its electron transport role, C₅₅₄ also functions as an NO reductase.⁷

1.4. The ecological importance of nitrite reduction path control

As mentioned in Section 1.1, until the early 20th century the only significant route by which nitrogen could become bioavailable for the vast majority of life forms was through nitrogen fixation by nitrogen fixing microorganisms. The invention of the Haber-Bosch process for making ammonia industrially changed the situation dramatically, to the point where more ammonia is now produced artificially than by biological nitrogen fixation.⁴ This development has been essential for feeding the growing global population, but it hasn't been without negative consequences. Indeed, by producing such enormous amounts of ammonia humans have, over the last 50, years significantly shifted the balance between the components of the nitrogen cycle (Fig. 1.1) in favor of reactive nitrogen species such as NH₄⁺ and NO₃⁻.^{3-5, 34, 35} This shift is having many unintended negative consequences that arise primarily from the currently

inefficient use of ammonia fertilizer; for the good of the planet, these consequences will have to be mitigated in the coming years.^{3-5, 34, 35}

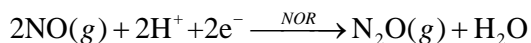
The two biggest problems that have arisen from the massive increase in reactive nitrogen availability have been the concomitant increases in nitrate and N₂O concentrations. Though both ammonium and nitrate are bioavailable, the positively charged ammonium species tends to bind to negatively charged soils, whereas negatively charged nitrate tends to wash through the soils and end up in aquifers. Once there it can be used as fertilizer by algae, which proceed to grow in an uncontrolled way that consumes all dissolved oxygen, killing aerobic organisms. This process, called “eutrophication”, is creating huge “dead zones” in the Gulf of Mexico’s Mississippi delta, and in other waterways heavily affected by agriculture.^{4, 5} Unlike nitrate, N₂O is not a viable fertilizer, and is eventually converted to dinitrogen by a subset of denitrifying bacteria. However, because of its comparative inertness, N₂O can persist in the atmosphere for prolonged periods of time. This is a problem because N₂O is a potent greenhouse gas (about 300× more potent than CO₂),³ and also an ozone depleter; indeed, a recent study showed that N₂O is now the single most important ozone depleting emission, and is likely to remain as such throughout the 21st century.^{36, 37}

Clearly a better understanding of the interplay between the various chemical processes in the nitrogen cycle, in particular in the vicinity of the NO branch-point (Fig. 1.1), could greatly aid microbial physiologists and ecologists, and ultimately farmers, to find more efficient and ecologically friendly ways of using fertilizer. The next two sections summarize what is currently known about biological reduction of NO to N₂O. Section 1.5 focuses on the classic NO reductases of anaerobic denitrifiers, while Section 1.6 centers on alternative N₂O forming pathways, particularly those mediated by ammonia oxidizing bacteria under moderately anoxic

conditions. Section 1.7 briefly looks at some factors that might determine whether NO is reduced to NH₄⁺ or N₂O in a given circumstance, and then summarizes the scope of the dissertation.

1.5. Nitric oxide reduction during dissimilatory denitrification

Nitric oxide reductases (NORs) are heme containing enzymes that catalyze the reduction of nitric oxide to nitrous oxide in denitrifying bacteria (Fig. 1.1, Scheme 1.2).³¹ In 1994 NORs were classified into the heme-copper containing oxidase superfamily based on the similarity of their amino acid sequences with the catalytic subunits of cytochrome oxidases, which reduce oxygen to water as the terminal step in aerobic respiration.³⁸ All NORs are integral membrane proteins. Three types have been characterized, cNORs, qNORs and qCu_ANOR, with the major difference between them being the source of electrons that they utilize.³⁹ For cNORs the electron donors are small electron transport proteins such as *c*-cytochromes or blue copper proteins, whereas qNORs and qCu_ANOR use ubihydroquinone or menahydroquinone. The one example of a qCu_ANOR discovered so far is further distinguished in having a copper center that is absent from the other two classes. The cNOR class has been most extensively characterized, and will be the focus of the rest of this section.



Scheme 1.2.

The cNORs are cytochrome *bc* heterodimers purified from gram negative bacteria.^{39, 40} The NorC subunit is relatively small (ca. 17 kDa), and contains a *c*-heme that is coordinated by His and Met axial ligands. Physiologically it is reduced by soluble *c*-hemes or blue copper proteins, and passes the electrons on to the much larger (ca. 53 kDa) NorB subunit, which is the

catalytic center. NorC is membrane-anchored, while NorB is a highly hydrophobic integral membrane protein that contains twelve transmembrane α -helices.³⁸⁻⁴¹ NorB contains three iron centers: two *b*-hemes and one non heme iron referred to as Fe_B. One low spin *b*-type heme mediates electron transfer from the *c*-heme in NorC to the catalytic center, which contains the second *b*-type heme (heme *b*₃, high-spin), and Fe_B.

The crystal structure of *Pseudomonas aeruginosa* cNOR has been solved to 2.7 Å resolution for the resting enzyme,⁴¹ and also for the reduced enzyme in the presence of a variety of ligands.⁴² Inspection of the fully oxidized cNOR active site reveals that the Fe_B iron is coordinated by three His residues and a Glu, that the heme *b*₃ and Fe_B iron centers are 3.8 Å apart, and that they are bound together by an oxo bridge. Such an arrangement is too crowded to accommodate two NO molecules, and Hino et al. initially suggested that the glutamate might dissociate from Fe_B during the catalytic cycle, thus making more space for the incoming NO moieties.⁴¹ However, the later crystallographic investigation showed that the active site is quite elastic, so that after reduction it expands to the point where it can accommodate two CO molecules (one at each iron center), and even the bulky ligand acetaldoxime.⁴² Other than a lengthening of the Fe-Fe separation (from 3.8 Å to 4.4 Å), and protonolysis of the oxo bridge, no significant ligand rearrangements were observed around the active site metals. These results showed that two NO molecules would fit readily into the active site, without the need to change the metal coordination environments.

Based on the available crystallographic data,^{41, 42} and on earlier spectroscopic analyses,^{39, 43-45} Figure 1.6 shows a plausible catalytic cycle for reduction of NO to N₂O by cNOR, likely the most plausible of three that have been proposed over the years.^{41, 44} The first step in the cycle would be protonolysis of the oxo bridge between the two iron centers. This could be coupled to

the next step, metal reduction, but there is EPR evidence for the existence of the unbridged oxidized moiety as well.⁴⁴ After reduction of the two iron centers, one NO molecule would bind to each. EPR and Resonance Raman experiments suggest that NO binding to heme b_3 is accompanied by dissociation of the proximal histidine, as shown in Figure 1.6,⁴⁵ though this was not observed in the crystallographic studies with reduced cNOR.⁴² At this point both the heme b_3 and the Fe_B nitrosylated sites would be in the $\{\text{Fe}(\text{NO})\}^7$ state (Scheme 1.1),⁶ which has substantial radical character centered on the nitrogen;⁴⁶ positioning two such sites in close proximity would promote formation of an N-N bond. The exact steps that follow are unclear;

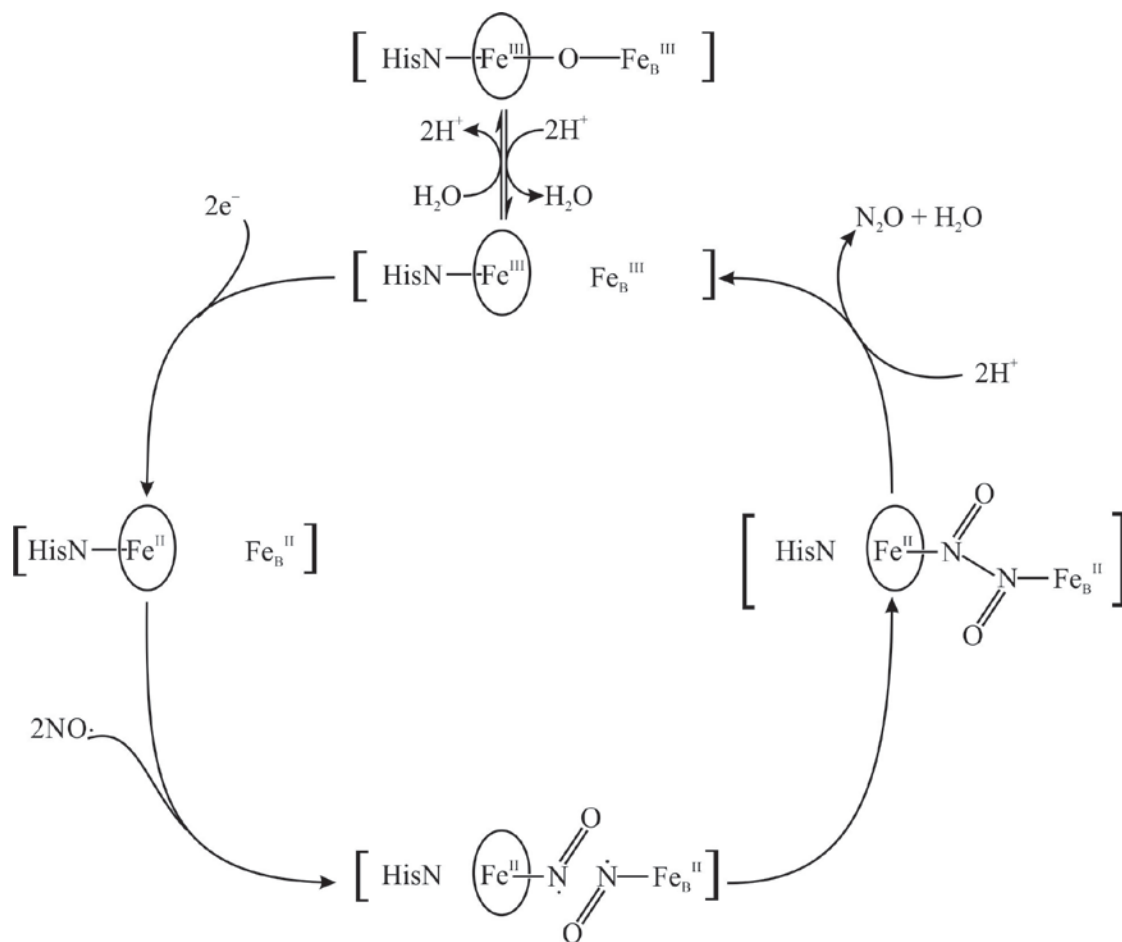


Figure 1.6. Proposed steps in the cNOR-catalyzed reduction of NO to N₂O.

however formally at least, N₂O formation to complete the cycle would require transfer of two electrons from the irons to one of the nitrogens, followed by protonolysis of a N-O bond. The crystal structure of cNOR reveals two possible hydrophilic channels that could transport protons to the active site, as well as a hydrophobic channel that could act as a conduit for NO.⁴¹

1.6. N₂O generation by way of nitric oxide – hydroxylamine comproportionation

Autotrophic ammonia oxidizing bacteria (AOB) have been identified as major contributors of N₂O.⁴⁷ Two distinct pathways have been identified so far for N₂O production by AOB.⁴⁷ The first pathway, often referred to as the “nitrifier denitrification (ND)” pathway, is really the same process described in Section 1.5, but carried out by nitrifying rather than denitrifying bacteria.⁴⁸ The pathway involves initial reduction of NO₂⁻ to NO by the copper containing nitrite reductase NirK, followed by NO reduction to N₂O by a NOR protein analogous to that described in the previous section. The second pathway to N₂O in AOB is often referred to as the “hydroxylamine” pathway, because it has long been known to require the combined presence of both hydroxylamine and NO.^{47, 49} Both nitrifier denitrification and the hydroxylamine pathway from AOB are reviewed in this section. In addition, a N₂O-producing pathway seen in fungi, which bears some relation to the AOB hydroxylamine pathway, is also briefly discussed.

The nitrifier denitrification pathway is promoted under O₂-limiting conditions when nitrite concentrations are high.⁵⁰ During entry into strict anaerobic conditions NH₃ and NH₂OH oxidation nearly cease, and NO₂⁻ is reduced to NO by NirK. This reduction is speculated to be supported by the cytochrome pool, cytochromes C₅₅₄ and C_{m552}, the latter of which has been shown to exchange electrons with the membrane-associated quinone/quinol pool.⁵¹ Interestingly, genetic and whole-cell studies suggest that the activities of NirK and NOR don't wax and wane

in tandem. Increased production of NO is observed in AOB cultures that are made anaerobic, but there is no corresponding increase in N₂O production under these conditions.

Correspondingly, mRNA studies show that *norB* mRNA concentrations actually decrease under anaerobic conditions along with mRNA concentrations of the genes encoding HAO and AMO, whereas *nirK* mRNA concentrations increase.⁵⁰ N₂O formation is seen upon recovery to aerobic conditions, and appears to parallel renewed availability of NH₃. Under these conditions mRNA studies show that *nirK* mRNA concentration decreases, while the concentrations of *norB* mRNA, and the mRNA for HAO and AMO production, all increase.⁴⁹

Surprisingly, knockouts in *N. europaea* of *nirK* and *norB* suggest that *nirK* is not essential for the nitrifier denitrifier pathway; however, no other genes for nitrite reductases have been identified.⁵² The *norB* gene was shown to be essential for production of N₂O in the nitrifier denitrifier pathway, as no measurable amount of N₂O was observed in *norB* knockouts. A c-terminally truncated HAO has been suggested as a possible candidate for nitrite reductase,⁵³ but much still remains to be clarified about these systems.

The hydroxylamine pathway for N₂O production seems to peak when there is incomplete oxidation of NH₂OH to NO₂⁻ under aerobic conditions.^{47, 54} Though long known to be distinct from nitrifier denitrification, the first truly convincing mechanistic analysis of this pathway was only recently published in 2016.⁵⁴ The 2016 paper by Caranto et al. described NO – NH₂OH comproportionation catalyzed by the protein cytochrome P460 (cyt P460) from *N. europaea*. Cyt P460 is a 36 kDa homodimeric protein in which each subunit has a single c-heme like prosthetic group, the P460, that differs from a true c-heme by having an N – C crosslink from one of the porphyrin meso carbons to a lysine residue.⁵⁵ The iron in the P460 is 5-coordinate, and comproportionation at the vacant site is proposed to proceed as shown in Figure 1.7.⁵⁴

According to this mechanism NH_2OH first binds to the resting enzyme, and is then oxidized by 3 electrons to generate the $\{\text{Fe}(\text{NO})\}^6$ species.⁶ As shown by the lower resonance form in Figure 1.7 the bound nitrosyl in $\{\text{Fe}(\text{NO})\}^6$ is electrophilic,⁵⁶⁻⁶⁰ and in the rate determining step it is proposed to undergo nucleophilic attack by free NH_2OH , which ultimately results in release of N_2O . One-electron oxidation of the P460 then regenerates the resting enzyme. Notice that $\{\text{Fe}(\text{NO})\}^6$ can also be generated by direct addition of free NO to the resting enzyme.

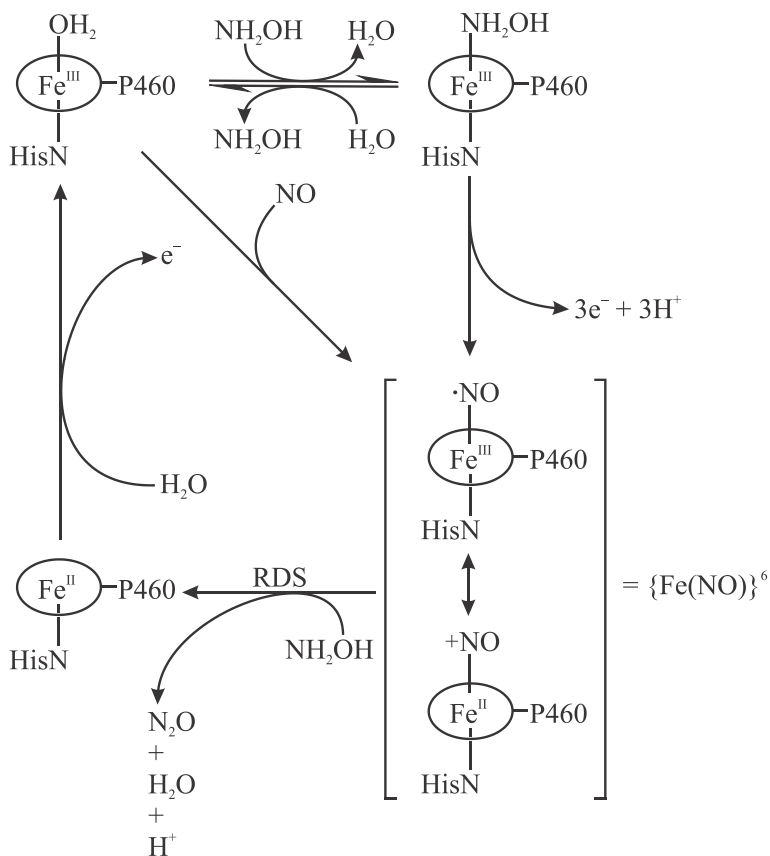


Figure 1.7. Proposed steps in the cyt P460-catalyzed comproportionation of NO and NH_2OH . This comproportionation is often known as the “hydroxylamine pathway” for N_2O formation in AOB.

Though the paper of Caranto et al. focused on the chemistry of Cyt P460, it is important to note that the active site of HAO is also a P460-type moiety, with many of the same properties.^{26, 27} Moreover, it is known that under anaerobic conditions the product of NH_2OH oxidation by HAO is NO rather than NO_2^- .^{28, 29} Thus it will not be surprising if future studies demonstrate that HAO can also catalyze $\text{NO} - \text{NH}_2\text{OH}$ comproportionation by a mechanism analogous to that proposed in Figure 1.7 for Cyt P460.

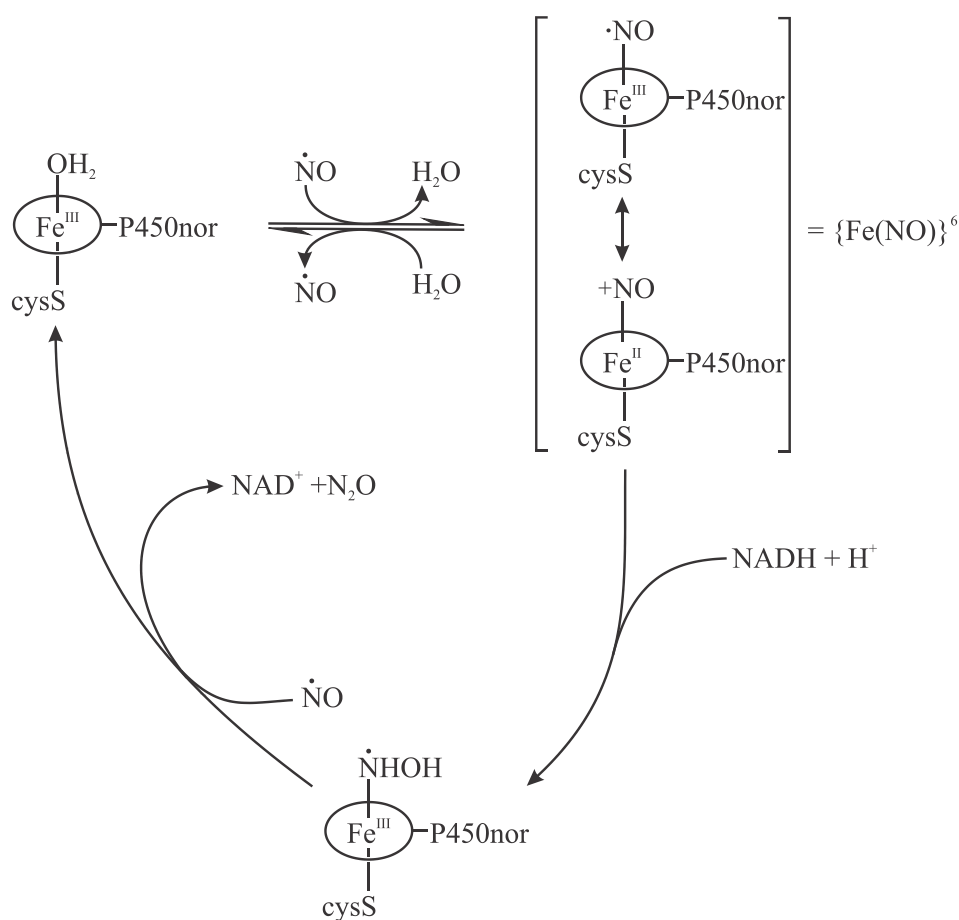


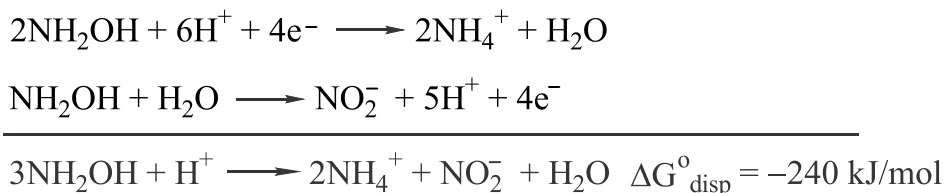
Figure 1.8. Proposed steps in the fungal cyt P450nor-catalyzed comproportionation of NO and NH_2OH . Note the similarities with the scheme proposed in Fig. 1.7 for the bacterial P460 enzyme. In both cases the primary mechanistic evidence is spectroscopic, but it is easy to imagine that the enzymes and proposed mechanisms could switch depending on reaction conditions.

Finally, it should be noted that a mechanism very similar to the hydroxylamine pathway of AOB has been proposed to explain fungal N₂O production. In the fungal denitrification system, initial reduction of nitrate and nitrite are catalyzed by enzymes analogous to those seen in prokaryotes; however, N₂O production is catalyzed by a unique P450 enzyme known as P450nor. The proposed mechanism for P450nor is shown in Figure 1.8.⁶¹ In the first step of the catalytic cycle NO binds to the resting enzyme to produce an {Fe(NO)}⁶ species. A 2-electron reduction of this species by NADH yields a hydroxylamine radical bound to Fe^{III} (detected by EPR); this species can interact with free NO, itself a radical, to ultimately release N₂O. In support of the hydroxylamine radical intermediate proposed in Figure 1.8, our group detected a similar species within 15 ms of rapidly mixing free NH₂OH with the nitrite ammonifying enzyme cytochrome *c* nitrite reductase.⁶²

1.7. Ammonification vs. denitrification

The 6-electron reduction of nitrite to ammonia is catalyzed by the periplasmic, decaheme homodimeric enzyme cytochrome *c* nitrite reductase (ccNiR), which also catalyzes the 5-electron reduction of NO, or the 2-electron reduction of NH₂OH, to ammonia. Under physiological conditions ccNiR catalyzes nitrite reduction to ammonia without release of intermediates. However, in vitro the Pacheco group has found it possible to trap putative intermediates, or to release partially reduced nitrogen species such as nitric oxide, by controlling the electrochemical potential at which reduction takes place.^{63, 64} Thus, for example, when the weak reductant ferrocyanide is used as the electron source, *S. oneidensis* ccNiR catalyzes the one-electron reduction of nitrite to nitric oxide.⁶⁴ In a separate study the Pacheco group showed that ccNiR will oxidize stoichiometric amounts of a large excess of NH₂OH to nitrite, but won't catalyze NH₂OH disproportionation to NH₄⁺ and NO₂⁻, despite a very favorable driving force (Scheme

1.3).⁶² On the basis of these accumulated results, our group has developed the working hypothesis shown schematically in Fig. 1.9. According to this hypothesis there is a large



Scheme 1.3. Energetics of hydroxylamine disproportionation.

activation barrier between NH_2OH and NH_4^+ that makes the thermodynamically favorable reduction of NO_2^- , NO or NH_2OH to NH_4^+ slow, unless a significant overpotential is supplied. Thus, for example, electrochemical reduction of NO_2^- that is thermodynamically favorable at applied potentials of 0 mV vs SHE, does not occur at appreciable rates at applied potentials above -200 mV vs SHE.⁶⁵

The Fig. 1.9 hypothesis could also be predicting the conditions under which NO reduction to N_2O will be favored over reduction to NH_4^+ ; in essence the latter could only occur at applied potentials low enough to overcome the activation barrier. At higher applied potentials, and in the presence of a suitable catalyst, reduction of NO will generate N_2O instead. The last two sections of this chapter presented two distinct strategies for generating N_2O enzymatically. In the classic NORs reviewed in Section 1.5 a dinuclear iron active site aligns two NO molecules in such a way as to first promote $\text{NO} - \text{NO}$ dimerization, then reduction of the dimer, and finally protonolysis of one $\text{N} - \text{O}$ bond (Fig. 1.6). The second strategy, seen in AOB and fungi, utilized mononuclear iron active sites, and relied on NO and NH_2OH being available together so that they could undergo comproportionation (Figs. 1.7 and 1.8). The Fig. 1.9 hypothesis suggests the intriguing possibility that ccNiR could be induced to generate N_2O in the presence of a reducing

agent that takes NO (or NO_2^-) to NH_2OH but not to NH_4^+ , while an enzyme such as cyt P460 that has been shown to generate N_2O might also produce NH_4^+ in the presence of a sufficiently powerful reducing agent. The former conjecture has yet to be tested experimentally; however the Pacheco group demonstrated some years ago that HAO, and even myoglobin and catalase, were capable of reducing NO and NH_2OH to ammonia.^{29, 66} HAO will even catalyze the reduction of NO_2^- to NH_4^+ in the presence of the strong reductant methyl viologen monocation radical.²⁹

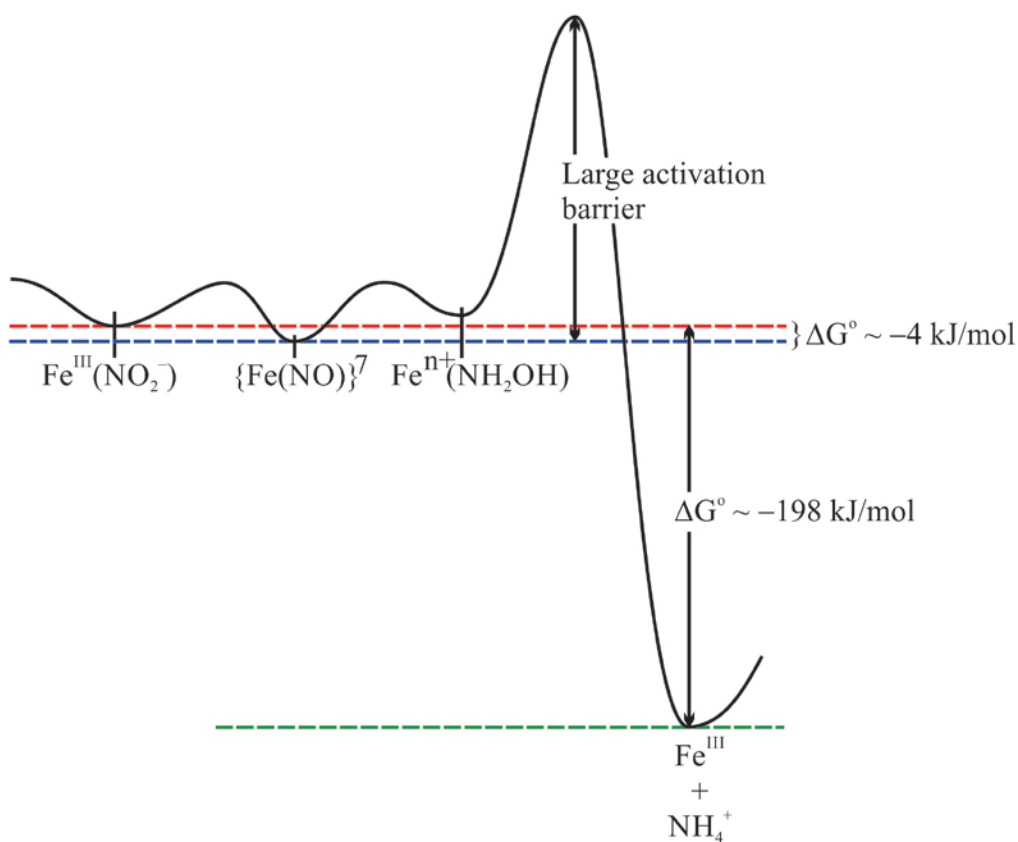


Figure 1.9. Schematic view of the putative activation barrier that makes enzyme-catalyzed reduction of hydroxylamine to ammonia slow, unless an overpotential is supplied to overcome it.

Experiments to test the Fig. 1.9 hypothesis with ccNiR and HAO are ongoing in the Pacheco group, but the purported NO reductase activity of C₅₅₄ (Section 1.4)⁷ poses an apparent challenge to this hypothesis. In their paper Upadhyay et al. reported that C₅₅₄-catalyzed reduction of NO to N₂O occurred at potentials poised by dithionite,⁷ which has a midpoint potential comparable to, or lower than that of the methyl viologen monocation radical. Under such conditions, we'd have predicted reduction of NO to NH₄⁺ instead, based on Fig. 1.9. Presumably C₅₅₄ – catalyzed reduction of NO would have to proceed by a mechanism more akin to those of Figs. 1.7 and 1.8 than that shown in Fig. 1.6, since the protein's 5-coordinate heme II is a monovalent site. Based on the Fig. 1.9 hypothesis we'd predict that C₅₅₄ would catalyze NO reduction to N₂O when provided with comparatively weak reducing agents that could reduce NO only as far as NH₂OH, but would reduce NO to NH₄⁺ when provided with more powerful reducing agents. However C₅₅₄ is unusual because the heme II vacant site seems too small to allow NO and NH₂OH to be present simultaneously, and furthermore it has a hydrophobic pocket devoid of possibly essential proton donors (Fig. 1.5).[†] All of these considerations made the interaction of NO with C₅₅₄ worthy of further study.

Chapter 3 of this dissertation presents a rigorous re-evaluation of the interaction between NO and wild type C₅₅₄ at various stages of reduction. Chapters 4 and 5 extend the investigation to C₅₅₄ mutants in which the vacant site is expanded by substituting a phenylalanine by an alanine (Chapter 4), or is provided with the protonatable residue histidine in the place of phenylalanine (Chapter 5). Chapter 2 provides an electrochemical characterization of the wild type and mutant C₅₅₄ moieties, as well as a description of the methods for preparation of all the

[†]A third possible mechanism would involve release of NO⁻ or HNO from C₅₅₄, which would then spontaneously dimerize and dehydrate in solution.^{67, 68}

protein species, and their spectroscopic properties. The Chapter 2 results proved essential for interpreting the results of Chapters 3-5.

1.8. References

- [1] Fenchel, T., King, G. M., and Blackburn, T. H. (1998) *Bacterial Biogeochemistry*, 2nd ed., Academic Press, London.
- [2] Ehrlich, H. L. (2002) *Geomicrobiology*, 4th ed., Marcel Dekker, Inc, New York, NY.
- [3] Canfield, D. E., Glazer, A. N., and Falkowski, P. G. (2010) The Evolution and Future of Earth's Nitrogen Cycle, *Science* 330, 192-196.
- [4] Galloway, J. N., Leach, A. M., Bleeker, A., and Erisman, J. W. (2013) A chronology of human understanding of the nitrogen cycle, *Phil. Trans. R. Soc. B.* 368, 20130120.
- [5] Lehnert, N., Coruzzi, G., Hegg, E., Seefeldt, L., and Stein, L. (2015) Feeding the world in the 21st century: grand challenges in the nitrogen cycle, National Science Foundation Workshop, https://www.nsf.gov/mps/che/workshops/nsf_nitrogen_report_int.pdf.
- [6] Enemark, J. H., and Feltham, R. D. (1974) Principles of Structure, Bonding and Reactivity for Metal Nitrosyl Complexes, *Coord. Chem. Rev.* 13, 339-406.
- [7] Upadhyay, A. K., Hooper, A. B., and Hendrich, M. P. (2006) NO reductase activity of the tetraheme cytochrome c(554) of *Nitrosomonas europaea*, *J. Am. Chem. Soc.* 128, 4330-4337.
- [8] Kartal, B., Maalcke, W. J., de Almeida, N. M., Cirpus, I., Gloerich, J., Geerts, W., Op den Camp, H. J., Harhangi, H. R., Janssen-Megens, E. M., Francoijs, K. J., Stunnenberg, H. G., Keltjens, J. T., Jetten, M. S. M., and Strous, M. (2011) Molecular mechanism of anaerobic ammonium oxidation, *Nature* 479, 127-130.

- [9] Dietl, A., Ferousi, C., Maalcke, W. J., Menzel, A., de Vries, S., Keltjens, J. T., Jetten, M. S. M., Kartal, B., and Barends, T. R. M. (2015) The inner workings of the hydrazine synthase multiprotein complex, *Nature* 527, 394-397.
- [10] Whittaker, M., Bergmann, D., Arciero, D., and Hooper, A. B. (2000) Electron transfer during the oxidation of ammonia by the chemolithotrophic bacterium *Nitrosomonas europaea*, *Biochim. Biophys. Acta Bioenerg.* 1459, 346-355.
- [11] Kim, H. J., Zatsman, A., Upadhyay, A., Whittaker, M., Bergmann, D. J., Hendrich, M. P., and Hooper, A. B. (2008) Membrane tetraheme cytochrome *c_{m552}* of the ammonia-oxidizing *Nitrosomonas europaea*: A ubiquinone reductase, *Biochemistry* 47, 6539-6551.
- [12] Yamanaka, T., and Shinra, M. (1974) Cytochrome *c-552* and cytochrome *c-554* derived from *Nitrosomonas europaea*, *J. Biochem.* 75, 1265-1273.
- [13] Bergmann, D. J., Arciero, D. M., and Hooper, A. B. (1994) Organization of the *hao* gene cluster of *Nitrosomonas europaea*: genes for two tetraheme *c* cytochromes, *J. Bacteriol.* 176, 3148-3153.
- [14] Iverson, T. M., Arciero, D. M., Hsu, B. T., Logan, M. S. P., Hooper, A. B., and Rees, D. C. (1998) Heme packing motifs revealed by the crystal structure of the tetra-heme cytochrome *c554* from *Nitrosomonas europaea*, *Nat. Struct. Biol.* 5, 1005-1012.
- [15] Iverson, T. M., Arciero, D. M., Hooper, A. B., and Rees, D. C. (2001) High-resolution structures of the oxidized and reduced states of cytochrome *c554* from *Nitrosomonas europaea*, *J. Biol. Inorg. Chem.* 6, 390-397.
- [16] Upadhyay, A. K., Petasis, D. T., Arciero, D. M., Hooper, A. B., and Hendrich, M. P. (2003) Spectroscopic characterization and assignment of reduction potentials in the tetraheme cytochrome *c(554)* from *Nitrosomonas europaea*, *J. Am. Chem. Soc.* 125, 1738-1747.

- [17] Walker, F. A. (1999) Magnetic spectroscopic (EPR, ESEEM, Mossbauer, MCD and NMR) studies of low-spin ferriheme centers and their corresponding heme proteins, *Coord. Chem. Rev.* 186, 471-534.
- [18] Spinner, F., Cheesman, M. R., Thomson, A. J., Kaysser, T., Gennis, R. B., Peng, Q., and Peterson, J. (1995) The haem b_{558} component of the cytochrome *bd* quinol oxidase complex from *Escherichia coli* has histidine-methionine axial ligation, *Biochem. J.* 308, 641-644.
- [19] Walker, F. A., Huynh, B. H., Scheidt, W. R., and Osvath, S. R. (1986) Models of the cytochromes *b*. Effect of axial ligand plane orientation on the EPR and Mossbauer spectra of low-spin ferrihemes, *J. Am. Chem. Soc.* 108, 5288-5297.
- [20] Stein, N., Love, D., Judd, E. T., Elliott, S. J., Bennett, B., and Pacheco, A. A. (2015) Correlations between the electronic properties of *Shewanella oneidensis* cytochrome *c* nitrite reductase (ccNiR) and its structure: effects of heme oxidation state and active site ligation, *Biochemistry* 54, 3749-3758.
- [21] Hooper, A. B., Maxwell, P. C., and Terry, K. R. (1978) Hydroxylamine oxidoreductase from *Nitrosomonas*: absorption spectra and content of heme and metal, *Biochemistry* 17, 2984-2989.
- [22] Chain, P., Lamerdin, J., Larimer, F., Regala, W., Lao, V., Land, M., Hauser, L., Hooper, A. B., Klotz, M., Norton, J., Sayavedra-Soto, L., Arciero, D. M., Hommes, N., Whittaker, M., and Arp, D. (2003) Complete genome sequence of the ammonia oxidizing bacterium and obligate chemolithoautotroph *Nitrosomonas europaea*, *J. Bacteriol.* 185, 2759-2773.

- [23] Arciero, D. M., Collins, M. J., Haladjian, J., Bianco, P., and Hooper, A. B. (1991) Resolution of the 4 Hemes of Cytochrome-C554 from *Nitrosomonas-Europaea* by Redox Potentiometry and Optical Spectroscopy, *Biochemistry* 30, 11459-11465.
- [24] Arciero, D. M., Balny, C., and Hooper, A. B. (1991) Spectroscopic and Rapid Kinetic-Studies of Reduction of Cytochrome-C554 by Hydroxylamine Oxidoreductase from *Nitrosomonas-Europaea*, *Biochemistry* 30, 11466-11472.
- [25] Pulcu, G. S., Elmore, B. L., Arciero, D. M., Hooper, A. B., and Elliott, S. J. (2007) Direct electrochemistry of tetraheme cytochrome *c₅₅₄* from *Nitrosomonas europaea*: redox cooperativity and gating, *J. Am. Chem. Soc.* 129, 1838-1839.
- [26] Igarashi, N., Moriyama, H., Fujiwara, T., Fukumori, Y., and Tanaka, N. (1997) The 2.8 angstrom structure of hydroxylamine oxidoreductase from a nitrifying chemoautotrophic bacterium, *Nitrosomonas europaea*, *Nat. Struct. Biol.* 4, 276-284.
- [27] Cedervall, P., Hooper, A. B., and Wilmot, C. M. (2013) Structural studies of hydroxylamine oxidoreductase reveal a unique heme cofactor and a previously unidentified interaction partner, *Biochemistry* 52, 6211-6218.
- [28] Hooper, A. B., and Terry, K. R. (1979) Hydroxylamine oxidoreductase of *nitrosomonas*: production of nitric oxide from hydroxylamine, *Biochim. Biophys. Acta* 571, 12-20.
- [29] Kostera, J., McGarry, J. M., and Pacheco, A. A. (2010) Enzymatic Interconversion of Ammonia and Nitrite: the Right Tool for the Job, *Biochemistry* 49, 8546-8553.
- [30] Maalcke, W. J., Dietl, A., Marritt, S. J., Butt, J. N., Jetten, M. S. M., Keltjens, J. T., Barends, T. R. M., and Kartal, B. (2014) Structural basis of biological NO generation by octaheme oxidoreductases, *J. Biol. Chem.* 289, 1228-1242.

- [31] Zumft, W. G. (1997) Cell biology and molecular basis of denitrification, *Microbiol. Mol. Biol. Rev.* 61, 533-616.
- [32] Hendriks, J., Warne, A., Gohlke, U., Haltia, T., Ludovici, C., Lubben, M., and Saraste, M. (1998) The active site of bacterial nitric oxide reductase is a dinuclear iron center, *Biochemistry* 37, 13102-13109.
- [33] Gomes, C. M., Giuffre, A., Forte, E., Vicente, J. B., Saraiva, L. M., Brunori, M., and Teixeira, M. (2002) A novel type of nitric oxide reductase, *J. Biol. Chem.* 277, 25273-25276.
- [34] Galloway, J. N., Townsend, A. R., Erisman, J. W., Bekunda, M., Cai, Z., Freney, J. R., Martinelli, L. A., Seitzinger, S. P., and Sutton, M. A. (2008) Transformation of the Nitrogen Cycle: Recent Trends, Questions and Potential Solutions, *Science* 320, 889-892.
- [35] Duce, R. A., LaRoche, J., Altieri, K., Arrigo, K. R., Baker, A. R., Capone, D. G., Cornell, S., Dentener, F., Galloway, J., Ganeshram, R. S., Geider, R. J., Jickells, T., Kuypers, M. M., Langlois, R., Liss, P. S., Liu, S. M., Middelburg, J. J., Moore, C. M., Nickovic, S., Oschlies, A., Pedersen, T., Prospero, J., Schlitzer, R., Seitzinger, S., Sorensen, L. L., Uematsu, M., Ulloa, O., Voss, M., Ward, B., and Zamora, L. (2008) Impacts of Atmospheric Anthropogenic Nitrogen on the Open Ocean, *Science* 320, 893-897.
- [36] Ravishankara, A. R., Daniel, J. S., and Portmann, R. W. (2009) Nitrous oxide (N₂O): the dominant ozone-depleting substance emitted in the 21st century, *Science* 326, 123-125.
- [37] Wuebbles, D. J. (2009) Nitrous oxide: no laughing matter, *Science* 326, 56-57.
- [38] Saraste, M., and Castresana, J. (1994) Cytochrome oxidase evolved by tinkering with denitrification enzymes, *FEBS Lett.* 341, 13743.

- [39] Wasser, I. M., de Vries, S., Moenne-Loccoz, P., Schroder, I., and Karlin, K. D. (2002) Nitric Oxide in Biological Denitrification: Fe/Cu Metalloenzyme and Metal Complex NO_x Redox Chemistry, *Chemical Reviews* 102, 1201-1234.
- [40] Dermastia, M., Turk, T., and Hollocher, T. C. (1991) Nitric oxide reductase, *J. Biol. Chem.* 266, 10899-10905.
- [41] Hino, T., Matsumoto, Y., Nagano, S., Sugimoto, H., Fukumori, Y., Murata, T., Iwata, S., and Shiro, Y. (2010) Structural basis of biological N₂O generation by bacterial nitric oxide reductase, *Science* 230, 1666-1670.
- [42] Sato, N., Ishii, S., Sugimoto, H., Hino, T., Fukumori, Y., Sako, Y., Shiro, Y., and Tosha, T. (2014) Structures of reduced and ligand-bound nitric oxide reductase provide insights into functional differences in respiratory enzymes, *Proteins* 82, 1258-1271.
- [43] Shiro, Y. (2012) Structure and function of bacterial nitric oxide reductases, *Biochim. Biophys. Acta* 1817, 1907-1913.
- [44] Kumita, H., Matsuura, K., Hino, T., Takahashi, S., Hori, H., Fukumori, Y., Morishima, I., and Shiro, Y. (2004) NO reduction by nitric oxide reductase from denitrifying bacterium *Pseudomonas aeruginosa*, *J. Biol. Chem.* 279, 55247-55254.
- [45] Moenne-Loccoz, P., and de Vries, S. (1998) Structural characterization of the catalytic high-spin heme *b* of nitric oxide reductase: a Resonance-Raman study, *J. Am. Chem. Soc.* 120, 5147-5152.
- [46] Westcott, B. L., and Enemark, J. H. (1999) Transition Metal Nitrosyls, In *Inorganic Electronic Structure and Spectroscopy* (Solomon, E. I., and Lever, A. B. P., Eds.), pp 435-439, John Wiley and Sons, Inc., New York, NY.

- [47] Ni, B.-J., Peng, L., Law, Y., Guo, J., and Yuan, Z. (2014) Modeling nitrous oxide production by autotrophic ammonia-oxidizing bacteria with multiple production pathways, *Environ. Sci. Technol.* 48, 3916-3924.
- [48] Zhu, X., Burger, M., Doane, T. A., and Horwath, W. R. (2013) Ammonia oxidation pathways and nitrifier denitrification are significant sources of N₂O and NO under low oxygen availability, *PNAS* 110, 6328-6333.
- [49] Chandran, K., Stein, L. Y., Klotz, M. G., and van Loosdrecht, M. C. M. (2011) Nitrous oxide production by lithotrophic ammonia-oxidizing bacteria and implications for engineered nitrogen-removal systems, *Biochem. Soc. Trans.* 39, 1832-1837.
- [50] Yu, R., Kampschreur, M. J., Van Loosdrecht, M. C. M., and Chandran, K. (2010) Mechanisms and specific directionality of autotrophic nitrous oxide generation during transient anoxia, *Environ. Sci. Technol.* 44, 1313-1319.
- [51] Stein, L. Y., Campbell, M. A., and Klotz, M. G. (2013) Energy-mediated vs. ammonium-regulated gene expression in the obligate ammonia-oxidizing bacterium, *Nitrosococcus oceani*, *Front. Microbiol.* 4, 277.
- [52] Kozłowski, J. A., Price, J., and Stein, L. Y. (2014) Revision of N₂O-producing pathways in the ammonia-oxidizing bacterium *Nitrosomonas europaea* ATCC 19718, *Appl Environ. Microbiol.* 80, 4930-4935.
- [53] Hendgen-Cotta, U. B., Merx, M. W., Shiva, S., Schmidz, J., Becher, S., Klare, J. P., Steinhoff, H.-J., Goedecke, A., Schrader, J., Gladwin, M. T., Kelm, M., and Rassaf, T. (2008) Nitrite reductase activity of myoglobin regulates respiration and cellular viability in myocardial ischemia-reperfusion injury, *Proc. Natl. Acad. Sci. USA* 105, 10256-10261.

- [54] Caranto, J. D., Vilbert, A. C., and Lancaster, K. M. (2016) *Nitrosomonas europaea* cytochrome P460 is a direct link between nitrification and nitrous oxide emission, *PNAS* *113*, 14704-14709.
- [55] Pearson, A. R., Elmore, B. O., Yang, C., Ferrara, J. D., Hooper, A. B., and Wilmot, C. M. (2007) The crystal structure of cytochrome P₄₆₀ of *Nitrosomonas europaea* reveals a novel cytochrome fold and heme-protein cross-link, *Biochemistry* *46*, 8340-8349.
- [56] Hoshino, M., Maeda, M., Konishi, R., Seki, H., and Ford, P. C. (1996) Studies on the reaction mechanism for reductive nitrosylation of ferrihemoproteins in buffer solutions, *J. Am. Chem. Soc.* *118*, 5702-5707.
- [57] Ford, P. C., and Lorkovic, I. M. (2002) Mechanistic aspects of the reactions of nitric oxide with transition-metal complexes, *Chem. Rev.* *102*, 993-1017.
- [58] Wolak, M., and van Eldik, R. (2002) To be or not to be NO in coordination chemistry? A mechanistic approach, *Coord. Chem. Rev.* *230*, 263-282.
- [59] Fernandez, B. O., and Ford, P. C. (2003) Nitrite catalyzes ferriheme protein reductive nitrosylation, *J. Am. Chem. Soc.* *125*, 10510-10511.
- [60] Cabail, M. Z., and Pacheco, A. A. (2003) Selective One-Electron Reduction of *Nitrosomonas europaea* Hydroxylamine Oxidoreductase with Nitric Oxide, *Inorg. Chem.* *42*, 270-272.
- [61] Shoun, H., Fushinobu, S., Jiang, L., Kim, S.-W., and Wagaki, T. (2012) Fungal denitrification and nitric oxide reductase cytochrome P450_{nor}, *Phil. Trans. R. Soc. B.* *367*, 1186-1194.
- [62] Youngblut, M., Pauly, D. J., Stein, N., Walters, D., Conrad, J. A., Moran, G. R., Bennett, B., and Pacheco, A. A. (2014) *Shewanella oneidensis* cytochrome *c* nitrite reductase (ccNiR)

- does not disproportionate hydroxylamine to ammonia and nitrite, despite a strongly favorable driving force., *Biochemistry* 53, 2136-2144.
- [63] Stein, N. (2014) Spectroscopic and electrochemical studies of shewanella oneidensis cytochrome c nitrite reductase, and improving c-heme expression systems, In *Department of Chemistry and Biochemistry*, University of Wisconsin-Milwaukee.
- [64] Ali, M. M., Legaspi-Humiston, D., Keefe, K., Robinson, N. A., Pauly, D. J., and Pacheco, A. A. (Unpublished).
- [65] Judd, E. T., Youngblut, M., Pacheco, A. A., and Elliott, S. J. (2012) Direct Electrochemistry of Shewanella oneidensis Cytochrome c Nitrite Reductase: Evidence of Interactions across the Dimeric Interface, *Biochemistry* 51, 10175-10185.
- [66] Kostera, J., Youngblut, M. D., Slosarczyk, J. M., and Pacheco, A. A. (2008) Kinetic and product distribution analysis of NO reductase activity in *Nitrosomonas europaea* hydroxylamine oxidoreductase, *J. Biol. Inorg. Chem.* 13, 1073-1083.
- [67] Shafirovich, V., and Lyamar, S. V. (2002) Nitroxyl and its anion in aqueous solutions: spin states, protic equilibria, and reactivities toward oxygen and nitric oxide, *PNAS* 99, 7340-7345.
- [68] Shafirovich, V., and Lyamar, S. V. (2003) Spin-forbidden deprotonation of aqueous nitroxyl (HNO), *J. Am. Chem. Soc.* 125, 6547-6552.

Chapter 2

Spectropotentiometric analysis of cytochrome *c*₅₅₄ and selected variants

2.1. Introduction

In the initial account of C₅₅₄'s interactions with NO Upadhyay et al. noted that the nature of the interaction depended strongly on the extent of protein reduction, as well as the amount of NO present. Thus, for example, fully oxidized C₅₅₄ didn't interact with NO at all, 2-electron reduced protein was nitrosylated by one equivalent of NO but also slowly oxidized by excess NO, and fully reduced protein was virtually fully oxidized by excess NO.¹ Given the reported importance of C₅₅₄'s oxidation state to its reactivity with NO, it is clear that knowing the extent of protein reduction at all times during a reaction is critical to fully understanding that reaction. The midpoint potentials of wild-type C₅₅₄ were previously obtained using UV/Vis spectropotentiometry and protein film voltammetry.^{2, 3} This chapter presents UV/Vis spectropotentiometric investigations of the F156A and F156H mutants of C₅₅₄, as well as a re-investigation of the wild type redox chemistry. UV/Vis spectropotentiometry is a combination of potentiometric titration and UV/Vis spectroscopy,^{4, 5} that we have found very useful for the deconvolution of midpoint potentials in multi-heme systems.^{6, 7} The primary goal of these studies was to obtain the heme midpoint potentials of the mutant proteins, but an important additional goal was to acquire full extinction coefficient spectra of the mutants and the wild type for use in future mechanistic investigations (Chapters 3-5). As will be seen, the experimental results also provide interesting insights about how hemes in a multi-heme system interact with each other during the reduction process.

2.2. Materials and Methods

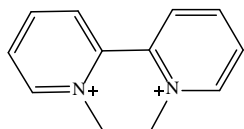
2.2.1. General materials. Gallocyanine, phenazine methosulfate, indigo tetrasulfonate, indigo carmine, hexammineruthenium(III) chloride, anthraquinone 1,5 disulfonic acid and methyl viologen were obtained from Acros. Safranin O and Anthraquinone sulfonic acid were obtained from Sigma-Aldrich. Diquat (6,7-dihydrodipyrido[1,2-a:2',1'-c]pyrazinediium dibromide, Table 2.1) was synthesized using the method described by Homer and Tomlinson.⁸ All experiments were performed in solutions buffered at pH 7.0 with 50 mM N-(2-hydroxyethyl) piperazine-N-ethanesulfonic (HEPES), which also contained 150 mM sodium chloride as an electrolyte. All solutions were prepared daily and manipulated in a nitrogen- filled glovebox.

Table 2.1. Mediators used for spectropotentiometry

Mediator	ϵ° (V vs SHE)	Concentration (μM)
Phenazine methosulfate	0.08	25
Gallocyanin	-0.020	25
Hexaammineruthenium(III) chloride	-0.020	100
Indigo tetrasulfonate	-0.030	25
Indigo trisulfonate	-0.080	25
Indigo carmine	-0.125	25
Anthraquinone 1,5-disulfonic acid	-0.175	25
Anthraquinone 2-sulfonic acid	-0.255	25
Safranin O	-0.289	25
Diquat ^a	-0.390	25
Methyl viologen	-0.449	25

^a

Diquat:



2.2.2. Protein purification and handling. The gene for wild-type C₅₅₄ was synthesized for optimal codon usage by Genscript, and included a ribosomal binding site, the leader sequence for the signal peptide of *S. oneidensis* small tetraheme *c*, and restriction enzyme digest sites (SacI + XbaI). The gene was cloned into the pUC-type vector pHSG299 (Takara), which confers kanamycin resistance, before being transformed into competent 5-alpha *Escherichia coli* (*New England Biolabs*) for verification of correct sequence. The C₅₅₄ construct was then electroporated into *S. oneidensis* tsp-c cells, which exhibit rifampicin resistance, for expression. The construct was also conjugated into *S. oneidensis* MR-1 as an alternative expression vehicle.

The phenylalanine at the 156 position of C₅₅₄ was mutated to alanine using site directed mutagenesis. The PCR was performed using phusion hotstart high fidelity DNA polymerase (Finnzymes). The primers for C₅₅₄F156A-F (GCTACCCCCGAAGTGGATGCAAAG) and C₅₅₄F156A-R (TGGGGTATAGGGTGCTTTGGCAC) were purchased from Integrated DNA technologies with phosphorylated 5' ends. The mutated PCR construct was ligated with T4 DNA ligase (New England biolabs) and transformed into competent WM3064 *E. coli* cells (gift from Coats lab UC-Berkeley). The WM3064 cells were used to transfer the mutated plasmid via conjugation into *S. oneidensis* MR-1 cells. The mutation for phenylalanine in the 156 position of C₅₅₄ to histidine was performed using the same protocol. The primers for C₅₅₄F156H-F (CATACCCCCG-AAGTGGATGCAAAG) and C₅₅₄F156H-R (TGGGGTATAGGGTGCTTTGGCAC) were purchased from Integrated DNA technologies with phosphorylated 5' ends.

Bacterial cultures were grown overnight at 30° C in 45 L batches of LB growth medium for wild type C₅₅₄. Attempts to scale the mutant cultures to 45 L proved unsuccessful, and these were grown in five 1 L cultures overnight at 30° C. The following purification protocol was

used for all forms of C₅₅₄. The bacteria were sedimented by centrifugation at 4400 rpm for 10 minutes, after which the cell pellet was re-suspended in a minimal volume of 20 mM HEPES buffer pH 7, containing 1 mM EDTA, 10 μ M leupeptin, and 500 μ M 4-(2-aminoethyl) benzenesulfonyl fluoride hydrochloride as protease inhibitors. The concentrated cell suspensions were stored at -80° C until needed. Cells were lysed using a sonic dismembrator (model CL-334) to release cell contents for purification, after which the solid cell debris was sedimented by centrifugation at 52k rpm for 30 minutes, and the clarified supernatant was decanted and kept for further purification steps.

Purification was effected in a two-step process. In the first step the cell lysate supernatant was loaded onto a 5 ml HiTrap SP cation exchange column (GE Healthcare) equilibrated with a 20 mM HEPES pH 7 loading buffer containing 1 mM EDTA (Buffer A). Once the protein was loaded and all non-bound proteins were washed off with Buffer A, a 200 ml linear gradient that started with Buffer A, and ended with 100% of an elution buffer consisting of 0.2 M NaCl in Buffer A (buffer B), was used to elute the protein. The C₅₅₄ fractions were desalted using dialysis in Buffer A, and concentrated to 1-2 mL using centrifugal concentration devices (Amicon Ultra-15 Centrifugal Filter Units Millipore). The protein was then passed through a G-50 (83 cm length, 26 mm diameter) size exclusion column equilibrated with Buffer A containing 0.15 M NaCl adjusted to pH 7.0. The purity of C₅₅₄ was assessed by the ratio of $A_{406\text{nm}}/A_{280\text{nm}}$ in the UV/visible spectra; samples exhibiting ratios above 5 were pooled. The final purity of the pooled sample was assessed by gel electrophoresis using a sodium dodecyl sulfate polyacrylamide gel.

The purified stock solution concentrations of C₅₅₄ wild type, F156A and F156H were initially determined using a pyridine hemochrome assay,⁹ after which the extinction coefficient

spectrum of each protein could be determined, and used to assess the concentrations of further samples. The λ_{max} at 406 nm is $3.97 \times 10^5 \text{ M}^{-1}\text{cm}^{-1}$ for wild type C_{554} , $3.81 \times 10^5 \text{ M}^{-1}\text{cm}^{-1}$ for F156A and $5.00 \times 10^5 \text{ M}^{-1}\text{cm}^{-1}$ for F156H (Fig. 2.1). Concentrated aliquots of purified C_{554} wild type, F156A and F156H (typically 100-500 μM), buffered with 50 mM HEPES pH 7 containing 1 mM EDTA, were flash frozen with liquid nitrogen and stored at -80 C until needed.

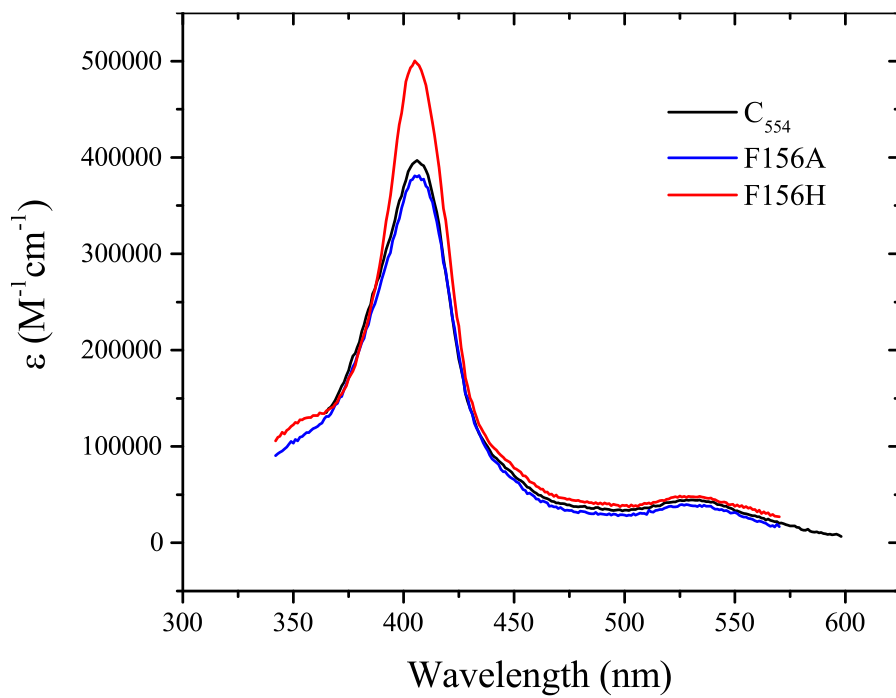


Figure 2.1. UV-Vis extinction coefficient spectra for wild-type C_{554} , and for the F156A and F156H mutants. The values at the 406 nm maximum were determined to be $3.97 \times 10^5 \text{ M}^{-1}\text{cm}^{-1}$ for wild type C_{554} , $3.81 \times 10^5 \text{ M}^{-1}\text{cm}^{-1}$ for F156A, and $5.00 \times 10^5 \text{ M}^{-1}\text{cm}^{-1}$ for F156H, by cross-reference to a pyridine hemochrome assay (see text for details).

2.2.3. UV-Vis spectropotentiometric titrations of C_{554} and its variants. UV/vis spectropotentiometry experiments were performed using a BASi Epsilon EC potentiostat to set the potential, and a CARY Bio 50 UV/vis spectrophotometer to collect spectra at 10 mV

intervals of applied potential. The complete apparatus was housed in an anaerobic glovebox. Controlled potentiometric electrolysis of the solution was performed in an optically transparent thin layer electrode (OTTLE) cuvette (Fig. 2.2), which was adapted from previously described designs.^{4,5} Solutions containing protein (typically 50-100 μM) and mediators (Table 2.1) were prepared in 50 mM HEPES, 150 mM NaCl, pH 7.0. The mediator concentrations were all 25 μM , except hexammineruthenium (III) chloride concentrations which were 100 μM . UV/Vis spectra were collected from +50 mV to -500 mV at 10 mV intervals (vs SHE). An Ag/AgCl

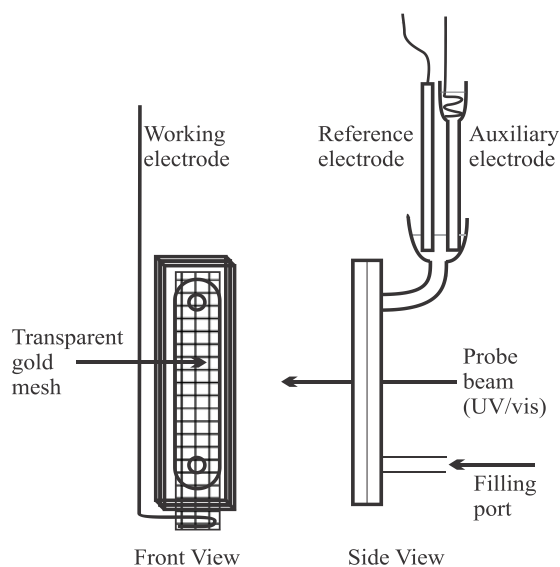
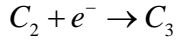
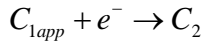
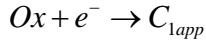


Figure 2.2. UV/Vis cell used for the spectropotentiometric titration of C_{554} and its variants. The quartz cuvette is a short pathlength (nominally 0.2 mm) demountable flow cell available commercially from Starna. The optically transparent gold mesh was obtained from Precision E-Forming, was sandwiched between the cuvette plates, and was connected to a copper wire using a conductive silver-containing glue (from GC Electronics). The edges of the cuvette were sealed with silicone adhesive (RTV108, Momentive). The cuvette could be filled from its lower filling port using a syringe. A small cup connected to the upper port by silicone tubing was partially filled with the protein solution, and provided a spot where the reference and auxiliary electrodes could make electrical contact. The actual pathlength of the cell with the gold foil in place was determined using a cytochrome *c* solution of known concentration. Note: for very long experiments the cup at the top should be covered to minimize evaporation of the protein solution.

electrode (BASi, Model RE-5B) was used as a reference, and a spiral platinum wire was used as the auxiliary electrode (Fig. 2.2). To correct for possible drift in the reference electrode, a cyclic voltammogram of methyl viologen (midpoint potential of -449 mV vs SHE ¹⁰) was performed before collecting data sets. Data were also collected for solutions containing identical mediator concentrations but no protein, and these were subtracted from corresponding protein data sets to correct for any spectral changes contributed by the mediators during the titration. The corrected data sets were analyzed with programs written in commercially available software packages Mathcad 15 (PTC software) and Origin 9.0 (Microcal Software), as described below and in Appendix 1.

2.3. Results

2.3.1. A spectropotentiometric study of wild type C₅₅₄. The blue traces in Fig. 2.3a show selected spectral changes observed when a solution initially containing 100 μ M C₅₅₄, and the mediator mixture of Table 2.1, was subjected to successively more negative applied potentials. Though C₅₅₄ has four hemes, analysis by singular value decomposition (SVD) ^{11, 12} shows that these spectra are linear combinations of just two component spectra. This result can be attributed to two causes. The first is that the two high potential hemes have identical (or nearly indistinguishable) midpoint potentials, so they reduce simultaneously, as has previously been reported. ^{2, 3} This leads to spectral changes that are indistinguishable from those that would accompany one-electron reduction of a single heme. To account for this fact we model our system with the reduction steps shown in Scheme 2.1. In this scheme C_{1app} is the concentration of what appears to be a 1-electron reduced C₅₅₄ species that accumulates as the applied potential is lowered, but is in fact a 2-electron reduced species. Thus, overall, the reduction of C₅₅₄ appears to take place in three 1-electron steps.



Scheme 2.1. Reduction of fully oxidized wild type C₅₅₄ (Ox) to the apparently 3-electron reduced form (C₃) in 1-electron steps (see text for details).

The second factor that reduces the number of SVD components contributing to the Fig. 2.3a spectra is that the two lowest potential hemes appear to make identically-shaped contributions to the extinction coefficient difference spectra of the 3- and 4-electron reduced C₅₅₄ species, though they reduce with different midpoint potentials. Based on this hypothesis, and the hypothesis of Scheme 2.1, we fit the Fig. 2.3a data using Eqs. 2.1 – 2.3, which are derived in Appendix 1, following a procedure similar to one used by our research group in the past.^{6, 7}

$$C_n = \frac{C_T \times \prod_{n=1}^3 E_n}{denom} \quad (2.1a)$$

Where, (2.1b)

$$denom = 1 + E_1[1 + E_2(1 + E_3)]$$

$$E_n = \exp\left[\frac{nF}{RT}(\varepsilon_n^o - \varepsilon_{app})\right] \quad (2.1c)$$

$$\Delta A_{\lambda, \varepsilon_{app}} = \left[\Delta \varepsilon_{HP(\lambda)} \cdot (C_{1app} + C_2 + C_3)_{\varepsilon_{app}} + \Delta \varepsilon_{LP(\lambda)} (0.5C_2 + C_3)_{\varepsilon_{app}} \right] \cdot \ell \quad (2.2)$$

$$\Delta \boldsymbol{\varepsilon} = \Delta \mathbf{A} \cdot [\mathbf{C}_{red} (\mathbf{C}_{red}^T \mathbf{C}_{red})^{-1}] \frac{1}{\ell} \quad (2.3a)$$

$$(\mathbf{C}_{red})_{\varepsilon_{app},1} = (C_{1app} + C_2 + C_3)_{\varepsilon_{app}}$$

$$(\mathbf{C}_{red})_{\varepsilon_{app},2} = (0.5C_2 + C_3)_{\varepsilon_{app}} \quad (2.3b)$$

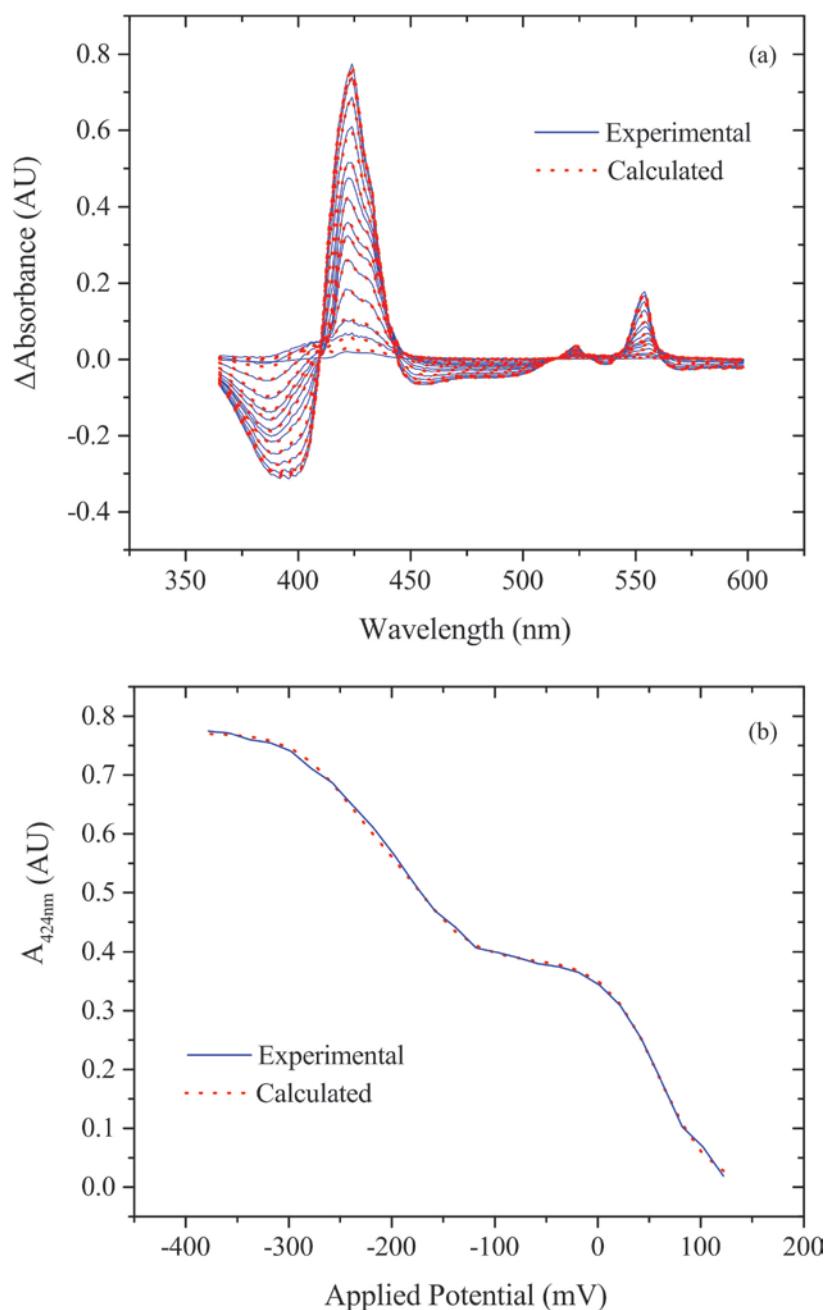


Figure 2.3. (a) SVD-processed difference spectra obtained for 100 μM wild-type C₅₅₄ at applied potentials of 102, 62, 22, -58, -138, -198, -238, -278, -318, and -358 mV versus the standard hydrogen electrode (SHE). Solid blue lines show the experimental data, whereas the dashed red lines show the calculated fits obtained using Eqs. 2.1 – 2.3. (b) A slice through the spectra from (a) taken at 424 nm, where the biggest changes in absorbance were observed; the solid blue trace represents the experimentally obtained data, the dashed red one the least-squares best fit using Eqs. 2.1 – 2.3.

Collectively, equations 2.1a – 2.1c are simply Nernst equations in exponential form for each of the reduced species C_n from Scheme 2.1 (the first reduced species being C_{1app}). In these equations C_T is the total C_{554} concentration in solution (determined apriori from the initial spectrum), \mathcal{E}_n^o is the midpoint potential associated with one-electron reduction of the (n–1)th reduced species, and \mathcal{E}_{app} is the applied potential. In Eq. 2.2 $\Delta A_{\lambda, \mathcal{E}_{app}}$ is the absorbance change at a given wavelength and applied potential, $\Delta \mathcal{E}_{HP(\lambda)}$ is the extinction coefficient difference at a given wavelength corresponding to the two high-potential hemes combined, $\Delta \mathcal{E}_{LP(\lambda)}$ is the extinction coefficient difference at a given wavelength corresponding to the two low-potential hemes combined, and ℓ is the pathlength of the cuvette. The concentrations of the reduced species C_{1app} , C_2 and C_3 in Eq. 2.2 are those specified by Eqs. 2.1, in which the midpoint potentials are adjustable parameters to be experimentally determined.⁶ Thus, for a given trial set of midpoint potentials one generates a corresponding set of concentrations C_{1app} , C_2 and C_3 for Eq. 2.2. Because the concentration matrix generated for Eq. 2.2 is not square, and thus has no inverse, for each trial set of midpoint potentials the pseudoinverse of the concentration matrix is constructed to obtain trial extinction coefficient spectra, as shown in Eq. 2.3.^{6, 13} In this equation the first column of the $\Delta \mathbf{\epsilon}$ matrix is the extinction coefficient difference spectrum for the high potential hemes, and the second column is for the low potential hemes. The two columns of the matrix \mathbf{C}_{red} are as defined in Eq. 2.3b. Once $\Delta \mathbf{\epsilon}$ has been obtained for a trial set of midpoint potentials, a theoretical matrix of absorbances $\Delta \mathbf{A}_{calc}$ can be obtained as the product $\Delta \mathbf{\epsilon} \cdot \mathbf{C}_{red}^T \cdot \ell$; the sum of squares corresponding to $\Delta \mathbf{A} - \Delta \mathbf{A}_{calc}$ is then used as the figure of merit to obtain the best midpoint potential parameter set.

The red traces in Fig. 2.3a are examples of the best fits to the experimentally acquired spectra, and were obtained by manually adjusting the trial set of midpoint potentials until the sum of

squares was minimized. Figure 2.3b shows a ΔA versus ε_{app} slice through all of the collected spectra at 424 nm, the wavelength at which the largest absorbance change was detected. Fits at other wavelengths were equally good. The best midpoint potential parameter set obtained from the fitting routine is recorded in Table 2.2 (page 54). Figure 2.4a provides the calculated extinction coefficient difference spectra $\Delta\varepsilon_{\text{HP}}$ and $\Delta\varepsilon_{\text{LP}}$ (the columns of matrix $\Delta\varepsilon$) obtained by the fitting procedure. By adding $\Delta\varepsilon_{\text{HP}}$ and $\Delta\varepsilon_{\text{LP}}$ to the extinction coefficient spectrum of fully oxidized C_{554} , one can generate absolute extinction coefficient spectra for 2- and 4-electron reduced protein (Fig. 2.4b).

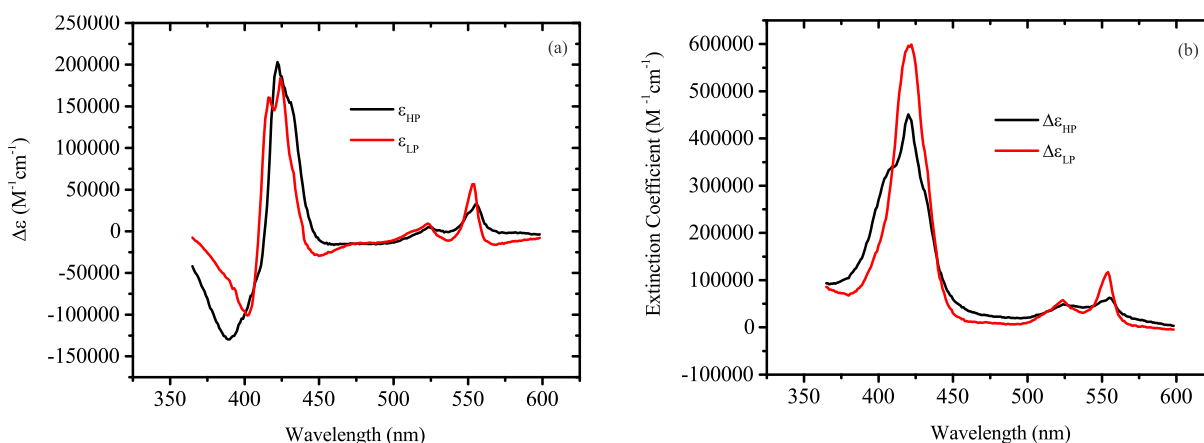
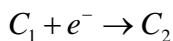
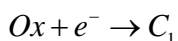


Figure 2.4. (a) Extinction coefficient difference spectra obtained by fitting the Fig. 2.3 data using Eqs. 2.1 – 2.3. (b) Absolute extinction coefficient spectra obtained by adding $\Delta\varepsilon_{\text{HP}}$ and $\Delta\varepsilon_{\text{LP}}$ to the previously obtained extinction coefficient spectrum of fully oxidized C_{554} (Fig. 2.1).

2.3.2. A spectropotentiometric study of the F156A C_{554} mutant. A challenge of running spectropotentiometric experiments with proteins that contain multiple redox-active centers is that they can take a very long time, even when using thin low-volume cuvettes. During this time unwanted processes such as buffer evaporation can take place, which then must be corrected for. This can be done when necessary, but if possible it is more convenient to split

the experiment into two steps. Both the C₅₅₄ wild type and the F156A mutant have two sets of two reduction events that are well separated from each other, which makes it easy to split their spectropotentiometric titrations into two separate experiments. The experiment with wild type described in Section 2.3.1 was done in two steps, but the spectra were then combined and fitted as one set. The experiments with the F156A mutant were also done in two steps, but the two datasets so obtained were treated separately, as will now be described.

The blue traces in Fig. 2.5a show selected spectral changes observed when a solution initially containing 60.8 μM of F156A, and the mediator mixture of Table 2.1, was subjected to successively more negative applied potentials in the range from 92 to –68 mV. SVD analysis¹¹,¹² shows that these spectra are linear combinations of two component spectra, which were hypothesized to correspond to the isolated first two reduction events in the tetraheme system (Scheme 2.2). Based on Scheme 2.2, one can readily derive (Appendix 1) the fitting equations



Scheme 2.2. First two steps in the reduction of fully oxidized F156A mutant (*Ox*) in 1-electron steps.

2.4 and 2.5, which are analogous (though simpler) to the Eqs. 2.1 and 2.2 used to fit the wild type spectra. The Fig. 2.5a spectra could then be fit with Eqs. 2.4 and 2.5 in a manner completely analogous to that used in fitting the Fig. 2.3 spectra. The red traces in Fig. 2.5a are

$$C_n = \frac{C_T \times \prod_{n=1}^2 E_n}{denom} \quad (2.4a)$$

$$denom = 1 + E_1(1 + E_2) \quad (2.4b)$$

$$\Delta A_{\lambda, \varepsilon_{app}} = \left[\Delta \varepsilon_{1(\lambda)} \cdot C_{1(\varepsilon)} + \Delta \varepsilon_{2(\lambda)} \cdot C_{2(\varepsilon)} \right] \cdot \ell \quad (2.5)$$

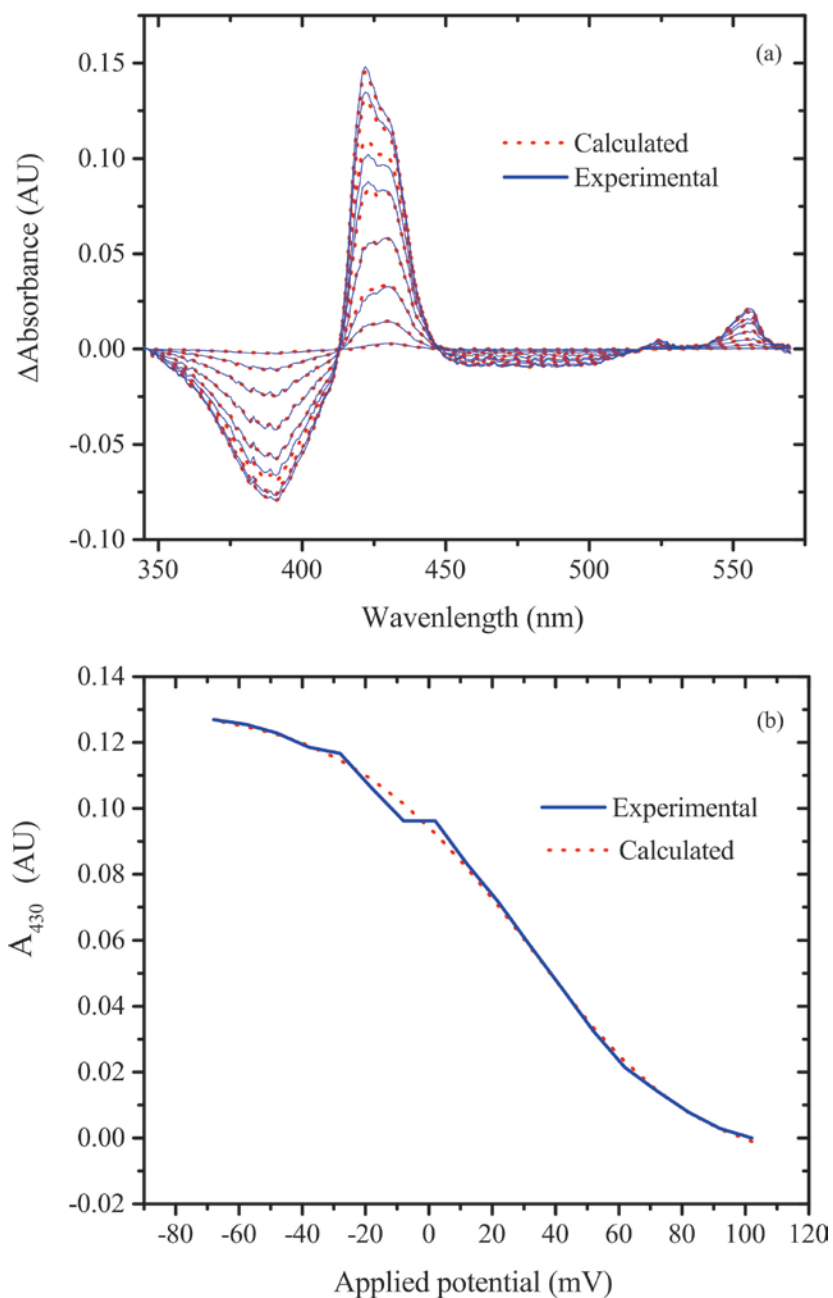


Figure 2.5. (a) SVD-processed difference spectra obtained for 60.8 μ M of the F156A C₅₅₄ mutant at applied potentials of 92, 72, 52, 32, 12, -8, -28, -48, and -68 mV versus SHE. Solid blue lines show the experimental data, whereas the solid red lines show the calculated fits obtained using Eqs 2.4 and 2.5. (b) A slice through the spectra from (a) taken at 430 nm, where absorbance changes due to the high-spin 5-coordinate heme predominate. The solid blue trace represents the experimentally obtained data, the dashed red one the least-squares best fit using Eqs. 2.4 and 2.5.

examples of the best fits to the experimentally acquired spectra obtained using Eqs. 2.4 and 2.5. Figure 2.5b shows a ΔA versus ε_{app} slice through all of the collected spectra at 430 nm, the wavelength at which the absorbance changes due to the high-spin 5-coordinate heme predominate. Fits at other wavelengths were equally good. The best midpoint potential parameter set ε'_1 and ε'_2 obtained from the fitting routine is recorded in Table 2.2. (page 54). Figure 2.6a provides the calculated extinction coefficient difference spectra $\Delta\varepsilon_1$ and $\Delta\varepsilon_2$ obtained by the fitting procedure. By adding $\Delta\varepsilon_1$ and $\Delta\varepsilon_2$ to the extinction coefficient spectrum of fully oxidized F156A mutant, one can generate absolute extinction coefficient spectra for 1- and 2-electron reduced protein (Fig. 2.6b).

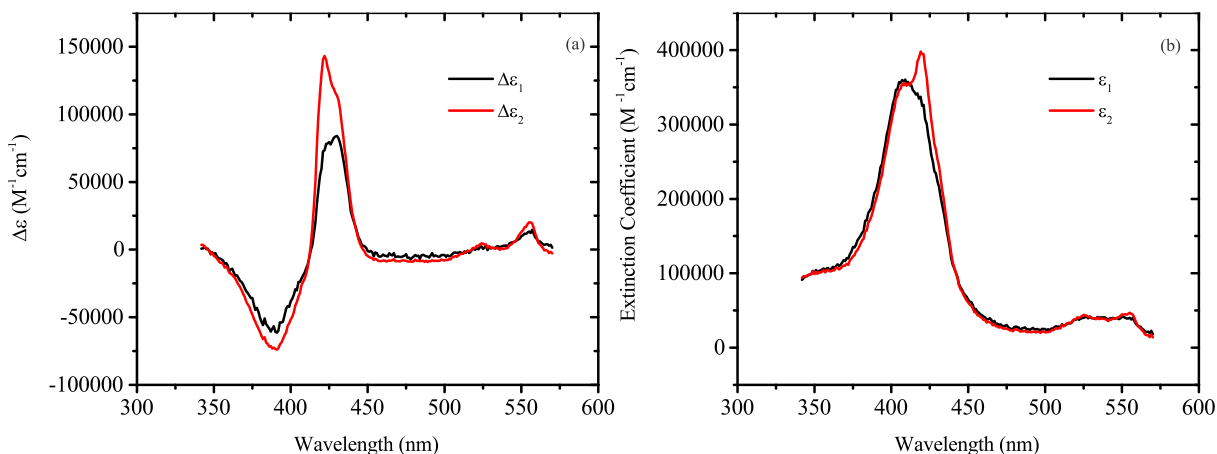
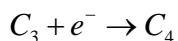
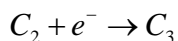


Figure 2.6. (a) Extinction coefficient difference spectra associated with formation of C_1 and C_2 (Scheme 2.2), obtained by fitting the Fig. 2.5 data using Eqs. 2.4 and 2.5. (b) Absolute extinction coefficient spectra of C_1 and C_2 , obtained by adding $\Delta\varepsilon_1$ and $\Delta\varepsilon_2$ to the previously obtained extinction coefficient spectrum of fully oxidized F156A C_{554} mutant (Fig. 2.1).

The midpoint potentials of the low-potential F156A hemes were obtained in a separate experiment, in which an applied potential of -80 mV vs SHE was first used to reduce the protein by two electrons in a single step. The assumption, justified below, was that at this potential the

2-electron reduced species was the only one present in significant quantities. The spectral changes obtained relative to the spectrum at -80 mV applied potential, as the potential was further decreased to -500 mV, are shown as blue traces in Fig. 2.7a; the reaction mixture for this experiment initially contained 60.5 μM of F156A, and the mediator mixture of Table 2.1. SVD analysis^{11, 12} showed that these spectra are linear combinations of two component spectra, which were hypothesized to arise from the final two reduction events in the tetraheme system (Scheme 2.3). Based on Scheme 2.3 one can readily derive (Appendix 1) the fitting equations 2.6 and 2.7,



Scheme 2.3. Reduction of 2-electron reduced F156A mutant (C_2) to the 4-electron reduced moiety (C_4) in 1-electron steps.

which are analogous Eqs. 2.4 and 2.5 above, except that now $\Delta\varepsilon_n = \varepsilon_n - \varepsilon_2$. The red traces in Fig. 2.7a are examples of the best fits to the experimentally acquired spectra obtained using Eqs. 2.6 and 2.7. Figure 2.7b shows a ΔA versus ε_{app} slice through all of the collected spectra at 423 nm,

$$C_n = \frac{C_T \times \prod_{n=3}^4 E_n}{denom} \quad (2.6a)$$

$$denom = 1 + E_3(1 + E_4) \quad (2.6b)$$

$$\Delta A_{\lambda, \varepsilon_{app}} = \left[\Delta\varepsilon_{3(\lambda)} \cdot C_{3(\varepsilon)} + \Delta\varepsilon_{4(\lambda)} \cdot C_{4(\varepsilon)} \right] \cdot \ell \quad (2.7)$$

the wavelength at which the largest spectral changes are observed. Fits at other wavelengths were equally good. The best midpoint potential parameter set ε'_3 and ε'_4 obtained from the fitting routine is recorded in Table 2.2. Figure 2.8a provides the calculated extinction coefficient difference spectra $\Delta\varepsilon_3$ and $\Delta\varepsilon_4$ obtained by the fitting procedure. By adding $\Delta\varepsilon_3$ and $\Delta\varepsilon_4$ to the

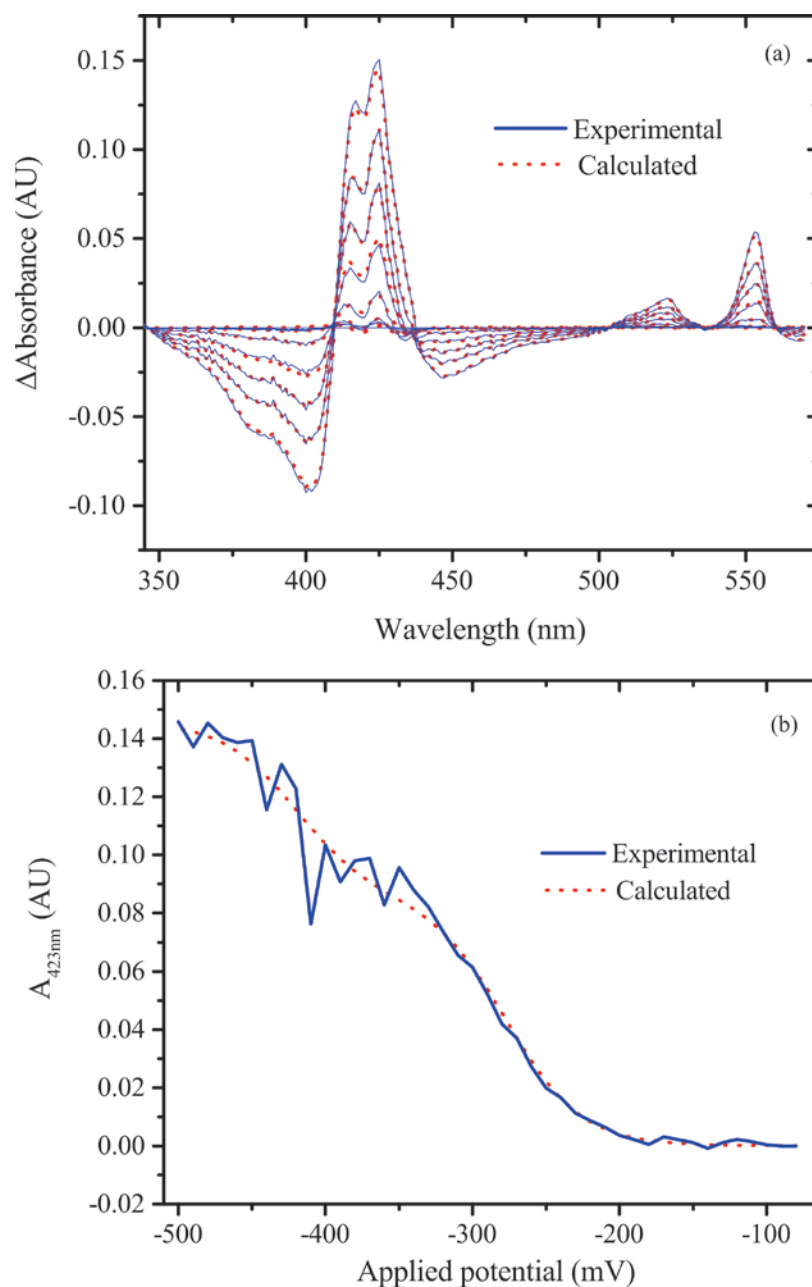


Figure 2.7. (a) SVD-processed difference spectra obtained for 60.5 μM of the F156A C₅₅₄ mutant at applied potentials of -80 (flat line), -120, -160, -200, -240, -280, -320, -400, and -480 mV versus SHE. Solid blue lines show the experimental data, whereas the solid red lines show the calculated fits obtained using Eqs 2.6 and 2.7. (b) A slice through the spectra from (a) taken at 423 nm, where largest absorbance changes are observed. The solid blue trace represents the experimentally obtained data, the dashed red one the least-squares best fit using Eqs. 2.6 and 2.7.

extinction coefficient spectrum of 2-electron reduced F156A mutant (Fig 2.6b), one can generate absolute extinction coefficient spectra for 3- and 4-electron reduced protein (Fig. 2.8b).

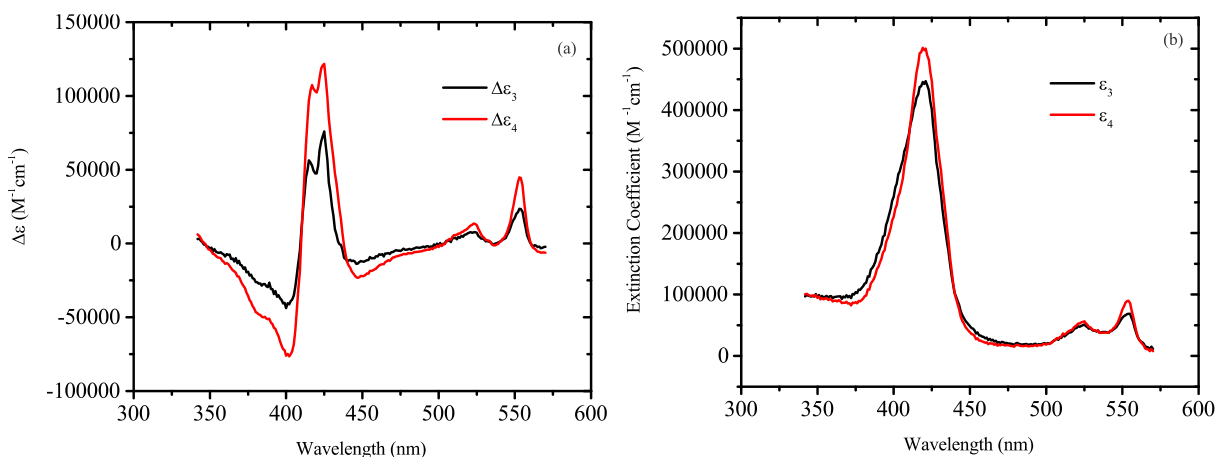


Figure 2.8. (a) Extinction coefficient difference spectra associated with formation of C_3 and C_4 of F156A (Scheme 2.3), obtained by fitting the Fig. 2.7 data using Eqs. 2.6 and 2.7. (b) Absolute extinction coefficient spectra of C_3 and C_4 , obtained by adding $\Delta\epsilon_3$ and $\Delta\epsilon_4$ to ϵ_2 (shown in Fig. 2.6b).

Figure 2.9 shows the fractional abundance of $C_1 - C_4$ calculated using Eqs. 2.4 and 2.6, and the experimentally calculated parameter set from Table 2.2 (page 54). Note that at the applied potential of -80 mV virtually all (94%) of the F156A is present as the 2-electron reduced species, thus justifying the decision to generate the Fig 2.7a difference spectra using the -80 mV spectrum as the reference. In retrospect, an even better choice would have been $\epsilon_{app} = -140$ mV, where $\sim 99\%$ of the protein is present as the 2-electron reduced species; however, the extinction coefficient spectra obtained with the -80 mV choice proved adequate for our experiments.

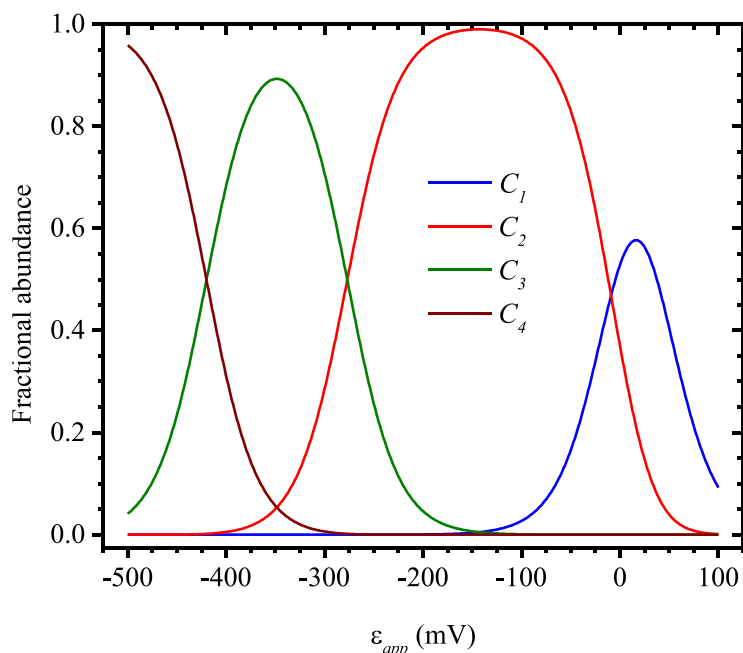


Figure 2.9. Fractional abundance of each reduced F156A species as a function of applied potential, calculated using Eqs. 2.4 and 2.6, and the midpoint potential parameter set from Table 2.2. Based on the calculations, the 2-electron reduced species will constitute ~94% of the total C_{554} at $\epsilon_{app} = -80$ mV, with the remaining 6% being 1-electron reduced

2.3.3. A spectropotentiometric study of the F156H C_{554} mutant. The blue traces in Fig. 2.10a show selected spectral changes observed when a solution initially containing 52 μM of the F156H C_{554} mutant, and the mediator mixture of Table 2.1, was subjected to successively more negative applied potentials. The entire spectropotentiometric titration had to be done in a single experiment because, unlike the situation encountered with F156A, there was no applied potential at which a single species of the F156H mutant predominated. Analysis by singular value decomposition (SVD)^{11, 12} showed that the Fig. 2.10a spectra are linear combinations of four component spectra, as would be expected if each reduction event in the tetraheme system resulted in formation of a spectrally and electrochemically distinguishable species. The

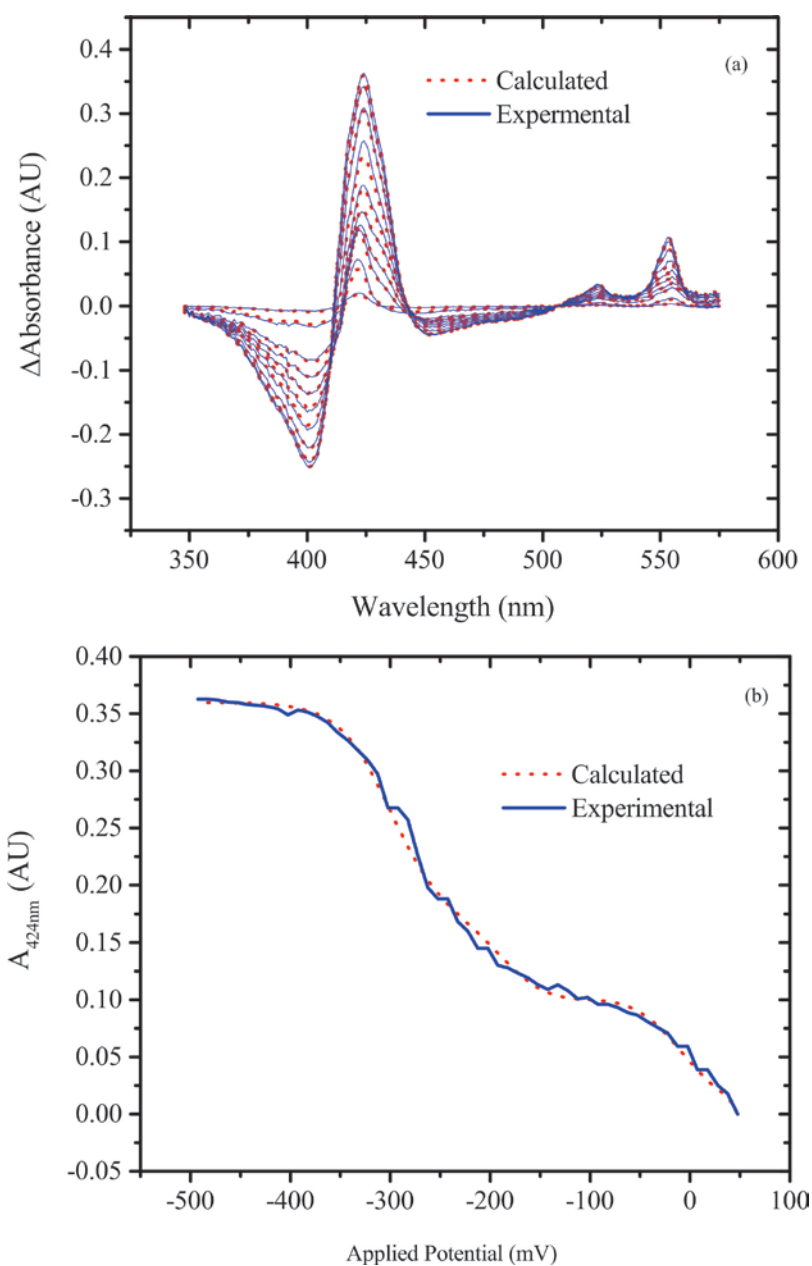
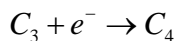
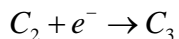
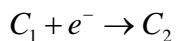
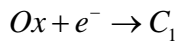


Figure 2.10. (a) SVD-processed difference spectra obtained for 52 μM of the F156H C₅₅₄ mutant at applied potentials of 38.5, -2.5, -122.5, -162.5, -202.5, -242.5, -285.5, -322.5, -362.5 and -482.5 mV versus SHE. Solid blue lines show the experimental data, whereas the solid red lines show the calculated fits obtained using Eqs 2.8 and 2.9. (b) A slice through the spectra from (a) taken at 424 nm, where the largest absorbance changes are observed. The solid blue trace represents the experimentally obtained data, the dashed red one the least-squares best fit using Eqs. 2.8 and 2.9.

experiment was thus modelled using Scheme 2.4 and Eqs. 2.8 and 2.9. This is the most straightforward of the cases encountered so far, and the required equations are derived in



Scheme 2.4. Reduction of fully oxidized F156H mutant (*Ox*) to the 4-electron reduced moiety in 1-electron steps.

detail in Appendix 1. The red traces in Fig. 2.10a are examples of the best fits to the experimentally acquired spectra obtained using Eqs. 2.8 and 2.9. Figure 2.10b shows a ΔA versus ε_{app} slice through all of the collected spectra at 424 nm, where the largest absorbance

$$C_n = \frac{C_T \times \prod_{n=1}^4 E_n}{denom} \quad (2.8a)$$

$$denom = 1 + E_1 \{1 + E_2 [1 + E_3 (1 + E_4)]\} \quad (2.8b)$$

$$\Delta A_{\lambda, \varepsilon_{app}} = \ell \cdot \sum_{n=1}^4 \Delta \varepsilon_{n(\lambda)} \cdot C_{n(\varepsilon_{app})} \quad (2.9)$$

changes are observed. Fits at other wavelengths were equally good. The best midpoint potential parameter set $\varepsilon^o_1 - \varepsilon^o_4$ obtained from the fitting routine is recorded in Table 2.2. Figure 2.11a provides the calculated extinction coefficient difference spectra $\Delta \varepsilon_1 - \Delta \varepsilon_4$ obtained by the fitting procedure. By adding these to the extinction coefficient spectrum of fully oxidized F156H mutant one can generate absolute extinction coefficient spectra for 1- to 4-electron reduced protein (Fig. 2.11b).

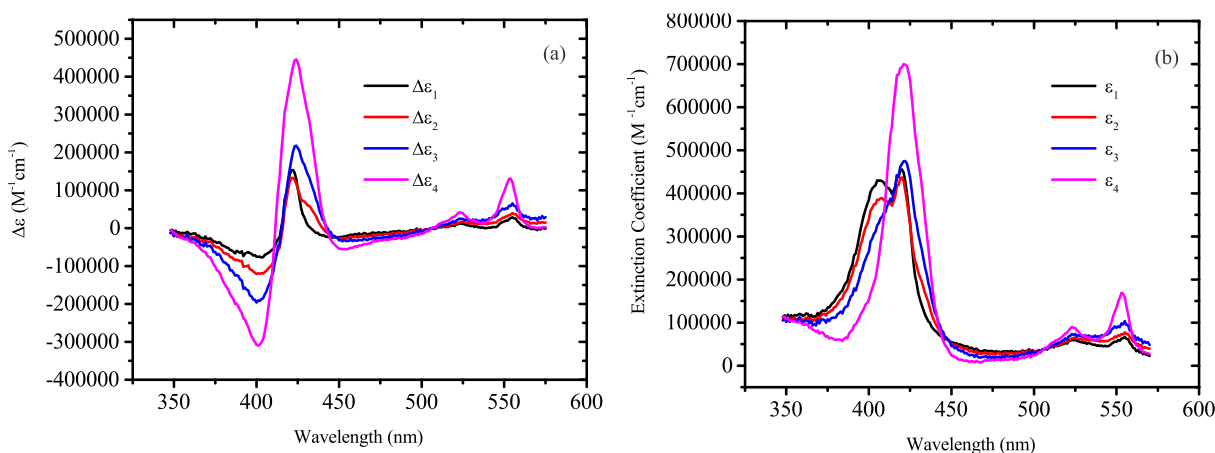


Figure 2.11. (a) Extinction coefficient difference spectra associated with formation of $C_1 - C_4$ of F156H (Scheme 2.4), obtained by fitting the Fig. 2.10 data using Eqs. 2.8 and 2.9. (b) Absolute extinction coefficient spectra of $C_1 - C_4$, obtained by adding $\Delta\epsilon_1 - \Delta\epsilon_4$ to the mutant's ϵ_{ox} spectrum. Note that the split Soret seen in the Fig. 2.4a and 2.8a difference spectra are not seen in (a) above. This is because $\Delta\epsilon_3$ and $\Delta\epsilon_4$ in this case are obtained by subtraction of the fully oxidized spectra, whereas in the earlier cases the reduced difference spectra were relative to partially reduced intermediates.

2.4. Discussion

2.4.1. Wild type C₅₅₄. The midpoint potentials of wild type C₅₅₄ were previously obtained by UV/Vis spectropotentiometric analysis at selected wavelengths,² and by protein film voltammetry (PFV).³ Table 2.2 (page 54) shows that the results from this work are in reasonable agreement with both sets of prior results. One does see variations of up to 35 mV in the midpoint potentials of the lowest potential heme obtained by the different methods, but such variations are comparatively minor given the complexity of the system being analyzed. Similar variations were found when various methods were used to extract the midpoint potentials of the decaheme enzyme cytochrome *c* nitrite reductase (ccNiR),^{6, 7} and the variations appear to arise primarily from experimental biases introduced by the various measuring techniques.⁶

Table 2.2. Midpoint potentials of wild type and variant C₅₅₄ hemes (in volts vs. the standard hydrogen electrode) obtained in this work, and in previous investigations.

Midpoint potential	Wild type C ₅₅₄		F156A mutant	F156H mutant	
	UV/Vis spectropotentiometry	Protein film voltammetry ^c	UV/Vis spectropotentiometry ^a		
\mathcal{E}^o_1	0.059 ^a	0.047 ^b	0.050	0.042	-0.006
\mathcal{E}^o_2	0.059 ^a	0.047 ^b	0.032	-0.009	-0.111 (heme II)
\mathcal{E}^o_3	-0.164 ^a	-0.147 ^b	-0.183	-0.277	-0.187
\mathcal{E}^o_4	-0.248 ^a	-0.276 ^b	-0.283	-0.420	-0.301

^a. This work

^b. Reference²

^c. Reference³

Though the two high potential hemes give rise to a single SVD component and midpoint potential in the spectropotentiometric titration, their extinction coefficient spectra show distinct contributions from the low-spin heme I and the high-spin heme II (Fig. 1.4a). Reduced low spin *c* hemes typically display absorbance maxima below 430 nm, whereas the maxima for high-spin *c*-hemes are always above 430 nm.^{2, 6, 14} Thus, in the Fig. 2.4a difference spectrum $\Delta\mathcal{E}_{HP}$, the main maximum at 422 nm is assigned to the low-spin heme I, and the prominent shoulder at 431 nm to the high-spin heme II. The shoulder due to the high-spin heme also appears at 431 nm in the absolute spectrum of Fig. 2.4b, but the main peak attributable to the low-spin heme is slightly shifted to 420 nm relative to the difference spectrum. It should be noted that even though hemes I and II appear to reduce with identical midpoint potentials in UV/Vis spectropotentiometric titrations, in PFV experiments heme I reduces slightly before heme II (50 mV vs 32 mV, Table 2.2).³ This result is also in agreement with a prediction from a theoretical study of C₅₅₄ reduction.¹⁵

Mössbauer and EPR spectroscopic analyses also show that hemes I and II reduce simultaneously in the first C₅₅₄ reduction event.¹⁶ Both the oxidized and reduced states of the high-spin heme stand out clearly in the Mössbauer spectrum, so the reduction process can be directly monitored by this method. The EPR spectrum of fully oxidized C₅₅₄ shows that hemes (I and III) and (II and IV) form two weakly antiferromagnetically coupled pairs. Following the first reduction event both couplings disappear, leaving signals typical of two magnetically isolated low-spin ferric hemes that can be assigned as hemes III and IV. The reduction order of the low potential hemes was also assigned by EPR because they give rise to distinct signals. The aromatic rings of histidine axial ligands for heme III are nearly parallel to each other, and give rise to a rhombic EPR spectrum, while those of heme IV are closer to perpendicular and give rise to a so-called HALS (highly axial low spin) signal. In EPR spectropotentiometric titrations, the rhombic signals disappear at higher potential.¹⁶

A notable feature of the component spectra obtained from the spectropotentiometric titration is the split Soret observed in the difference spectrum Δ_{ELP} that arises from the two low potential hemes (Fig. 2.4a, the Soret band displays distinct maxima at 416 and 424 nm). This feature was documented but not discussed in an earlier study of C₅₅₄ electrochemistry.² Unlike hemes I and II, hemes III and IV exhibit distinct midpoint potentials, and the earlier EPR studies¹⁶ clearly showed that heme III reduces before heme IV. Yet our SVD analysis showed that reduction of each low potential heme made spectroscopically identical contributions (Section 2.3.1), so each heme *individually* must be contributing to both the 416 nm and the 424 nm bands.

Prior to its observation in C₅₅₄, a split Soret spectrum was documented for a *Desulfovibrio desulfuricans* c-heme protein that was in fact named the “split-Soret cytochrome”

(SSC).¹⁷ The SSC is a homodimer in which each protomer contains two *c*-hemes; as with C₅₅₄, a split Soret with maxima at 415 and 424 nm appeared upon heme reduction.¹⁸ The only similarity between C₅₅₄ and the SSC is that both proteins contain pairs of parallel but offset hemes that come within Vander Waals contact (see Fig. 1.4a for the C₅₅₄ case); indeed, C₅₅₄ hemes I and III overlay quite nicely on the heme pair from a SSC protomer.¹⁹ C₅₅₄ Hemes II and IV don't overlay on the SSC pair, but their arrangement is similar in that they too are offset parallel, and within Vander Waals contact.¹⁹ We therefore propose that the necessary condition for generating a split Soret is to have a pair of offset but parallel reduced hemes in Vander Waals contact. In C₅₅₄ two such pairs are available under reducing conditions: hemes I-III and II-IV (Fig. 1.4a). Thus, as heme III reduces, the heme I-III pair makes a first contribution to the split Soret of Fig. 2.4a. At lower applied potentials heme IV reduces, at which point the heme II-IV pair makes a second contribution. The fact that the heme I-III and II-IV pairs provide spectroscopically indistinguishable contributions (Fig. 2.4a) suggests that geometric constraints other than having the hemes parallel offset and within Vander Waals contact have minimal importance.

2.4.2. F156A mutant of C₅₅₄. As noted in Chapter 1, the likely physiological role of C₅₅₄ is to accept electrons from hydroxylamine oxidase (HAO).¹⁹ HAO and C₅₅₄ each possess a pair of nearly equipotential hemes, with the HAO pair having midpoint potential values of ~0mV,^{15, 20, 21} and the C₅₅₄ pair having them at ~45 mV (Table 2.2).^{2, 3, 15, 16} Based on this observation it has been suggested that HAO is primed to accept electrons from the substrate hydroxylamine two at a time, and C₅₅₄ is optimized to accept these electrons from HAO pairwise as well.^{3, 15} This hypothesis is supported by PFV studies that demonstrate some cooperativity in reduction of the high-potential C₅₅₄ hemes, and perhaps also some rectification behavior, which speeds electron transfer from HAO to C₅₅₄ relative to the reverse process.³ The F156A mutation

somewhat perturbs the delicate balance between hemes I and II so that the first and second reduction events are now about 50 mV apart instead of roughly isopotential (Table 2.2).

Interestingly, the spectral changes that accompany the first two reduction events are not consistent with sequential reduction of first one discrete heme and then another. Though the 1- and 2-electron reduced species now display discrete extinction coefficient spectra (Fig. 2.6), both species exhibit overlapping bands attributable to reduction of distinct hemes in the Soret region of their difference spectra (Fig. 2.6a). One band has an absorbance maximum near 422 nm characteristic of low-spin ferrous heme, while the other peaks near 430 nm, which is more characteristic of high-spin hemes (see Section 2.4.1). Figure 2.5a shows that in the early stages of heme reduction the 430 nm band is slightly higher than the 422 nm one, but that as the reduction progresses the 422 nm band becomes more prominent. This is reflected in the component extinction coefficient difference spectra of Fig. 2.6a. We interpret this to mean that in the 1-electron reduced species the single electron is delocalized between hemes I and II, but exhibits a slight preference for residing on the high-spin heme II. When C₅₅₄ is reduced further to the 2-electron reduced species both hemes I and II will be reduced equally, at which point the 422 nm band predominates as it does in the high potential component of the wild type (Fig. 2.4a). This interpretation should be further tested in the future using EPR spectropotentiometry. Evidence for electron delocalization similar to that described here was previously observed during spectropotentiometric reduction of the homodimeric decaheme enzyme cytochrome *c* nitrite reductase,^{6, 7} and in computational studies of HAO reduction.¹⁵ The phenomenon may prove to be widespread in multi-heme proteins.

A final notable feature of the first two F156A reduction events is that the midpoint potential associated with 1-electron reduced F156A generation very nearly matches ϵ_{HP}^o

attributable to simultaneous reduction of hemes I and II in the wild type (Table 2.2), while the midpoint potential for generating the 2-electron reduced species is shifted 50 mV down to -9mV . At first glance this result seems counterintuitive. In the 1-electron reduced species the electron appears to have a preference for residing on heme II, which is the one affected by the mutation, and yet the midpoint potential of the first reduction event is very close to that of the wild type. On the other hand the midpoint potential of the second reduction event is more profoundly influenced by the mutation, even as more electron density is being added to heme I, which is far from the mutated site. The observation highlights the complexity of interactions in multi-heme systems, and is worthy of further study.

As is the case for the wild type, the extinction coefficient difference spectra of the F156A mutant low potential hemes both exhibit split Soret bands, with maxima at 417 and 424 nm (Fig. 2.8a). Though SVD analysis shows distinct spectral changes associated with the two reduction events, the difference spectra for the 3- and 4-electron reduced species in Fig. 2.8a are visually quite similar, and it is quite possible that some of the differences are due simply to varying admixtures of noise into the two components. Interestingly, the midpoint potentials for F156A's third and fourth reduction events are significantly more affected by the mutation than the high-potential hemes, despite the fact that the mutation was in the vicinity of the high-potential heme II (Table 2.2). In both cases the midpoint potentials shifted more than 100 mV to the negative. Thus, \mathcal{E}_3° shifted from -166 mV in the wild type to -277 mV in the mutant, while \mathcal{E}_4° shifted from -276 mV to -420 mV . Once again this demonstrates the significant global effects that local changes can have on midpoint potentials in multi-heme proteins. Crystallographic analysis of wild type C₅₅₄ showed that structural changes accompanying heme reduction are relatively minor.²² Notably though, the most pronounced changes take place in the vicinity of hemes III

and IV. The biggest changes occur in a loop between residues 175 and 179 that terminates at one of the heme III axial histidine ligands (His 179), and in the rearrangement of one of the heme IV propionates.²² His 179 is not so far from residue 156, and it is possible that the 156 mutation affects the loop. Similarly, the proximity between Hemes II and IV (Fig. 1.4) could allow any structural changes at heme II that accompany the H156A mutation to influence the arrangement of the heme IV propionate in the redox process. These possibilities should be explored in future structural studies of the mutant.

2.4.3. F156H mutant of C₅₅₄. Unlike the F156A change, mutation of F156 to a histidine has a profound effect on the heme II midpoint potential, which shifts from 45 mV in the wild type to -111 mV in F156H (Table 2.2). Histidine is a potential ligand for heme II, and we propose that in oxidized F156H it binds to the metal center, thus stabilizing the higher oxidation state. In keeping with this hypothesis the spectral changes associated with loss of oxidized heme II display maximum amplitude at about 400 nm (Figs. 2.10a and 2.11a), which is consistent with the oxidized species now being low-spin.² By contrast, for both the wild type and the F156A mutant the spectral changes associated with loss of oxidized heme II have maximum amplitudes at around 390 nm, which is characteristic of high-spin oxidized hemes.² Note however that the new band that *appears* as heme II is reduced is at 430 nm (Figs. 2.10 and 2.11), which as mentioned before is characteristic of high-spin ferrous hemes.² Thus it seems that while the ferric heme II of F156H is low-spin and 6-coordinate, the ferrous form reverts back to high-spin 5-coordinate like the wild-type and F156A.

Two factors could drive a 5-coordinate to 6-coordinate transition during heme oxidation. First, donation of electron density by formation of an additional covalent bond to the ferric heme would help to dissipate the extra formal charge associated with the higher oxidation state.

Second, the porphyrin rings of ferric hemes are typically easier to distort from planarity,²² and this in turn might make it easier for ferric heme II to adopt a conformation amenable to establishing an iron-histidine bond with a comparatively distant ligand. In the converse case, as the heme II of F156H reduces from the ferric to ferrous form, one could envision the porphyrin ring becoming more rigid, and pulling the iron away from the H156, at the same time that additional stabilizing electron density became less desirable. Future crystallographic studies of the F156H mutant, in oxidized and reduced states, will be needed in order to test the proposed hypothesis.

Interestingly, the midpoint potentials of the two low-potential hemes of F156H are much closer to those of the wild type than they are to those of F156A. Histidine is much closer in size to phenylalanine than is alanine, so it seems quite reasonable that the F156A substitution would lead to larger structural changes at remote locations near hemes III and IV than the F156H switch; this in turn would lead to greater changes in the midpoint potentials.

2.5 Summary

The midpoint potentials of all the hemes in C₅₅₄, and in the F156A and F156H variants, were determined using spectropotentiometric analysis. The midpoint potentials obtained for the wild type protein were comparable to those obtained in earlier studies,^{2, 3} which provided validation for the methodology used herein. By taking complete spectra at each applied potential and then analyzing the data globally, we were also able to obtain full extinction coefficient spectra for the protein species at varying stages of reduction.

The heme II midpoint potential of F156H was profoundly altered from the wild type value, shifting about 170 mV to the negative. This may be showing that the histidine ligand in

the variant binds to the previously vacant ferric heme II axial site, thus stabilizing the oxidized state. Consistent with this interpretation, the UV/Visible spectrum of fully oxidized F156H exhibited increased absorbance at 409 nm relative to the wild type, which suggests that the mutant protein has 4 low-spin ferrihemes, rather than three low-spin and one high-spin as seen in the wild type. Upon reduction of heme II though, the spectrum of F156H exhibits a band at 430 nm characteristic of high-spin ferrohemes, which suggests that His 156 dissociates from the heme when this reduces.

In contrast to the case with F156H, the midpoint potentials of hemes I and II in F156A were only slightly shifted relative to the wild type. On the other hand, the midpoint potentials of the low-potential hemes III and IV were shifted about 100 mV to the negative by mutating Phe156 to Ala, whereas mutation of Phe156 to His had minimal impact on these hemes. It appears that the substitution of bulky Phe by the small Ala significantly alters the conformation of the protein backbone, which in turn affects the environment of distant hemes enough to substantially alter their midpoint potentials.

To summarize, the midpoint potential values obtained in this chapter for the hemes of C₅₅₄ and its variants, together with the corresponding full extinction coefficient spectra, provided a level of understanding of these multi-heme systems that was only obtainable from a global analysis. The following chapters rely heavily on the insights obtained herein to explore the interaction with NO of C₅₅₄ and its variants.

2.6. References

- [1] Upadhyay, A. K., Hooper, A. B., and Hendrich, M. P. (2006) NO reductase activity of the tetraheme cytochrome c(554) of *Nitrosomonas europaea*, *J. Am. Chem. Soc.* *128*, 4330-4337.
- [2] Arciero, D. M., Collins, M. J., Haladjian, J., Bianco, P., and Hooper, A. B. (1991) Resolution of the 4 Hemes of Cytochrome-C554 from *Nitrosomonas-Europaea* by Redox Potentiometry and Optical Spectroscopy, *Biochemistry* *30*, 11459-11465.
- [3] Pulcu, G. S., Elmore, B. L., Arciero, D. M., Hooper, A. B., and Elliott, S. J. (2007) Direct electrochemistry of tetraheme cytochrome *c*₅₅₄ from *Nitrosomonas europaea*: redox cooperativity and gating, *J. Am. Chem. Soc.* *129*, 1838-1839.
- [4] Heineman, W. R., Norris, B. J., and Goelz, J. F. (1975) Measurement of enzyme E⁰ values by optically transparent thin layer electrochemical cells, *Anal. Chem.* *47*, 79-84.
- [5] Pilkington, M. B. G., Coles, B. A., and Compton, R. G. (1989) Construction of an optically transparent thin layer electrode cell for use with oxygen-sensitive species in aqueous and non-aqueous solvents, *Anal. Chem.* *61*, 1787-1789.
- [6] Youngblut, M., Judd, E. T., Srajer, V., Sayyed, B., Goelzer, T., Elliott, S. J., Schmidt, M., and Pacheco, A. A. (2012) Laue crystal structure of *Shewanella oneidensis* cytochrome *c* nitrite reductase from a high-yield expression system, *J. Biol. Inorg. Chem.* *17*, 647-662.
- [7] Stein, N., Love, D., Judd, E. T., Elliott, S. J., Bennett, B., and Pacheco, A. A. (2015) Correlations between the electronic properties of *Shewanella oneidensis* cytochrome *c* nitrite reductase (ccNiR) and its structure: effects of heme oxidation state and active site ligation, *Biochemistry* *54*, 3749-3758.

- [8] Homer, R. F., and Tomlinson, T. E. (1960) The stereochemistry of the bridged quaternary salts of 2,2'-bipyridyl, *J. Chem. Soc.*, 2498-2503.
- [9] Berry, E. A., and Trumpower, B. L. (1987) Simultaneous determination of hemes a, b, and c from pyridine hemochrome spectra, *Anal. Biochem.* 161, 1-15.
- [10] Watanabe, T., and Honda, K. (1982) Measurement of the extinction coefficient of the methyl viologen cation radical and the efficiency of its formation by semiconductor photocatalysis, *J. Phys. Chem.* 86, 2617-2619.
- [11] Press, W. H., Teukolsky, S. A., Vetterling, W. T., and Flannery, B. P. (2007) Numerical Recipes the art of scientific computing, 3rd ed., pp 65-75, Cambridge University Press, New York, NY.
- [12] Henry, E. R., and Hofrichter, J. (1992) Singular Value Decomposition: Application to Analysis of Experimental Data, In *Meth. Enzymol.* (Brand, L., and Johnson, M. L., Eds.), pp 129-192, Academic Press, San Diego.
- [13] Press, W. H., Teukolsky, S. A., Vetterling, W. T., and Flannery, B. P. (2007) Numerical Recipes the art of scientific computing, 3rd ed., pp 773-839, Cambridge University Press, New York, NY.
- [14] Marritt, S. J., Kemp, G. L., Xiaoe, L., Durrant, J. R., Cheesman, M. R., and Butt, J. N. (2008) Spectroelectrochemical characterization of a pentaheme cytochrome in solution and as electrocatalytically active films on nanocrystalline metal-oxide electrodes, *J. Am. Chem. Soc.* 130, 8588-8589.
- [15] Kurnikov, I. V., Ratner, M. A., and Pacheco, A. A. (2005) Redox equilibria in hydroxylamine oxidoreductase. Electrostatic control of electron redistribution in multielectron oxidative processes, *Biochemistry* 44, 1856-1863.

- [16] Upadhyay, A. K., Petasis, D. T., Arciero, D. M., Hooper, A. B., and Hendrich, M. P. (2003) Spectroscopic characterization and assignment of reduction potentials in the tetraheme cytochrome c(554) from *Nitrosomonas europaea*, *J. Am. Chem. Soc.* *125*, 1738-1747.
- [17] Liu, M. C., Costa, C., Coutinho, I. B., Moura, J. J. G., Moura, I., Xavier, A. V., and LeGall, J. (1988) Cytochrome components of nitrate and sulfate-respiring *Desulfovibrio desulfuricans* ATCC 27774, *J. Bacteriol.* *170*, 5545-5551.
- [18] Matias, P. M., Morais, J., Coelho, A. V., Meijers, R., Gonzalez, A., Thompson, A. W., Sieker, L., LeGall, J., and Carrondo, M. A. (1997) A preliminary analysis of the three-dimensional structure of dimeric di-haem split-Soret cytochrome *c* from *Desulfovibrio desulfuricans* ATCC 27774 at 2.5 Å resolution from MAD phasing method: a novel cytochrome fold with a stacked-haem arrangement, *J. Biol. Inorg. Chem.* *2*, 507-514.
- [19] Iverson, T. M., Arciero, D. M., Hsu, B. T., Logan, M. S. P., Hooper, A. B., and Rees, D. C. (1998) Heme packing motifs revealed by the crystal structure of the tetra-heme cytochrome c554 from *Nitrosomonas europaea*, *Nat. Struct. Biol.* *5*, 1005-1012.
- [20] Collins, M. J., Arciero, D. M., and Hooper, A. B. (1993) Optical Spectropotentiometric Resolution of the Hemes of Hydroxylamine Oxidoreductase - Heme Quantitation and Ph-Dependence of E_m , *J. Biol. Chem.* *268*, 14655-14662.
- [21] Hendrich, M. P., Petasis, D., Arciero, D. M., and Hooper, A. B. (2001) Correlations of structure and electronic properties from EPR spectroscopy of hydroxylamine oxidoreductase, *J. Am. Chem. Soc.* *123*, 2997-3005.
- [22] Iverson, T. M., Arciero, D. M., Hooper, A. B., and Rees, D. C. (2001) High-resolution structures of the oxidized and reduced states of cytochrome c554 from *Nitrosomonas europaea*, *J. Biol. Inorg. Chem.* *6*, 390-397.

Chapter 3

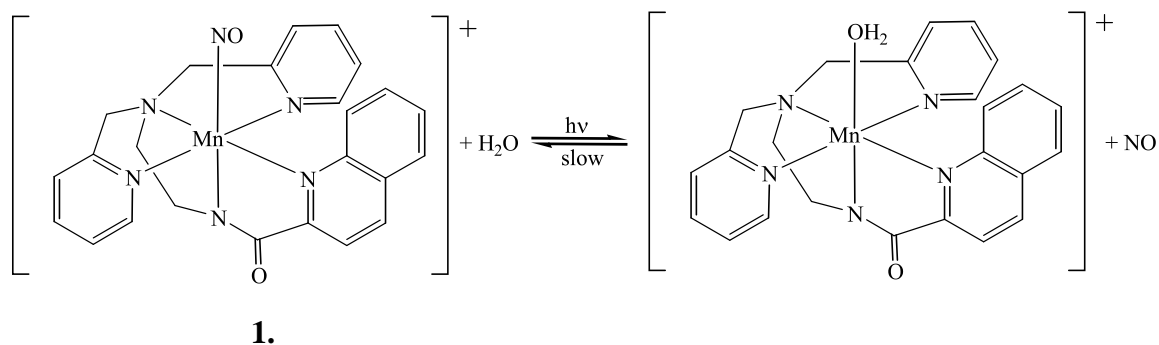
The reaction of wild type cytochrome *c*₅₅₄, at various stages of reduction, with photo-generated nitric oxide

3.1. Introduction

As was reviewed in Chapter 1 (Section 1.3), a 2006 paper reported that under certain conditions *C*₅₅₄ exhibits NO reductase activity, in addition to acting as an electron transport protein.² The Pacheco group was intrigued by this result for two reasons. First, it seemed surprising that such reactivity could be catalyzed in a heme vacant site that appears barely large enough to bind a single NO molecule (Fig. 1.5). All other known NO reductases either have di-iron active sites with enough space for two NO molecules (Section 1.5), or a mono-iron site that can accommodate NO and NH₂OH in close proximity (Section 1.6). Second, Upadhyay et al. reported that *C*₅₅₄-catalyzed reduction of NO to N₂O occurred most rapidly at very low applied potentials.² Such an observation appears to contradict a paradigm that has been developing in the Pacheco group for some years now, according to which NO is predicted to reduce to NH₄⁺ in the presence of powerful reductants, and to N₂O only in the presence of less powerful ones (Section 1.7). Given these apparent contradictions, we decided to re-examine the purported NO reductase activity of *C*₅₅₄.

A major challenge in studying the reactivity of NO under reducing conditions is that NO reacts directly with many commonly used reducing agents such as dithionite or methyl viologen monocation radical. This can make it difficult to deconvolute NO reduction catalyzed by a species such as *C*₅₅₄ from the direct interaction, which is often rapid. Furthermore, except at very low concentrations, NO gas reacts rapidly with even trace oxygen, which can easily

confound experimental results unless oxygen is rigorously excluded. In the past the Pacheco group has found the light-activated NO precursor $[\text{Mn}(\text{PaPy}_2\text{Q})\text{NO}]\text{ClO}_4$ (species **1**, Scheme 3.1,³ where PaPy_2Q is the pentadentate ligand *N,N*-bis(2-pyridylmethyl)-amine-*N*-ethyl-2-quinoline-2-carboxamide) to be extremely useful for investigating reactions of proteins with NO.^{4,5} This species releases NO within less than 1 μs of being irradiated with a laser pulse, and is thus ideally suited for investigating fast reactions of this gas. Furthermore, by quickly generating an aliquot of NO in situ, the method often allows the reaction of interest to be investigated before unwanted side reactions of NO, with residual oxygen or reducing agents, can proceed to a significant extent. In this chapter we re-evaluate the reactivity of NO with C_{554} under rigorously anaerobic conditions, exploiting the properties of **1** to minimize interference from unwanted side reactions.



Scheme 3.1. Photolytic cleavage of **1** to produce an aquo species and free NO.

3.2. Materials and Methods

3.2.1. General materials. Common chemicals were obtained from Fisher Scientific, VWR or Sigma-Aldrich unless specified otherwise. Hexammineruthenium(II) chloride ($\text{Ru}(\text{NH}_3)_6\text{Cl}_2$), hexammineruthenium(III) chloride ($\text{Ru}(\text{NH}_3)_6\text{Cl}_3$), and methyl viologen were obtained from Acros. Zinc powder was from Fisher Scientific. The light-activated NO precursor

1 (Scheme 3.1) was prepared by the method of Eroy-Reveles et al.³ The pH-jump activated NO precursor 1-(*N,N*-diethylamino)diazene-1-ium-1,2-diolate (DEANO) was prepared as described by Drago and Paulik.^{6, 7}

3.2.2. General instrumentation. Routine UV/vis spectra were obtained using one of three Cary 50 (Varian) spectrophotometers available to the Pacheco group. Two of these spectrophotometers are housed in gloveboxes for obtaining spectra of air-sensitive samples. Bulk electrolysis was carried out using a BASi Epsilon EC potentiostat to set the appropriate potential. An Ag/AgCl electrode was used as a reference (BASi model RE-5B), and was periodically standardized by comparison with the methyl viologen couple as described in Chapter 2.

3.2.3. Protein handling. The C₅₅₄ purification protocol can be found in Chapter 2. All experiments with purified C₅₅₄ were performed in solutions buffered with 50 mM HEPES pH 7, containing 1 mM EDTA. Solutions were prepared and manipulated in a nitrogen-filled glovebox. Stock solutions were prepared daily in the glovebox, and stored in a refrigerator at 4° C until needed.

In addition to C₅₅₄ and buffer, solutions for use in laser-initiated time-resolved spectroscopy also contained a suitable reducing agent as described below, and varying concentrations of the NO-generating photosensitive species **1**. Such solutions had to be prepared and kept in a darkened room at all times; a red safe-light was used to provide the minimal illumination needed to prepare the samples.

Stock solutions of two-electron reduced C₅₅₄ for laser-initiated time resolved spectroscopy were prepared in a bulk electrolysis cell by applying potentials of –50 mV vs SHE

to solutions initially containing 200 μM $\text{Ru}(\text{NH}_3)_6^{3+}$, 150 mM NaCl (as supporting electrolyte) and oxidized protein stock in standard HEPES buffer. Stock solutions containing only $\text{Ru}(\text{NH}_3)_6^{3+/2+}$ mixtures were prepared separately in a bulk electrolysis cell by applying potentials of -50 mV vs SHE to solutions initially containing 200 μM $\text{Ru}(\text{NH}_3)_6^{3+}$ and 150 mM NaCl (as supporting electrolyte) in standard HEPES buffer. Finally, stock solutions of species **1** were prepared by adding aliquots of the stock 200 μM $\text{Ru}(\text{NH}_3)_6^{3+/2+}$ mixtures to solid **1**. Reaction mixtures for each given experiment all contained the same volumes of stock C_{554} solution, but varying volumes of the stock **1** and 200 μM $\text{Ru}(\text{NH}_3)_6^{3+/2+}$ solutions.

Four-electron reduced C_{554} for laser-initiated time resolved spectroscopy was generated by gently stirring solutions containing the diluted oxidized protein stock, species **1** and methyl viologen (MV_{ox} , 3 μM) in a buffered suspension of zinc powder. The MV_{ox} was added to the suspension to act as a mediator between the solid zinc and the dissolved protein. After 30 min stirring was stopped, and the solid Zn was allowed to settle out in preparation for spectroscopic experiments. At this point the methyl viologen was fully reduced to the monocation radical (MV_{red}), as verified by UV/Vis spectroscopy.

Concentrations of C_{554} , as well as the extent of the protein's reduction, in the reaction mixtures used for laser spectroscopy and stopped-flow experiments, were assessed by UV/Vis spectroscopy using the independently obtained extinction coefficient spectra of the fully oxidized, 2-electron and 4-electron reduced C_{554} (see Chapter 2).

3.2.4. Laser-initiated time-resolved spectroscopic experiments. Samples for laser-initiated time-resolved experiments were prepared in the glovebox, in 1.5×1.5 mm fluorimeter cuvettes (Starna) stoppered with greased ground glass caps. Nitric oxide was generated

photochemically in the cuvettes by irradiating species **1** with 5 ns, 500 nm laser pulses from an OPO tunable laser (Opotec Rainbow Vis); NO release from the complex occurred in less than 1 μ s. The laser pulse was delivered through a fiber optic cable, and was focused to a spot of 5 mm diameter that homogeneously irradiated the entire cuvette window; this arrangement minimized artifacts due to irradiated solution diffusing out of the volume being probed. The laser pulse energies were measured daily before experiments were started using a Scientech AC2501 bolometer. The laser was tuned to deliver roughly 3 mJ/pulse (with ~10% variability from shot to shot), which for a 5 mm spot amounted to energy intensity of about 15 mJ/cm². Such laser pulses were found to release NO in concentrations of approximately 10% of [**1**] at low concentrations of **1**, but the NO yield decreased progressively due to self-screening in the cuvette as [**1**] increased towards 1 mM and beyond.⁸ The Mn product formed after release of NO is unreactive on the time scale recorded.³ Time resolved UV/vis spectra following the laser pulse were collected on an OLIS RSM 1000 spectrophotometer in rapid-scanning mode 1, which allowed complete spectra in the range from 361.9 nm – 587.2 nm to be collected at a rate of 62 scans/sec. The laser pulse entered a cuvette window perpendicular to the spectrophotometer's probe beam. Because the laser pulse irradiated the full window, the pathlength through the irradiated solution was 1.5 mm, equal to the cuvette's pathlength.

3.2.5. Data analysis. All data were analyzed using programs written within the commercially available software packages Origin version 6.0 or later (Microcal Software), or Mathcad 13 or later (PTC Software). The analysis strategies used in our laboratories have been previously described in general terms in references 9-13. Strategies more specific to analyzing kinetic data, including the background for the equations appearing in the Results and Discussion below, can be found in references 4,5,14.

3.3. Results

3.3.1. The reaction of photo-generated NO with two-electron reduced C₅₅₄. Figure 3.1 shows the spectral changes observed after a solution initially containing 0.9 mM of the NO generating species **1** (Scheme 3.1), 6 μM C₅₅₄ and 200 μM Ru(NH₃)₆²⁺ was exposed to a 500 nm, 5 ns laser pulse, which fragments **1** to release NO (Scheme 3.1). Under these conditions the hemes of C₅₅₄ with the highest potential (Fig 1.4a, hemes I and II) are reduced, while the lower potential hemes (Fig 1.4a, hemes III and IV) remain oxidized. The raw time-resolved UV/vis spectra were first subjected to singular value decomposition (SVD) to determine the number of spectral components and smooth out noise.^{15, 16} The SVD analysis showed that only three components were needed to faithfully reconstruct a noise-reduced absorbance matrix. The SVD-treated data were then fit to Eq. 3.1 using a global fitting routine.^{4, 5} In Eq. 3.1 spectral component Λ_0 is present immediately after the laser pulse (taken as t_0), component Λ_1 grows in exponentially in a process governed by the rate constant k_{obs} , and component Λ_2 grows in linearly with time. The data were fit to Eq. 3.1 with a Mathcad program that allowed k_{obs} to be manually adjusted, after which a pseudoinverse could be calculated to generate trial values of a matrix Λ

$$\Delta A_{\lambda,t} = \Lambda_{0(\lambda)} + \Lambda_{1(\lambda)}(1 - e^{-k_{obs}t}) + \Lambda_{2(\lambda)}t \quad (3.1)$$

that contained the spectral components.^{4, 5} The value of k_{obs} was adjusted until the least-squares difference between the experimental absorbance values and the matrix of $\Delta A_{\lambda,t}$ values obtained from Eq. 3.1 was minimized.

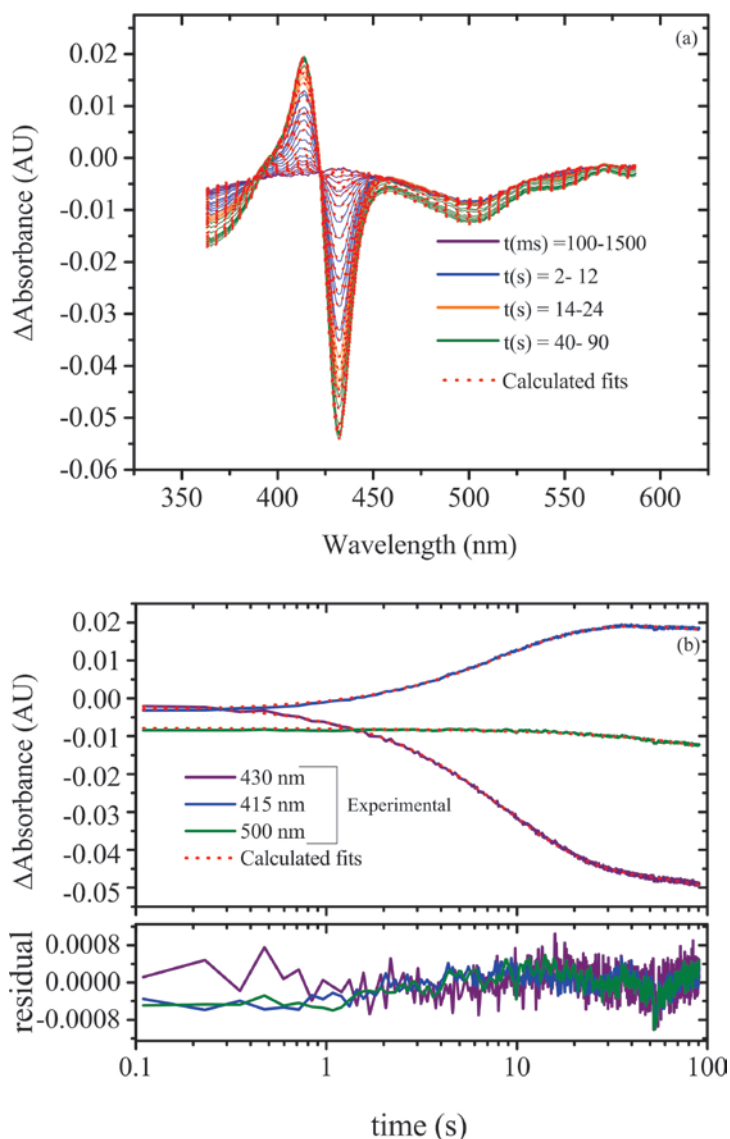


Figure 3.1. (a) Spectral changes at selected times observed when a solution initially containing 0.9 mM of the NO generating species **1**, 6 μM C_{554} and 200 μM $\text{Ru}(\text{NH}_3)_6^{2+}$ was exposed to a 500 nm, 5 ns laser pulse, which fragments **1** to release NO. The purple traces track the first 1500 ms at 100 ms intervals, the blue traces are at one-second intervals, the orange traces are at two-second intervals, and the green traces are at 10-second intervals. The red traces are the least-squares best fits using Eq. 3.1. (b) Changes in absorbance vs time are plotted for 415 nm, 430 nm and 500 nm, where individual species make significant contributions; the red traces are from the least-squares best fits using Eq. 3.1.

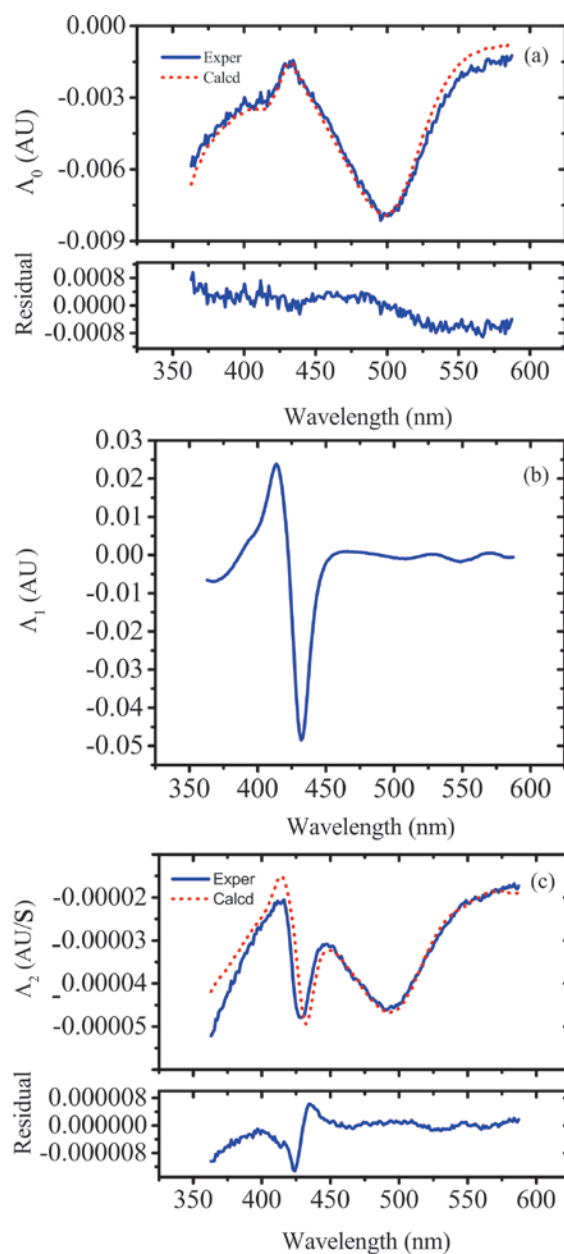


Figure 3.2. The spectral components Λ_0 - Λ_2 generated by fitting the SVD-processed Fig. 3.1 data to Eq 3.1 (blue traces). The red traces were generated with the independently known extinction coefficient spectrum of species **1** and small admixtures of Λ_1 . From the fit of Λ_0 (a) one can calculate that 31 μM of NO were generated by the laser pulse in this experiment. The fit of Λ_2 (c) mainly reflects the amount of **1** photolyzed per second due to the spectrophotometer probe beam; the NO so generated then nitrosylates additional C_{554} .

Figure 3.2 shows the spectral components obtained from the fitting process. The component Λ_0 (Fig. 3.2a) arises from the denitrosylation of species **1** within the dead-time of the experiment. This component was fit with the independently known extinction coefficient spectrum of species **1**, and the amount of NO generated by the laser pulse in the experiment was determined to be 31 μM from this fit. The component Λ_1 (Fig. 3.2b) grows in exponentially, and is attributed to nitrosylation of the reduced 5-coordinate heme II of C_{554} .² Finally, component Λ_2 (Fig. 3.2c) grows in linearly, and arises from the release of NO from species **1** caused by the spectrophotometer probe beam irradiation during the experiment (similar linear components are seen when collecting UV/Vis time series of solutions containing only species **1**). The Λ_2 component was fit using the independently known extinction coefficient spectrum of species **1**, with an admixture of component Λ_1 attributable to the extra C_{554} nitrosylation that accompanied the continued slow addition of NO. Small admixtures of the C_{554} nitrosylation spectrum Λ_1 are also seen in the Λ_0 component, but this is probably an artifact of the data reduction procedure, based on observations obtained by subjecting synthetic data of similar intensity and noisiness to the same procedure (including SVD analysis).

The analysis described in Figs. 3.1 and 3.2 was repeated with solutions containing varying concentrations of **1** and a nominally constant concentration of C_{554} . These experiments showed that k_{obs} varied linearly with the amount of NO generated by the laser pulses (Fig. 3.3). A least-squares fit of the data provided a non-zero intercept (red trace, Fig. 3.3), which suggests that exposure of 2-electron reduced C_{554} to photo-generated NO results in establishment of an equilibrium between the reduced C_{554}^{2-} and its nitrosylated form (C_{554}^{2-} and $\text{C}_{554}^{2-}(\text{NO})$, respectively, Scheme 3.2, page 81), whose position and rate of establishment depend visibly on

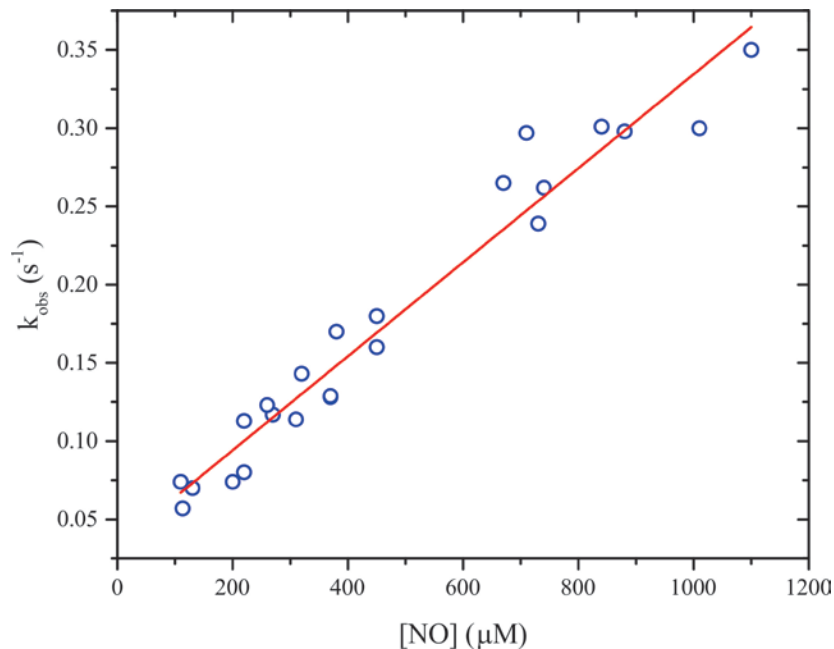


Figure 3.3. Plot of k_{obs} associated with appearance of the exponential component Λ_1 (Eq. 3.1), versus NO concentration obtained by fitting the corresponding t_0 component Λ_0 . Red trace: least-squares fit of the data to a straight line (Eq. 3.2). Slope = $3000 \pm 140 \text{ M}^{-1}\text{s}^{-1}$; Intercept = $0.034 \pm 0.009\text{s}^{-1}$; these are assigned as k_{on} and k_{off} , respectively as defined in Scheme 3.2 and Eq. 3.2.

the amount of NO present. Accordingly, the value of k_{obs} at a given NO concentration will be given by Eq. 3.2 (Appendix 2). Note that in all cases the amount of NO generated by the laser pulse exceeded the amount of C_{554} nitrosylated by a sufficient amount to maintain pseudo

$$k_{obs} = k_{off} + k_{on}[\text{NO}] \quad (3.2)$$

first-order conditions. From the linear fit to the Fig. 3.3 data, rate constant values of $3000 \pm 140 \text{ M}^{-1}\text{s}^{-1}$ and $0.034 \pm 0.009 \text{ s}^{-1}$ were obtained for k_{on} and k_{off} , respectively. An equilibrium constant K_{eq} of $(9 \pm 2) \times 10^4 \text{ M}^{-1}$ for the Scheme 3.2 nitrosylation was subsequently calculated from the ratio k_{on}/k_{off} . In addition to predicting a linear dependence of k_{obs} on $[\text{NO}]$ as shown in Eq. 3.2, the Scheme 3.2 (page 81) reversible nitrosylation model also predicts (Appendix 2) that

the amplitude of the Λ_1 component should depend hyperbolically on [NO], as shown in Eq. 3.3.

In principle, this relationship provides an independent method for obtaining K_{eq} ; however,

$$\Lambda_{1(\lambda)} = \frac{\Lambda_{1\max(\lambda)}[\text{NO}]}{K_{eq}^{-1} + [\text{NO}]} \quad (3.3)$$

in practice this proved unworkable due to large spectrum-to-spectrum scatter, which could not be completely corrected for. In attempts to analyze the amplitude information the values of $\Lambda_{1(\lambda)}$ obtained by fitting data to Eq. 3.1 were first converted to apparent extinction coefficient values by dividing the original $\Lambda_{1(\lambda)}$ values (in absorbance units) by the total C_{554} concentrations and cell pathlength. In addition, because the Λ_1 spectra showed pronounced baseline swings from experiment to experiment, the differences $\Lambda_{1(415)} - \Lambda_{1(433)}$, in which baseline variations should cancel out, were obtained from the Λ_1 spectra to be used in their place (415 nm and 433 nm are the wavelengths at which maximum absorbance positive and negative deflection was observed in Fig. 3.2b).

Figure 3.4 shows the differences $\Lambda_{1(415)} - \Lambda_{1(433)}$ obtained from each apparent extinction coefficient spectrum as a function of the NO present in solution. These data were fit to Eq. 3.4, which has the same hyperbolic form as Eq. 3.3. The Fig. 3.4 data were fit in two ways. The

$$\Lambda_{1(415)} - \Lambda_{1(433)} = \frac{\Delta\Lambda_{1\max}[\text{NO}]}{K_{eq}^{-1} + [\text{NO}]} \quad (3.4)$$

Fig. 3.4 red trace was obtained by fixing K_{eq} at the value obtained from the Fig. 3.3 fit, $(9 \pm 2) \times 10^4 \text{ M}^{-1}$ (see above). Despite the scatter in the Fig. 3.4 data, the red trace at least looks plausible. Furthermore, one can use the $\Delta\Lambda_{1\max}$ parameter obtained from the fit to then calculate reasonable estimates of the full extinction coefficient difference spectrum, $\Lambda_{1\max}$ (Eq. 3.3), which should accompany conversion of all available C_{554}^{2-} to the nitrosylated $\text{C}_{554}^{2-}(\text{NO})$ (Scheme 3.2,

page 81). The green trace in Fig. 3.4 was obtained by allowing both K_{eq} and $\Delta\Lambda_{1max}$ to be automatically adjusted by the fitting program. Surprisingly this trace was not much different from the red one, showing that convergence was still possible despite the data scatter, though the

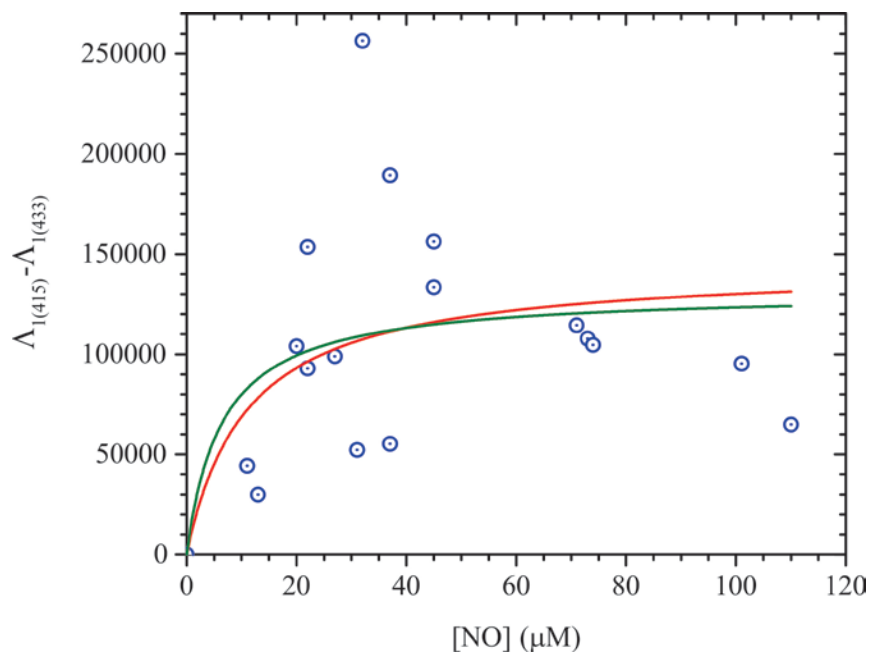


Figure 3.4. Blue circles: $\Lambda_{1(415)} - \Lambda_{1(433)}$ differences obtained from the Λ_1 components, plotted against the NO concentrations obtained by fitting the corresponding to components Λ_0 (see text for details). The red and green traces were least-squares best fits to Eq. 3.4. For the red trace the value of K_{eq}^{-1} was fixed using the k_{off}/k_{on} ratio obtained from the Fig. 3.3 fit to Eq. 3.2, while for the green trace both K_{eq}^{-1} and $\Delta\Lambda_{1max}$ in Eq. 3.4 were treated as adjustable parameters.

error in the K_{eq} value obtained from the fit was enormous: $(2\pm 3)\times 10^5 \text{ M}^{-1}$. Thus, while the amplitude data do not provide reliable estimates of the K_{eq} value, they are at least consistent with the results obtained by plotting k_{obs} vs [NO] (Fig. 3.3).

3.3.2 The reaction of photo-generated NO with four-electron reduced C554. Figure 3.5 shows the spectral changes observed after a solution initially containing 4 μM C554, 0.75 mM of the NO generating species **1** (Scheme 3.1), and 3 μM of methyl viologen reduced by zinc

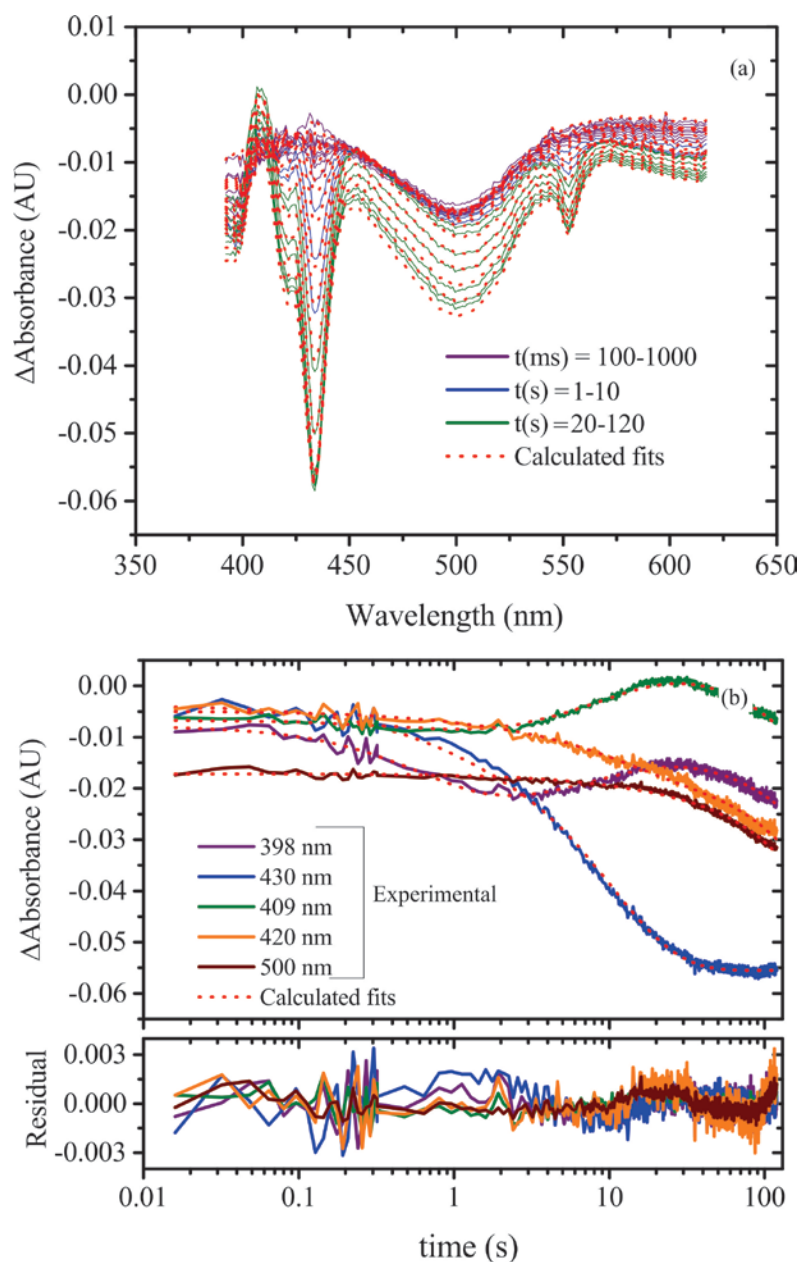


Figure 3.5. (a) Spectral changes at selected times observed when a solution initially containing 0.75 mM of the NO generating species **1**, 4 μM C_{554} and 3 μM MV_{red} was exposed to a 500 nm, 5 ns laser pulse which fragments **1** to release NO. The purple traces are at 100-ms intervals for the first 1000 ms, the blue traces are at one-second intervals, and the green traces are at 10-second intervals. The red traces are the least-squares best fits using Eq. 3.5. (b) Changes in absorbance vs time are plotted for 398 nm, 409 nm, 420 nm, 434 nm and 500 nm, where individual species make significant contributions; the red traces are from the least-squares best fits using Eq. 3.5.

powder (see Materials and Methods Section 3.2.3), was exposed to a 500 nm, 5 ns laser pulse, which fragments **1** to release NO (Scheme 3.1). Under these conditions all of the C₅₅₄ hemes (Fig. 1.4) are initially reduced. SVD analysis of the data showed that four components were needed to faithfully reconstruct a noise-reduced absorbance matrix. The SVD-treated data were fit to Eq. 3.5 using a global fitting routine.^{4, 5} In Eq. 3.5 spectral component Λ_0 is present

$$\Delta A_{\lambda,t} = \Lambda_{0(\lambda)} + \Lambda_{1(\lambda)}(1 - e^{-k_{1obs}t}) + \Lambda_{2(\lambda)}t + \Lambda_{3(\lambda)}(1 - e^{-k_{2obs}t}) \quad (3.5)$$

immediately after the laser pulse (taken as t_0), components Λ_1 and Λ_3 grow in exponentially in processes governed by the rate constants k_{1obs} and k_{2obs} , respectively, while component Λ_2 grows in linearly with time. As before with the 2-electron reduced case, the data were fit to Eq. 3.5 with a Mathcad program that allowed the two first-order rate constants to be manually adjusted, after which a pseudoinverse could be calculated to generate trial values of a matrix Λ that contained the spectral components.^{4, 5} The values of the rate constants were adjusted until the least-squares difference between the matrix of experimental absorbance values and the matrix of $\Delta A_{\lambda,t}$ values obtained from Eq. 3.5 was minimized.

Figure 3.6 shows the spectral components obtained from the fitting process. As with the 2-electron reduced case, the component Λ_0 (Fig. 3.6a) arises from the denitrosylation of species **1** within the deadtime of the experiment, and could be fit with the independently known extinction coefficient spectrum of species **1**. This revealed the amount of NO generated by the laser pulse to be 66 μM for the experiment portrayed. The component Λ_3 (Fig. 3.6d) that grows in exponentially could be fit (red trace) using the independently known extinction coefficient of the methyl viologen monocation radical (MV_{red}), and showed that 3.3 μM of this species was consumed upon exposure to NO; the rate constant k_{2obs} obtained for the process was 1.5 s^{-1} . The

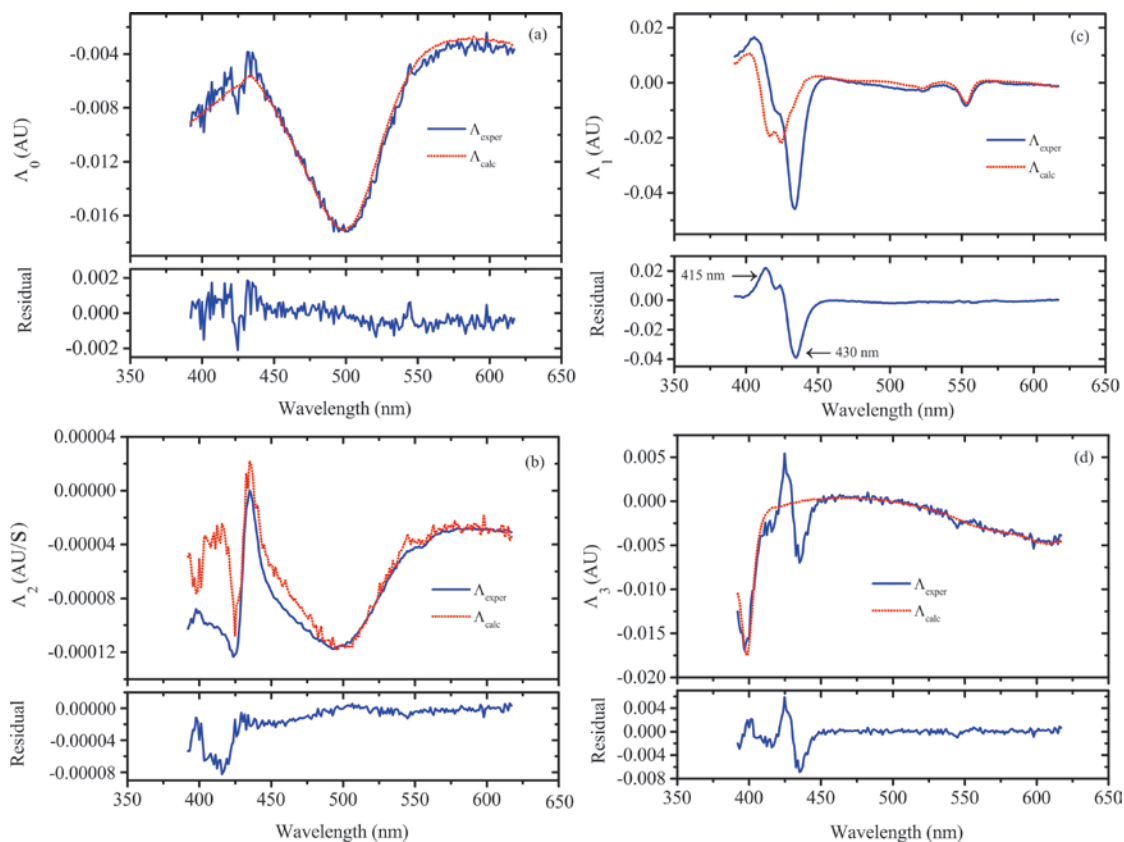


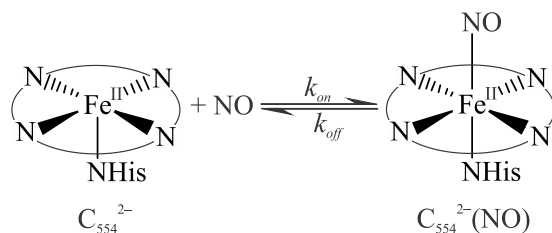
Figure 3.6. The spectral components Λ_0 - Λ_3 generated from the cleaned SVD absorbance matrix when fit to Eq. 3.5 (blue traces). The red traces in (a) and (b) were fit with the known extinction coefficient of species **1** and small admixtures of Λ_1 from Fig. 3.2b. The red trace in (d) was fit with the known extinction coefficient spectrum for MV_{red}. The red trace in (c) was fit with the difference spectrum $\Delta\epsilon_{LP}$ obtained in Section 2.3.1.

component Λ_2 (Fig 3.6b) that grows in linearly is once again attributed to the spectrophotometer probe-beam induced nitric oxide release from species **1**, and as before it can be fit primarily with the extinction coefficient spectrum for species **1**, with some admixture of component Λ_1 from the 2-electron reduced analysis of the previous section. The final component Λ_1 (Fig. 3.6c), which grows in exponentially with a k_{obs} of 0.097 s^{-1} , exhibits features characteristic of changes at the C₅₅₄ c hemes. In particular, the absorbance decreases at 554 nm and in the region 420 – 440 nm, and concomitant absorbance increase near 405 nm, at first sight appear to be diagnostic of

straightforward *c*-heme oxidation. However, more careful analysis revealed that more complex changes were occurring. The decrease at 554 nm is especially characteristic of low-spin heme oxidation (hemes I, III and IV). However, the largest net absorbance decrease occurs at 434 nm, which is diagnostic of changes at the single high-spin 5-coordinate heme II. Qualitative consideration of the relative magnitudes of high-spin and low-spin features suggested that component Λ_1 is a composite spectrum of all four hemes, and needs to be deconvoluted. To do this the contribution at 554 nm was subtracted out completely using the previously obtained (see Chapter 2) extinction coefficient difference spectrum $\Delta\epsilon_{LP}$ for the low potential hemes III and IV of C_{554} . In Fig. 3.6c the contribution from $\Delta\epsilon_{LP}$ that resulted in elimination of the 554 nm signal is shown by the dashed red line. The residual spectrum after the subtraction is shown in the bottom panel of Fig. 3.6c, and is comparable to the nitrosylated spectrum of two-electron reduced C_{554} (Fig. 3.2b). Thus, we conclude that the primary spectral change seen in Fig. 3.6c is due to nitrosylation of the high-spin heme II, just as it was when 2-electron reduced C_{554} was exposed to photogenerated NO. Some oxidation of the low-spin, low-potential *c* hemes occurred in tandem with the nitrosylation; however, quantitative analysis shows that this amounted to only $\sim 0.8 \mu\text{M}$ of the $4 \mu\text{M}$ available low-potential heme pool (which comprises hemes III and IV; see Section 2.3.1 and Appendix section A1.2). Assuming that the lowest-potential heme IV oxidizes first, this would amount to $\sim 40\%$ oxidation of heme IV, leaving hemes I, II and III fully reduced (with heme II of course also being nitrosylated). This is a very different result to that reported by Upadhyay et al., who saw rapid oxidation of all low-spin hemes upon exposure of fully reduced C_{554} to excess NO.²

3.4. Discussion

3.4.1. The reaction of photo-generated NO with two-electron reduced C₅₅₄. The results presented in Section 3.3.1 above are inconsistent with the results published earlier by Upadhyay et al.² that were summarized in Section 1.3. For 2-electron reduced C₅₅₄ the earlier work reported immediate oxidation of heme I upon addition of excess NO, though heme II



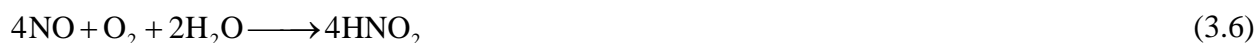
Scheme 3.2. Equilibrium between two-electron reduced C₅₅₄ and its nitrosylated form.

remained nitrosylated. We saw no evidence of heme I oxidation, which would have resulted in loss of signal at 420, 554 and 524 nm in the Fig. 3.1 difference spectra. This was true even in the presence of as much as 100 μM photogenerated NO (a 25 \times excess relative to the C₅₅₄ concentrations). The only changes observed in Fig. 3.1 and analogous spectra collected with other photogenerated NO concentrations was the absorbance decrease at 430 nm and concomitant increase at 414 nm, which could be attributed to high-spin ferrous heme I nitrosylation, as reported in the earlier paper.² The nitrosylation process is summarized in Scheme 3.2, in which the heme II center would be in the {Fe(NO)}⁷ state (Scheme 1.1).¹⁷

Our experiments were carried out in the presence of 200 μM $\text{Ru}(\text{NH}_3)_6^{2+}$, so we could not immediately rule out C₅₅₄-catalyzed reduction of NO to N₂O by the $\text{Ru}(\text{NH}_3)_6^{2+}$. Only about half of the Ru^{II} would potentially be oxidized by the highest concentrations of photogenerated NO

(~100 μM), and this would poise the solution at approximately -20 mV vs SHE (the midpoint potential for $\text{Ru}(\text{NH}_3)_6^{3+}$; Table 2.1). As the midpoint potential of C_{554} heme I is ~ 50 mV (Table 2.2), very little heme oxidation would be expected, even if all of the available NO was reduced to N_2O by $\text{Ru}(\text{NH}_3)_6^{2+}$. To test for this possibility, we used the thermally activated NO precursor DEANO (Section 3.2.1)^{6, 7, 12} to expose the $\text{C}_{554}/\text{Ru}(\text{NH}_3)_6^{2+}$ solutions to NO concentrations as high as 500 μM (data not shown). No C_{554} oxidation was observed at NO concentrations up to 300 μM . Such concentrations would have consumed all of the Ru^{II} , and subsequently all C_{554}^{2-} , if this species had been catalyzing NO reduction by $\text{Ru}(\text{NH}_3)_6^{2+}$. Hence, this possibility could be ruled out.

It should be noted that at NO concentrations higher than ~ 300 μM we did begin to see oxidation of both hemes I and II in the 2-electron reduced C_{554} , and this oxidation rate increased as the NO concentration was further increased (data not shown). Though such heme oxidation at very high NO concentrations could be due to direct interaction between NO and protein, the steep dependence on $[\text{NO}]$ instead suggests the involvement of residual oxygen. In aqueous solution NO and O_2 react to ultimately give NO_2^- , according to the stoichiometry shown in Eq. 3.6, but producing strongly oxidizing intermediates on the way.^{18, 19} The reaction is second order



in NO and first-order in O_2 , which gives it a very steep dependence on $[\text{NO}]$, much as we are seeing in the present case. In our experiments, we went to great lengths to exclude oxygen by using a glovebox, submitting all stock solutions to bulk electrolysis, and providing a high concentration of $\text{Ru}(\text{NH}_3)_6^{2+}$ that would tend to scrub out residual oxygen. Such precautions

may explain why we saw no C_{554}^{2-} oxidation at NO concentrations up to 300 μM , whereas Upadhyay et al. did.²

C_{554}^{2-} does nitrosylate at the heme II vacant site as reported earlier,² and our work now shows that this nitrosylation is discernibly reversible (Scheme 3.2, Section 3.3.1). Furthermore, by investigating the dependence of the nitrosylation rate k_{obs} on NO concentration, we were able to obtain the kinetic parameters k_{on} and k_{off} , as defined in Scheme 3.2, and the associated equilibrium constant $K_{eq} = k_{on}/k_{off}$ (Section 3.3.1). The K_{eq} value obtained from this analysis, $(9 \pm 2) \times 10^4 \text{ M}^{-1}$ (Section 3.3.1), is considerably lower than is typical for ferrous hemes; for example, the value for sperm whale myoglobin is estimated to be $\sim 10^{11} \text{ M}^{-1}$.^{12, 20} Indeed, the measured K_{eq} is more comparable to those obtained for ferric heme nitrosylations, which tend to be in the range $10^4 - 10^7 \text{ M}^{-1}$.^{12, 21, 22} A low binding constant is understandable given the steric crowding of the ostensibly vacant heme II site where the NO is binding (Fig. 1.5).

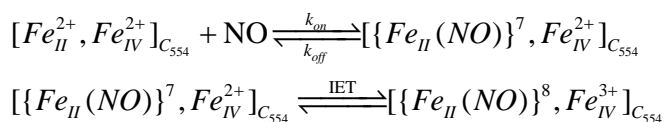
Horse heart ferrocyanochrome *c*, which will bind NO despite having no vacant heme sites available, displays a similarly low binding constant ($2.9 \times 10^5 \text{ M}^{-1}$).²¹ The comparison between the behavior towards NO of the two crowded hemes, that of the horse heart protein and heme II in C_{554} , is noteworthy. The k_{on} value for C_{554} is substantially higher than that for ferrocyanochrome *c* ($3000 \pm 140 \text{ M}^{-1}\text{s}^{-1}$ compared to $8.3 \text{ M}^{-1}\text{s}^{-1}$, a factor of 360 \times greater), but the difference in k_{off} values is even higher ($0.034 \pm 0.009 \text{ s}^{-1}$ compared to $2.9 \times 10^{-5} \text{ s}^{-1}$, a factor of 1200 \times greater).²¹ Unlike in the case of C_{554} , for NO to bind to ferrocyanochrome *c* the iron center must first dissociate a ligand, which likely explains the comparatively low k_{on} value. However, the much lower k_{off} value seen for ferrocyanochrome *c* indicates that, once bound, the Fe-NO bond is better stabilized in this protein than in C_{554} . Indeed, the NO k_{off} value for ferrocyanochrome *c* is

actually 10× smaller than that seen for ferromyoglobin ($2.9 \times 10^{-5} \text{ s}^{-1}$ vs. $1.2 \times 10^{-4} \text{ s}^{-1}$), though the far higher k_{on} for ferromyoglobin makes the net binding much tighter for the latter.²¹

Interestingly, NO will also bind to ferricytochrome *c*, with a K_{eq} value only slightly smaller than that seen for the ferrous heme (1.8×10^5 vs 2.9×10^5),²¹ whereas it will not bind at all to fully oxidized C₅₅₄.² This may reflect the fact that the Fe-NO bonds in ferric {Fe(NO)}⁶ species tend to be linear instead of bent as is typically the case for ferrous {Fe(NO)}⁷ species,²³ and a linear Fe-NO species would be much more hindered in the constrained pocket of C₅₅₄ (Fig. 1.5) than a bent one.

3.4.2. The reaction of photo-generated NO with four-electron reduced C₅₅₄. As mentioned earlier, one of the difficulties in studying reactions with NO under strongly reducing conditions is that this species reacts directly with many potential reducing agents, including the commonly used dithionite or methyl viologen monocation radical (MV_{red}). In the experiments presented in Section 3.3.2 solid Zn powder was used as the reducing agent. On its own this reagent was found to react very slowly with C₅₅₄ (over the course of a day; data not shown); however, in the presence of a small amount of methyl viologen as mediator, C₅₅₄ could be fully reduced in about half an hour. An advantage of our experimental setup, in which NO is photogenerated in less than a μs, is that it allowed us to deconvolute the reaction of residual MV_{red} with NO from that of C₅₅₄⁴⁻ with NO. Thus, from the Figs. 3.5 and 3.6d analyses, one can determine quantitatively that the concentration of the MV_{red} mediator was only about 3 μM, and that this was consumed within a few seconds by the photogenerated NO (with an observed first-order rate constant of 1.5 s^{-1}). In contrast C₅₅₄⁴⁻ nitrosylation and oxidation took tens of seconds, and was readily resolved from the MV_{red} reaction (Figs. 3.5 and 3.6c).

The results presented in Section 3.3.2 above are once again at odds with the results published earlier by Upadhyay et al.² that were summarized in Section 1.3. In the earlier work it was reported that the three low-spin hemes of C₅₅₄⁴⁻ are fully and rapidly oxidized upon exposure to excess NO, with a single turnover rate exceeding 16 s⁻¹.² In our case we observed that exposure of 4 μM C₅₅₄⁴⁻ to 66 μM of photogenerated NO resulted in oxidation of only about 40% of the available low-potential heme IV, leaving the remaining hemes reduced. Furthermore, heme IV oxidation was concomitant with heme II nitrosylation, and proceeded with an observed rate constant k_{obs} of 0.097 s⁻¹. This rate constant is comparable to those observed for heme II nitrosylation in 2-electron reduced C₅₅₄, and considerably below 16 s⁻¹.



Scheme 3.3. One proposed mechanism for the reaction of NO with fully reduced C₅₅₄. IET, intramolecular electron transfer.

Scheme 3.3 suggests one possible explanation for the partial oxidation of heme IV that accompanies heme II nitrosylation (Figs. 3.5 and 3.6c). According to this mechanism, the {Fe(NO)}⁷ species generated by nitrosylation of heme II is reversibly reduced to {Fe(NO)}⁸ by intramolecular electron transfer (IET) from the low potential heme IV. In this scenario, the nitrosylation would be rate-limiting, and occur at roughly the same rate as it does for C₅₅₄²⁻ (Scheme 3.2), after which the IET equilibrium would be established rapidly. If the Scheme 3.3 mechanism is assumed to be correct, it can be used to extract the midpoint potential for {Fe(NO)}⁷ reduction from Fig. 3.6c (Appendix 2). As explained above, fitting Fig. 3.6c with the C₅₅₄ low-potential extinction coefficient difference spectrum obtained in Chapter 2 allows one to

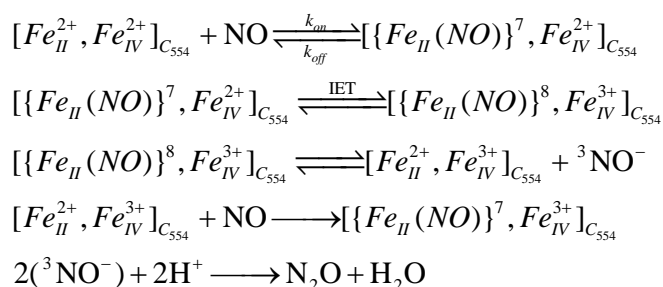
estimate that heme II nitrosylation of C_{554}^{2-} is accompanied by ~40% oxidation of heme IV. According to Scheme 3.3 this would correspond to an equilibrium constant of ~0.67 governing IET from ferrous heme IV to $\{Fe(NO)\}^7$ heme II, which in turn would translate to a cell potential of -0.0102 V for net reduction of $\{Fe(NO)\}^7$ heme II by ferrous heme IV. Given that the midpoint potential for heme IV is -0.25 V (Table 2.2), we find that the midpoint potential for $\{Fe(NO)\}^7$ heme II reduction would be ~ -0.260 V according to the Scheme 3.3 mechanism (Appendix 2).

Scheme 3.3 is a minimalist mechanism, which invokes no further reactivity for the bound NO. Though its simplicity is attractive, it requires the implicit assumption that the heme II $\{Fe(NO)\}^7$ and $\{Fe(NO)\}^8$ moieties have virtually identical extinction coefficient difference spectra, since the residual spectrum of Fig. 3.6c after the heme oxidation contribution is subtracted looks essentially the same as the $\{Fe(NO)\}^7$ spectrum observed upon nitrosylation of C_{554}^{2-} heme II (Fig. 3.2b). This is not impossible; to our knowledge pure $\{Fe(NO)\}^8$ heme species have not been previously reported for proteins, but the protonated $\{Fe(HNO)\}^8$ species has been characterized for myoglobin, and its UV/Vis spectrum is similar to that of myoglobin $\{Fe(NO)\}^7$.²⁴ Nevertheless, an alternative mechanism is proposed in Scheme 3.4, which would result in heme II ending up as $\{Fe(NO)\}^7$. The first two steps of this mechanism are the same as for Scheme 3.3, but in this case $\{Fe_{II}(NO)\}^8$ is proposed to release nitroxyl (NO^-), which is known to dimerize rapidly in aqueous solution to generate N_2O .^{1, 24, 25} Release of NO^- from $\{Fe_{II}(NO)\}^8$ would leave heme II in the ferrous state, and this species could then react with a second equivalent of NO. The final heme II product would thus be $\{Fe(NO)\}^7$, just as it was after nitrosylation of C_{554}^{2-} . Further oxidation of the C_{554} heme pool would be prevented if neither hemes I or III were strong enough reducing agents to once again reduce $\{Fe_{II}(NO)\}^7$ to

$\{Fe_{II}(NO)\}^8$. This is supported by the $\{Fe_{II}(NO)\}^7$ midpoint potential estimate of -0.21 V obtained above for Scheme 3.3 mechanism; the heme III midpoint potential of -0.150 V (Table 2.2) would yield an unfavorable cell potential of -0.11 V for reduction of $\{Fe_{II}(NO)\}^7$ by ferrous heme III, and an even more unfavorable potential for reduction by ferrous heme I.

3.5. Summary

Our results indicate that C_{554}^{2-} and C_{554}^{4-} will both nitrosylate at heme II; however, we saw no evidence of the previously reported C_{554} -catalyzed NO reduction,² either with C_{554}^{2-} or



Scheme 3.4. An alternative mechanism for the reaction of NO with fully reduced C_{554} , which allows for sub-stoichiometric production of N_2O . Note that free nitroxyl anion is expected to be in the triplet state.¹

with C_{554}^{4-} . Some sub-stoichiometric oxidation of the lowest potential heme IV is detected when C_{554}^{4-} is exposed to an excess of photogenerated NO, and Scheme 3.4 shows how this could be leading to formation of small amounts of N_2O . In principle such reactivity could be exploited to yield a catalytic system, if a reducing agent potent enough to re-reduce heme IV were provided; however, our results show that in such a system heme II nitrosylation would likely be rate limiting with a rate constant in the range of ~ 0.1 s⁻¹. Since NO typically reacts directly with strong reducing agents at much faster rates (see for example above for $NO + MV_{red}$), it is

difficult to see how a catalytic system would be devised in practice. Finally, one should remember that Scheme 3.4 is proposed on the basis of the observed heme spectral changes, without any evidence that N₂O is in fact being generated. The original report of C₅₅₄ NO reductase activity was similarly based on the observed heme spectral changes, and provided no direct measurements of N₂O generation. Whether N₂O is in fact produced, even in the sub-stoichiometric amounts proposed here, will have to be tested for in future studies.

3.6. References

- [1] Shafirovich, V., and Lymar, S. V. (2002) Nitroxyl and its anion in aqueous solutions: spin states, protic equilibria, and reactivities toward oxygen and nitric oxide, *PNAS* 99, 7340-7345.
- [2] Upadhyay, A. K., Hooper, A. B., and Hendrich, M. P. (2006) NO reductase activity of the tetraheme cytochrome c(554) of *Nitrosomonas europaea*, *J. Am. Chem. Soc.* 128, 4330-4337.
- [3] Eroy-Reveles, A., Leung, Y., Beavers, C. M., Olmstead, M. M., and Mascharak, P. K. (2008) Near-Infrared Light Activated Release of Nitric Oxide from Designed Photoactive Manganese Nitrosyls: Strategy, Design, and Potential as NO Donors, *J. Am. Chem. Soc.* 130, 4447-4458.
- [4] Koebke, K. J., Pauly, D. J., Lerner, L., Liu, X., and Pacheco, A. A. (2013) Does the oxidation of nitric oxide by oxyMyoglobin share an intermediate with the metMyoglobin-catalyzed isomerization of peroxynitrite?, *Inorg. Chem.* 52, 7623-7632.
- [5] Koebke, K. J., Waletzko, M. T., and Pacheco, A. A. (2016) Direct monitoring of the reaction between photochemically generated nitric oxide and *Mycobacterium tuberculosis*

- truncated hemoglobin N wild type and variant forms: an assessment of theoretical mechanistic predictions., *Biochemistry* 55, 686-696.
- [6] Drago, R. S., and Paulik, F. E. (1960) The Reaction of Nitrogen (II) Oxide with Diethylamine, *J. Am. Chem. Soc.* 82, 96-98.
- [7] Maragos, C. M., Morley, D., Wink, D. A., Dunams, T. M., Saavedra, J. E., Hoffman, A., Bove, A. A., Isaac, L., Hrabie, J. A., and Keefer, L. K. (1991) Complexes of NO with Nucleophiles as Agents for the Controlled Biological Release of Nitric-Oxide - Vasorelaxant Effects, *J. Med. Chem.* 34, 3242-3247.
- [8] Koebke, K. J. (2015) Mechanistic study of heme protein-mediated nitric oxide dioxygenation using photolytically produced nitric oxide In *Department of Chemistry and Biochemistry*, University of Wisconsin-Milwaukee.
- [9] Cabail, M. Z., Moua, V., Bae, E., Meyer, A., and Pacheco, A. A. (2007) Quantifying the photoinduced release of nitric oxide from N,N'-bis(carboxymethyl)-N,N'-dinitroso-1,4-phenylenediamine. Effect of reducing agents on the mechanism of the photoinduced reactions, *J. Phys. Chem. A* 111, 1207-1213.
- [10] Kostera, J., Youngblut, M. D., Slosarczyk, J. M., and Pacheco, A. A. (2008) Kinetic and product distribution analysis of NO reductase activity in *Nitrosomonas europaea* hydroxylamine oxidoreductase, *J. Biol. Inorg. Chem.* 13, 1073-1083.
- [11] Kostera, J., McGarry, J. M., and Pacheco, A. A. (2010) Enzymatic Interconversion of Ammonia and Nitrite: the Right Tool for the Job, *Biochemistry* 49, 8546-8553.
- [12] Purwar, N., McGarry, J. M., Kostera, J., Pacheco, A. A., and Schmidt, M. (2011) Interaction of nitric oxide with catalase: structural and kinetic analysis, *Biochemistry* 50, 4491-4503.

- [13] Youngblut, M., Judd, E. T., Srajer, V., Sayyed, B., Goelzer, T., Elliott, S. J., Schmidt, M., and Pacheco, A. A. (2012) Laue crystal structure of *Shewanella oneidensis* cytochrome *c* nitrite reductase from a high-yield expression system, *J. Biol. Inorg. Chem.* *17*, 647-662.
- [14] Youngblut, M., Pauly, D. J., Stein, N., Walters, D., Conrad, J. A., Moran, G. R., Bennett, B., and Pacheco, A. A. (2014) *Shewanella oneidensis* cytochrome *c* nitrite reductase (ccNiR) does not disproportionate hydroxylamine to ammonia and nitrite, despite a strongly favorable driving force., *Biochemistry* *53*, 2136-2144.
- [15] Press, W. H., Teukolsky, S. A., Vetterling, W. T., and Flannery, B. P. (2007) Numerical Recipes the art of scientific computing, 3rd ed., pp 65-75, Cambridge University Press, New York, NY.
- [16] Henry, E. R., and Hofrichter, J. (1992) Singular Value Decomposition: Application to Analysis of Experimental Data, In *Meth. Enzymol.* (Brand, L., and Johnson, M. L., Eds.), pp 129-192, Academic Press, San Diego.
- [17] Enemark, J. H., and Feltham, R. D. (1974) Principles of Structure, Bonding and Reactivity for Metal Nitrosyl Complexes, *Coord. Chem. Rev.* *13*, 339-406.
- [18] Goldstein, S., and Czapski, G. (1995) Kinetics of nitric oxide autoxidation in aqueous solution in the absence and presence of various reductants. The nature of the oxidizing intermediates, *J. Am. Chem. Soc.* *117*, 12078-12084.
- [19] Goldstein, S., and Czapski, G. (1996) Mechanism of the nitrosation of thiols and amines by oxygenated NO solutions: the nature of the nitrosating intermediates, *J. Am. Chem. Soc.* *118*, 3419-3425.

- [20] Hoshino, M., Maeda, M., Konishi, R., Seki, H., and Ford, P. C. (1996) Studies on the reaction mechanism for reductive nitrosylation of ferrihemoproteins in buffer solutions, *J. Am. Chem. Soc.* *118*, 5702-5707.
- [21] Hoshino, M., Ozawa, K., Seki, H., and Ford, P. C. (1993) Photochemistry of Nitric-Oxide Adducts of Water-Soluble Iron(III) Porphyrin and Ferrihemoproteins Studied by Nanosecond Laser Photolysis, *J. Am. Chem. Soc.* *115*, 9568-9575.
- [22] Laverman, L. E., Wanat, A., Oszejca, J., Stochel, G., Ford, P. C., and van Eldik, R. (2001) Mechanistic studies on the reversible binding of nitric oxide to metmyoglobin, *J. Am. Chem. Soc.* *123*, 285-293.
- [23] Ford, P. C., and Lorkovic, I. M. (2002) Mechanistic aspects of the reactions of nitric oxide with transition-metal complexes, *Chem. Rev.* *102*, 993-1017.
- [24] Lin, R., and Farmer, P. J. (2000) The HNO adduct of myoglobin: synthesis and characterization, *J. Am. Chem. Soc.* *122*, 2393-2394.
- [25] Shafirovich, V., and Lyman, S. V. (2003) Spin-forbidden deprotonation of aqueous nitroxyl (HNO), *J. Am. Chem. Soc.* *125*, 6547-6552.

Chapter 4

The reaction of the cytochrome *c*₅₅₄ mutant F156A, at various stages of reduction, with photo-generated nitric oxide

4.1. Introduction

The results from Chapter 3 showed that 2-electron reduced C₅₅₄ will bind NO but not reduce it, while the 4-electron reduced protein will partially reduce bound NO by transferring an electron from its lowest potential heme. This is intriguing because ongoing studies by the Pacheco group are showing that many non-specialized proteins, such as HAO, are capable of reducing NO to ammonia in the presence of sufficiently powerful reducing agents.^{1, 2} Two possible explanations for why reduced C₅₅₄ will not reduce bound NO are that the NO binding pocket at heme II is very crowded, or that the pocket is very hydrophobic, and devoid of hydrogen bonding amino acids capable of acting as proton donors. This chapter explores what happens when the bulky amino acid Phe 156 is replaced by an alanine, thus opening up more space in the vicinity of the heme II vacant site. Chapter 5 reports on the consequences of replacing Phe 156 with a nearly equally bulky, but protonatable, histidine.

4.2. Materials and Methods

4.2.1. General materials. The provenance of most of the common chemicals used in this chapter's experiments was summarized in Chapter 3. Methods for preparing the complex K[Ru(EDTA)Cl]·2H₂O and its precursors were found in articles by Wanat et al,³ Chatterjee et al,⁴ and references therein.

4.2.2. General instrumentation. The instrumentation available for routine measurements was previously described in Chapter 3.

4.2.3. Protein handling. The construction of the F156A expression system, as well as the purification protocol for the mutant, were described in Chapter 2. Solutions of F156A for experiments in which the protein was exposed to NO photogenerated from **1** by laser photolysis were prepared and handled as described in Chapter 3.

Stock NO for stopped-flow experiments was prepared from the precursor DEANO (Chapter 3)⁵⁻⁷ in a two-step process. In the first step a concentrated (20 mM) solution of DEANO was prepared in 0.01 M NaOH (pH 12), where it is stable for extended periods. When needed the DEANO was diluted to 200 μ M with the standard pH 7.0 HEPES buffer and allowed to stand for 15 minutes, during which time it decomposed to yield two equivalents of NO.^{5,6} In preparation for the stopped-flow experiments the F156A was 2-electron reduced in the glovebox by bulk electrolysis, in solutions containing 200 μ M Ru(NH₃)₆³⁺ in 1 M NaCl in addition to the standard HEPES buffer, as described in Chapter 3. The two-electron reduced F156A was then nitrosylated by adding enough pH 7.0 DEANO stock to give 50 μ M of NO in the reaction mixture. The final solution contained 1.5 μ M nitrosylated two-electron reduced F156A, and was housed in a tonometer for anaerobic transport to the stopped flow system. All other anaerobic solutions used in stopped-flow experiments were prepared by purging with nitrogen streams. Experiments involving wild type C₅₅₄ were prepared following the same procedure, using 2.1 μ M of nitrosylated two-electron reduced C₅₅₄ in the tonometer.

Concentrations of F156A in the reaction mixtures used for laser spectroscopy and stopped-flow experiments, as well as the extent of the protein's reduction, were assessed by

UV/Vis spectroscopy using the extinction coefficient spectra of F156A at various stages of reduction, obtained independently by spectropotentiometry, as described in Chapter 2.

4.2.4. Laser-initiated time-resolved spectroscopic experiments. The instrumentation used for laser-initiated time resolved spectroscopic laser experiments was as described in Chapter 3. Over timescales of seconds to tens of seconds, UV/vis spectra following the laser pulse were collected with the OLIS RSM 1000 spectrophotometer in rapid-scanning mode 1, which allowed complete spectra in the range from 387 nm – 612 nm to be collected at a rate of 62 scans/sec. The very fast nitrosylation of F156A was monitored with the OLIS RSM 1000 single wavelength mode.

4.2.5. Denitrosylation stopped-flow experiments. Stopped-flow experiments were done on a SF-61 DX2 stopped-flow system (Hi Tech Scientific), which was made anaerobic by scrubbing the system overnight with a solution containing 2 U/ml glucose oxidase (MP biomedical) and 1 mM glucose (Fisher Scientific). The apparatus was used in single-mixing mode, with one drive syringe containing the 2-electron nitrosylated C₅₅₄ or F156A described above, and the other containing a 200 μM anaerobic solution of [Ru(EDTA)OH₂]⁻ in the standard HEPES buffer. The protein solution was rapidly mixed with the [Ru(EDTA)OH₂]⁻, and spectral changes were monitored at 430 nm using photomultiplier tubes (Hi Tech Scientific) for 300 seconds for C₅₅₄, and 160 seconds for F156A.

4.2.6. Data analysis. All data were analyzed using programs written within the commercially available software packages Origin version 6.0 or later (Microcal Software), or Mathcad 13 or later (PTC Software). The analysis strategies used in our laboratories have been previously described in general terms in references 1,2,7-9. Strategies more specific to analyzing

kinetic data, including the background for the equations appearing in the Results and Discussion below, can be found in references 10-12.

4.3. Results

4.3.1. The reaction of photo-generated NO with two-electron reduced F156A. Figure 4.1 shows the spectral change observed immediately after a solution initially containing 900 μM of the NO generating species **1**, 5 μM F156A and 200 μM $\text{Ru}(\text{NH}_3)_6^{2+}$ was exposed to a 500 nm, 5 ns laser pulse, which fragments **1** to release NO (Scheme 3.1). Under these conditions the hemes of F156A with the highest potential (hemes I and II, Fig. 1.4) are reduced, while the lower potential hemes (hemes III and IV, Fig 1.4) remain oxidized (Table 2.2). The Fig. 4.1 spectrum shows absorbance decreases centered around 432nm and 500 nm, and an absorbance increase

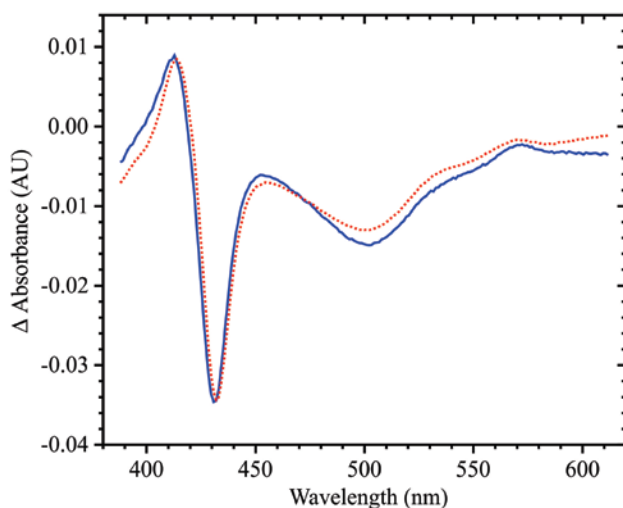


Figure 4.1. Blue trace: Spectral change observed immediately (within 16 ms) after a solution initially containing approximately 900 μM of the NO generating species **1**, 5 μM F156A and 200 μM $\text{Ru}(\text{NH}_3)_6^{2+}$ was exposed to a 500 nm, 5 ns laser pulse, which fragments **1** to release NO. Red trace: least-squares best fit using the independently known extinction coefficient spectrum of **1** and the extinction coefficient difference spectrum for wild type C_{554}^{2-} nitrosylation obtained as described in Chapter 3. From the fit one can estimate that the laser pulse photogenerated about 48 μM NO.

centered around 413 nm. Least-squares fitting of this spectrum with the independently known extinction coefficient spectrum of **1**, and the extinction coefficient difference spectrum for wild type C₅₅₄²⁻ nitrosylation obtained as described in Chapter 3, gave a reasonably good fit (red trace, Fig. 4.1). This shows that 2-electron reduced F156A nitrosylates much faster than wild type, within milliseconds instead of tens of seconds (Section 3.3.1). Further minor spectral changes were seen in the minutes following the laser pulse (data not shown). These could be attributed to additional photolysis of **1** in the spectrophotometer probe beam, and associated C₅₅₄²⁻ nitrosylation. No evidence was seen in this experiment for F156A²⁻ oxidation.

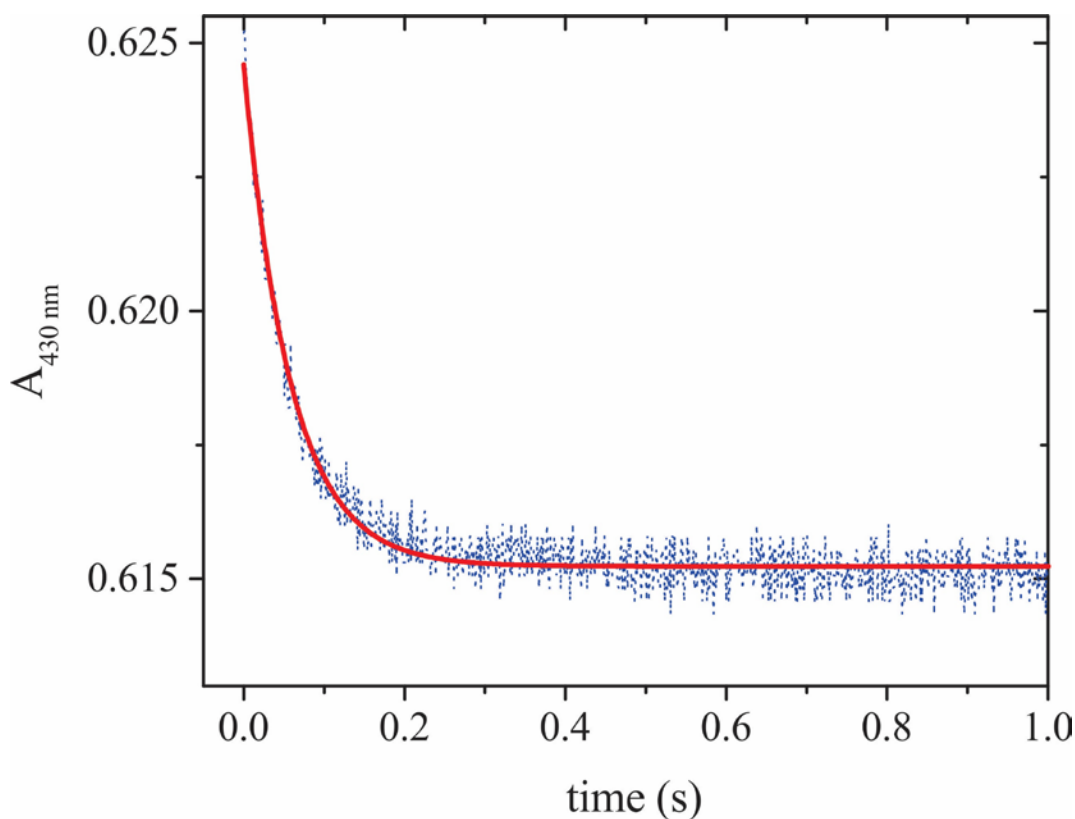


Figure 4.2. Change in absorbance at 430 nm over 1 s observed after a solution initially containing 12 μM F156A, 200 μM $\text{Ru}(\text{NH}_3)_6^{2+}$ and 48 μM of the NO generating species **1** was irradiated with a 500 nm, 5 ns laser pulse. Red trace: least-squared best fit to an exponential function.

F156A²⁻ nitrosylation proved too fast to follow reliably with the spectrophotometer in rapid scanning mode, so quantitative kinetic measurements were made with the instrument in fixed-wavelength mode. Figure 4.2 shows the change in absorbance at 430 nm over 1 s after a solution initially containing 12 μM F156A, 200 μM Ru(NH₃)₆²⁺ and 48 μM of the NO generating species **1** was irradiated with a 500 nm, 5 ns laser pulse. The data were well fit with a single exponential function (red trace, Fig. 4.2). The analysis described for Figure 4.2 was repeated with solutions containing varying concentrations of two-electron reduced F156A and a constant concentration of species **1**. The values of the rate constant k_{obs} obtained from the exponential fits varied linearly with concentration of F156A²⁻, as seen in Fig. 4.3.

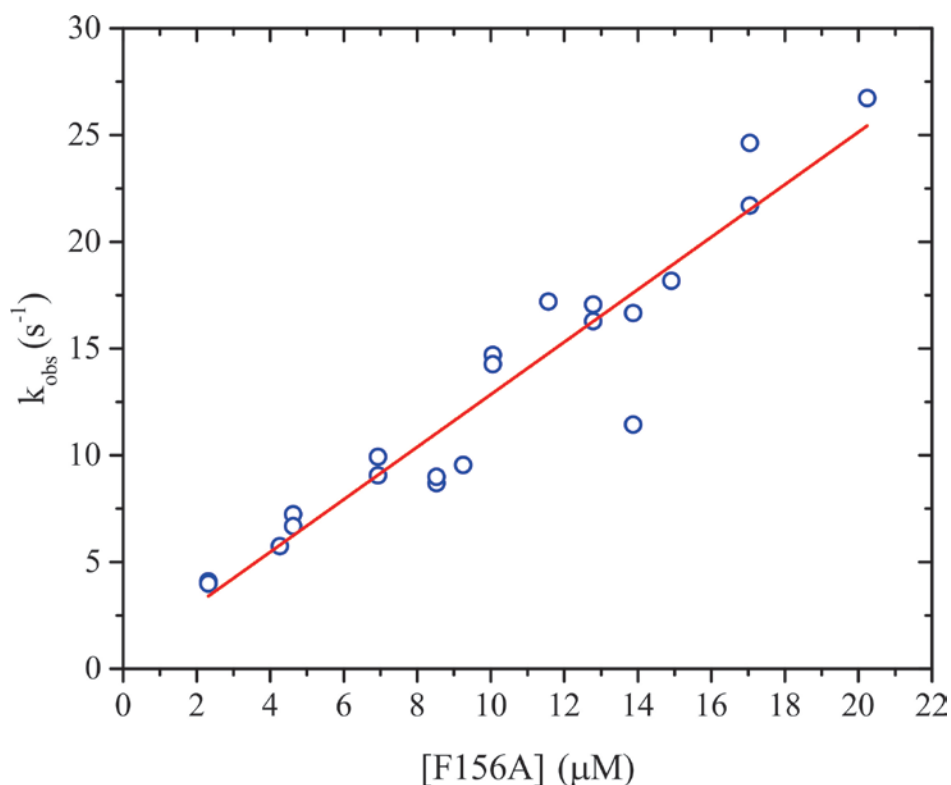
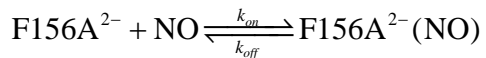


Figure 4.3. Blue circles: plot of k_{obs} associated with the exponential absorbance decrease at 430 nm vs F156A²⁻ concentration. Red trace: least-squares fit of the data to a straight line (Eq. 4.1). Slope = $(1.23 \pm 0.09) \times 10^6 \text{ M}^{-1} \text{ s}^{-1}$; Intercept = $0.5 \pm 1 \text{ s}^{-1}$. Note that the intercept is zero within the precision of the measurement.

Presumably, by analogy with the wild type case, F156A²⁻ nitrosylation is reversible as shown in Scheme 4.1, so that k_{obs} should vary linearly with [NO] as shown in Eq. 4.1. However,



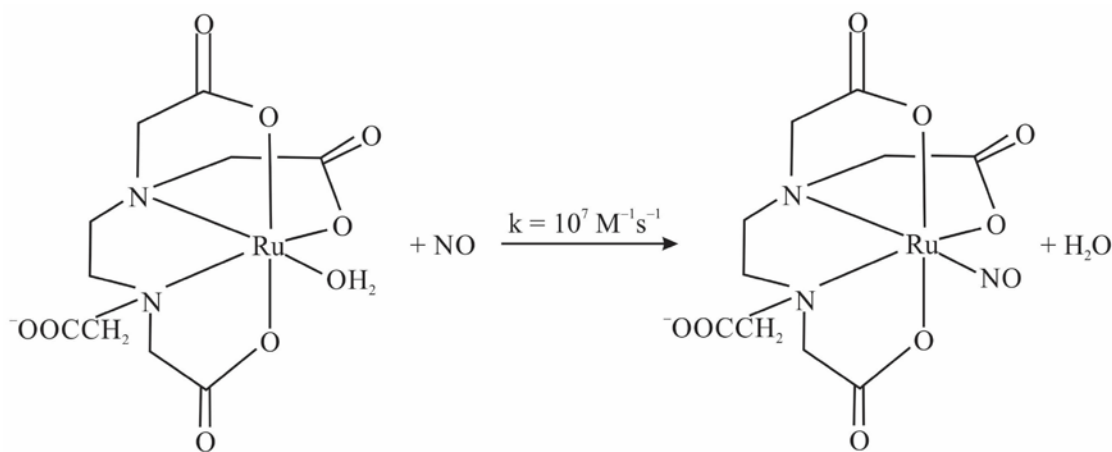
Scheme 4.1.

the intercept in Fig. 4.3 is zero within the precision of the measurements, so k_{off} can't be obtained

$$k_{obs} = k_{off} + k_{on}[\text{F156A}] \quad (4.1)$$

from this method. From the slope of the Fig. 4.3 line, k_{on} was estimated to be $(1.23 \pm 0.09) \times 10^6 \text{ M}^{-1}\text{s}^{-1}$, which is about 400× higher than the k_{on} value obtained for the wild type (Fig. 3.3).

4.3.2. Stopped-flow investigation of C554²⁻(NO) and F156A²⁻(NO) denitrosylation. As the k_{off} value could not be obtained from the Fig. 4.3 results, an alternative strategy was developed to measure this parameter directly, using a well-known NO trapping method.^{3, 4, 13} In this method, NO released from a labile nitrosylated protein of interest is rapidly and irreversibly trapped by $[\text{Ru}(\text{EDTA})\text{OH}_2]^-$, as shown in Scheme 4.2. Assuming that dissociation of NO from



Scheme 4.2.

the protein of interest is rate limiting, the method is readily used to measure the dissociation rate constant. The method was first tested with wild type C_{554} , for which the dissociation rate constant had been previously determined (Chapter 3); the denitrosylation was monitored by UV/Vis stopped-flow spectroscopy. C_{554}^{2-} was first fully nitrosylated by adding an excess of NO, obtained from decomposition of the precursor DEANO,⁵⁻⁷ as described in Section 4.2.3.

Figure 4.4a shows the change in absorbance at 430 nm observed after a solution initially containing 2.1 μM wild type $C_{554}^{2-}(\text{NO})$ and about 50 μM free NO was mixed by stopped-flow with a second solution containing 200 μM of the NO trapping compound $[\text{Ru}(\text{EDTA})\text{OH}_2]^-$. The data were fit using a two-exponential function (red trace Fig. 4.4a), which gave rate constant values of $0.0178 \pm 0.0001 \text{ s}^{-1}$ and a $0.090 \pm 0.004 \text{ s}^{-1}$. The amplitude associated with the first rate constant is 4 \times that of the second, and that rate constant value matches the k_{off} value obtained in the Chapter 3 experiments ($0.034 \pm 0.009 \text{ s}^{-1}$, Fig. 3.3) fairly closely. The minor exponential component is believed to arise from heme oxidation, either directly or indirectly by residual oxygen. This will have to be confirmed in future experiments where spectral changes are monitored at more than one wavelength; however, in support of the conjecture, the UV/Vis spectrum taken after stopped-flow mixing did show that some heme oxidation had accompanied denitrosylation.

The stopped flow experiment was repeated using F156A in place of C_{554} to determine the k_{off} for $\text{F156A}^{2-}(\text{NO})$ denitrosylation (Scheme 4.1). The blue trace in Fig. 4.4b shows the corresponding change in absorbance at 430 nm when 1.5 μM of $\text{F156A}^{2-}(\text{NO})$ (pre-nitrosylated with 50 μM NO as described in the Section 4.2.3) was rapidly mixed with 200 μM of $[\text{Ru}(\text{EDTA})\text{OH}_2]^-$. As before, the data were fit using a two-exponential decay equation (red

trace Fig 4.4b), which in this case gave rate constant values of 0.021 s^{-1} and 0.070 s^{-1} . Once again, inspection of the spectrum obtained after stopped-flow mixing showed that some heme oxidation had accompanied denitrosylation. In this case the amplitudes associated with the two rate constants were very similar (the higher-valued one had an amplitude about $1.4\times$ larger than the lower-valued one), which makes it difficult to be sure of which rate constant is associated with denitrosylation and which is tied to oxidation. However, given that the two rate constants are within a factor of 4 of each other, the salient fact is that the k_{off} values for $C_{554}^{2-}(\text{NO})$ and

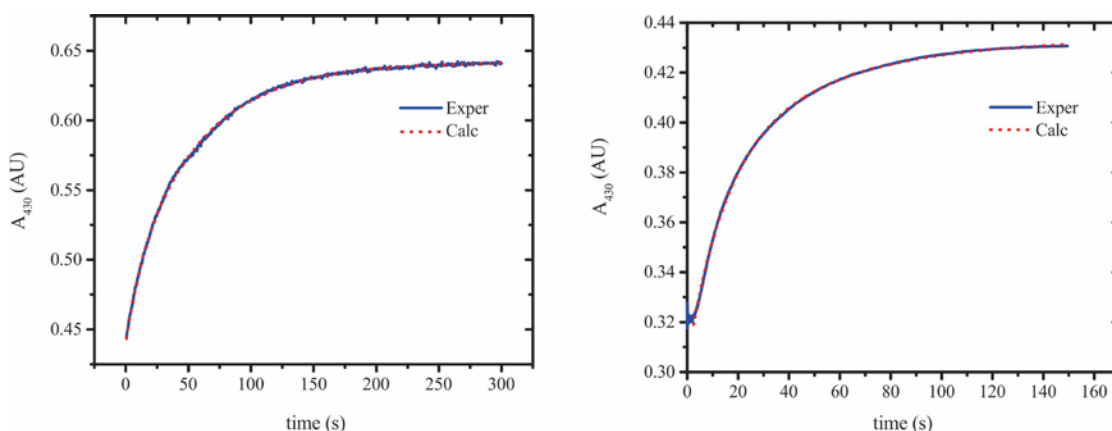


Figure 4.4. (a) Blue trace: change in absorbance at 430 nm observed after a solution initially containing $2.1\ \mu\text{M}$ wild type $C_{554}^{2-}(\text{NO})$ was mixed by stopped-flow with a second solution containing $200\ \mu\text{M}$ of the NO trapping compound $[\text{Ru}(\text{EDTA})\text{OH}_2]^-$. Red trace: least-squares fit of the data with a two-exponential function. (b) Similar to (a), but syringe 1 contained $1.5\ \mu\text{M}$ nitrosylated F156A instead of wild type protein. In both cases the concentration of $[\text{Ru}(\text{EDTA})\text{OH}_2]^-$ was sufficient to remove free NO as well as NO being released from nitrosylated protein.

$\text{F156A}^{2-}(\text{NO})$ must be in the same ballpark, whereas the k_{on} value for NO binding to F156A^{2-} is $400\times$ higher than the k_{on} value obtained for the wild type. Using the two rate constants obtained from the Fig. 4.4b fits, one can estimate the equilibrium constant $K_{eq} = k_{on}/k_{off}$ for F156A^{2-} nitrosylation to be about $(4\pm 2)\times 10^7\text{ M}^{-1}$. This represents an NO affinity about $440\times$ stronger for

the F156A²⁻ mutant compared to the wild type C₅₅₄²⁻, which is almost entirely due to the higher k_{on} value for the former.

4.3.3. The reaction of photo-generated NO with four-electron reduced F156A.

Figure 4.5 shows the spectral changes observed after a solution initially containing 7 μ M F156A, 570 μ M of species **1**, and 3 μ M of methyl viologen reduced by zinc powder (see Section 3.2.3), was exposed to a 500 nm, 5 ns laser pulse, which fragments **1** to release NO (Scheme 3.1).

Under these conditions all of the F156A hemes are initially reduced. SVD analysis of the data showed that three components were needed to faithfully reconstruct a noise-reduced absorbance matrix. The SVD-treated data were fit to Eq. 4.3, which has the same form as Eq. 3.1, using a global fitting routine. As before with the wild type two-electron case (Chapter 3) the data were

$$\Delta A_{\lambda,t} = \Lambda_{0(\lambda)} + \Lambda_{1(\lambda)}(1 - e^{-k_{obs}t}) + \Lambda_{2(\lambda)}t \quad (4.3)$$

fit to Eq. 4.3 with a Mathcad program that allowed the first order rate constant to be manually adjusted, after which a pseudoinverse could be calculated to generate trial values of a matrix Λ that contained the spectral components.^{10, 12} The value of the rate constant was adjusted until the least-squares difference between the matrix of experimental absorbance values and the matrix of $\Delta A_{\lambda,t}$ values obtained from Eq. 4.3 was minimized.

Figure 4.6 shows the spectral components obtained from the fitting process. As with the wild type two-electron reduced case, a major contributor to the component Λ_0 (Fig. 4.6a) comes from the denitrosylation of species **1** within the deadtime of the experiment; however, now the component also has a contribution from F156A⁴⁻ nitrosylation, which is taking place on the ms timescale, as previously seen for the 2-electron reduced protein (Section 4.3.1). The component is well fit using the independently known extinction coefficient spectrum of **1**, and the extinction

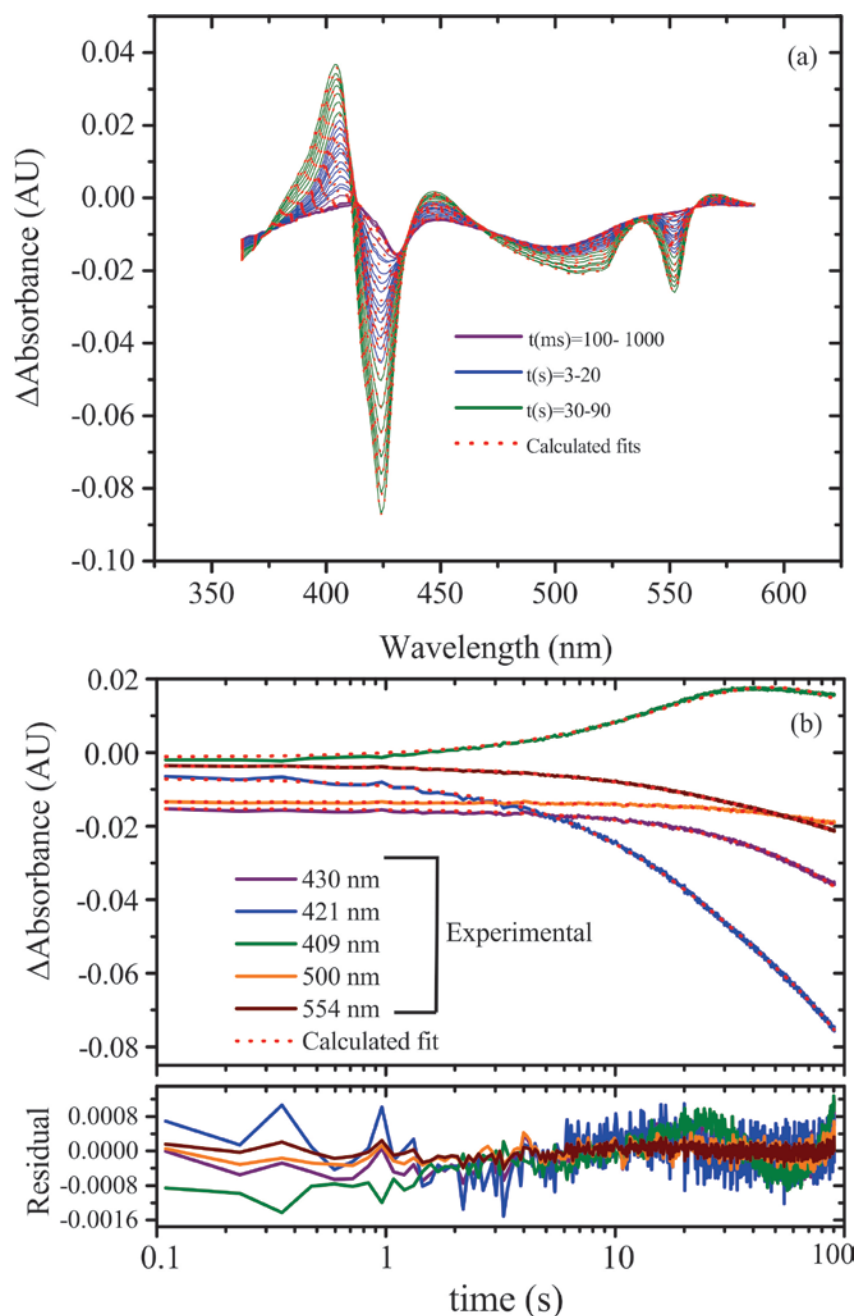


Figure 4.5. (a) Spectral changes at selected times observed when a solution initially containing 0.57 mM of the NO generating species **1**, 7 μM F156A and 3 μM MV_{red} was exposed to a 500 nm, 5 ns laser pulse which fragments **1** to release NO. The purple traces are representative of the first second, the blue traces are taken at 1-s intervals, and the green ones at 10-s intervals. The red traces are the least-squares best fits using Eq. 4.3. (b) Changes in absorbance vs time at the representative wavelengths stated, with the least-squares best fits using Eq. 4.3 overlaid as red traces.

coefficient difference spectrum of F156A²⁻(NO), obtained by analyzing nitrosylation of the 2-electron reduced protein (red trace, Fig. 4.6a).

Unlike in cases encountered earlier in this work, the major contributions to the linearly increasing component Λ_2 (Fig. 4.6c) are no longer from photolysis of **1** in the spectrometer probe beam. Instead, the major changes are now clearly due to *c*-heme oxidation; the absorbance decreases at 526 and 554 are particularly diagnostic of low-spin *c*-heme oxidation in general, and the decreases at 416 and 426 are reminiscent of the split-Soret spectral changes seen when hemes III and IV were electrochemically reduced in the Chapter 2 experiments. With this in mind, the Λ_2 component was reasonably well fit using the $\Delta\epsilon_3$ and $\Delta\epsilon_4$ extinction coefficient difference spectra obtained for the low potential hemes III and IV of F156A by UV/Vis spectropotentiometry (Section 2.3.2), as well as the extinction coefficient difference spectrum of F156A²⁻(NO) obtained by analyzing nitrosylation of the 2-electron reduced protein, and the extinction coefficient spectrum of **1**. The least-squares best fit is shown as a red overlay on Fig. 4.3.

The final component Λ_1 (Fig. 4.6b), which grows in exponentially with a k_{obs} of 0.05 s⁻¹, also exhibits features characteristic of low-spin *c*-ferroheme oxidation, in particular the absorbance decreases at 554 nm, 526 and 423 nm, with concomitant absorbance increase at 409 nm. Recall that when 4-electron reduced wild type was exposed to photogenerated NO heme II nitrosylation over tens of seconds was accompanied by concurrent partial oxidation of heme IV (Section 3.3.2). With F156A⁴⁻ nitrosylation after laser initiation occurs in ms, without attendant *c*-heme oxidation (component Λ_0 , Fig. 4.6a), and subsequent oxidation appears to be much slower, on the same timescale as observed for the wild type. The separation of the two processes can also be seen visually in Fig. 4.7, where the first ten SVD-cleaned spectra after the laser pulse

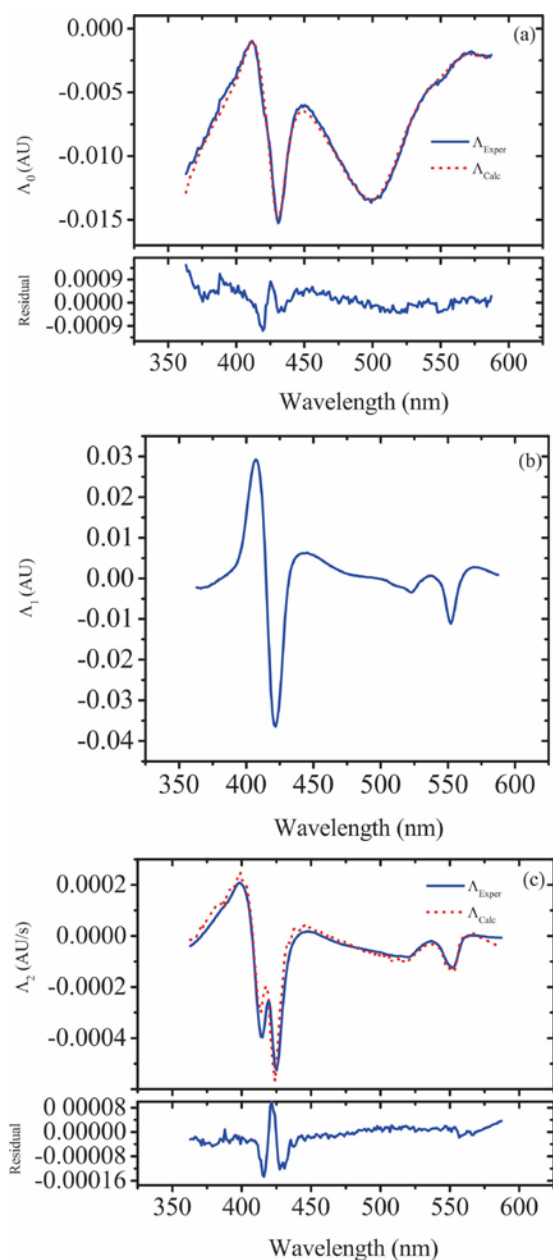


Figure 4.6. The spectral components Λ_0 - Λ_2 generated from the SVD-cleaned absorbance matrix when fit to Eq. 4.3 (blue traces). The red traces in (a) were fit with the known extinction coefficient of species **1** and the extinction coefficient difference spectrum of F156A²⁻(NO), obtained by analyzing nitrosylation of the 2-electron reduced protein. The red trace in (c) was fit with the F156A²⁻(NO) extinction coefficient difference spectrum, and admixtures of the $\Delta\epsilon_3$ and $\Delta\epsilon_4$ extinction coefficient difference spectra obtained for the low potential hemes III and IV of F156A by UV/Vis spectropotentiometry (Section 2.3.2).

were averaged to give the black trace, and the first 50 spectra were averaged and overlaid as the green trace. Both averaged spectra have more or less that same contributions from **1** photolysis (at ~500 nm) and from F156A⁴⁻ nitrosylation (at 432 and 414 nm), but in the longer average one can also begin to see appearance of the 554 band, and shifts in the Soret difference spectrum attributable to *c*-heme oxidation. To date, attempts to fit Λ_1 using extinction coefficient difference spectra obtained by UV/Vis spectropotentiometry (Chapter 2) have proved unsuccessful, presumably because heme II nitrosylation has changed the system to the point where the spectral components obtained from protein reduction in the absence of NO are no longer a sufficient basis. Why this is the case for component Λ_1 but not for Λ_2 is not yet clear.

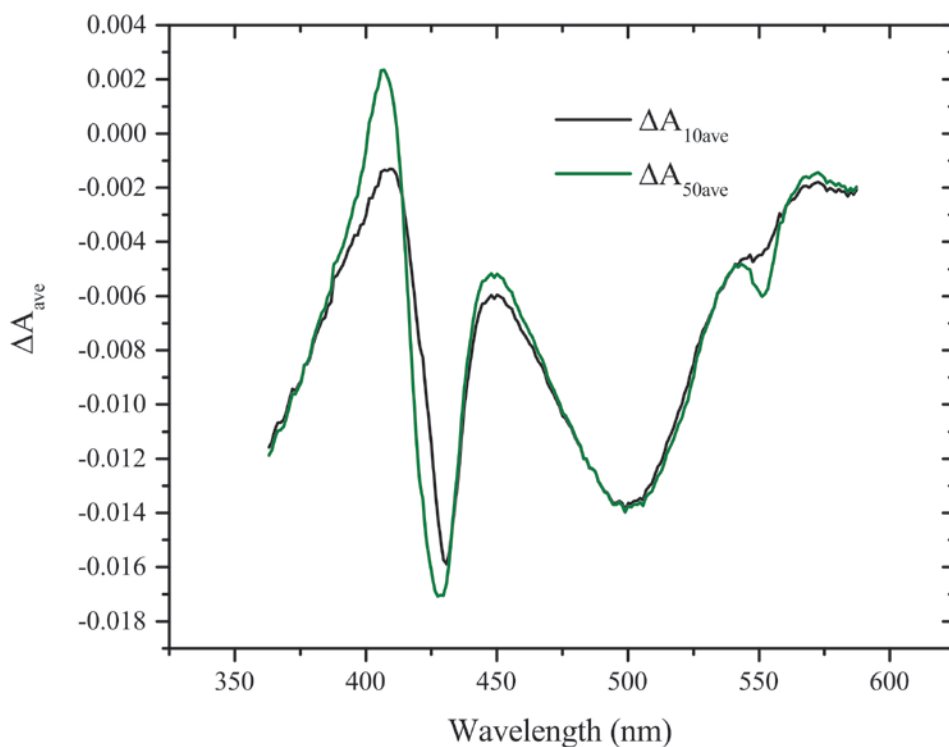


Figure 4.7. Plot of the first 10 (black trace) and first 50 (green trace) averaged SVD-cleaned spectra after the laser pulse from experiment shown in Fig 4.5a

4.4. Discussion

4.4.1. The reaction of photo-generated NO with two-electron reduced F156A.

Mutating the bulky hydrophobic amino acid Phe(156) to a smaller but still hydrophobic alanine profoundly increased the NO binding affinity (Scheme 4.1) of the 2-electron reduced mutant relative to wild type C₅₅₄. Thus, the equilibrium constant K_{eq} for NO binding went from $(9 \pm 2) \times 10^4 \text{ M}^{-1}$ for the wild type to $(4 \pm 2) \times 10^7 \text{ M}^{-1}$ for F156A²⁻. This is understandable given that Phe(156) sits right over the vacant site of heme II, restricting access to it (Fig. 1.5).

Interestingly, the increased NO affinity is due almost exclusively to an increase in k_{on} (Scheme 4.1), from $3000 \pm 140 \text{ M}^{-1}\text{s}^{-1}$ in the wild type to $(1.23 \pm 0.09) \times 10^6 \text{ M}^{-1}\text{s}^{-1}$ in F156A. The new rate constant is now within an order of magnitude of the k_{on} values typical of ferrous heme proteins such as myoglobin ($1.7 \times 10^7 \text{ M}^{-1}\text{s}^{-1}$) or hemoglobin ($2.5 \times 10^7 \text{ M}^{-1}\text{s}^{-1}$).¹⁴⁻¹⁶ On the other hand the rate constant for NO dissociation, k_{off} , remains virtually unchanged in F156A²⁻(NO) ($\sim 0.05 \text{ s}^{-1}$) relative to that of the wild type C₅₅₄²⁻(NO) ($0.034 \pm 0.009 \text{ s}^{-1}$). It appears that the less crowded pocket in F156A allows NO to more easily access and bind heme II, but that the bulky phenylalanine doesn't significantly destabilize the Fe-NO bond once the NO has bound metal.

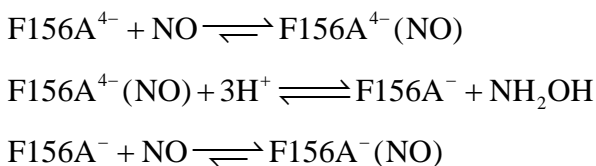
We had originally speculated that NO bound to the crowded pocket in wild type C₅₅₄ might be forced to adopt a Fe-N-O bond angle more bent than is ideal in $\{\text{Fe}(\text{NO})\}^7$ species, and that this would weaken the Fe-NO bond. The results presented herein suggest otherwise, though in the absence of structural data on the mutant we can't rule out the possibility that the Fe-N-O bond in F156A is still distorted, but by Thr 154 and Pro 155, which also crowd the heme II vacant site (Fig. 1.5). The k_{off} values of both wild type and F156A are both quite high compared to those of most ferroheme proteins, and even to those of synthetic water-soluble proteins, which

tend to fall in the range $10^{-4} - 10^{-5} \text{ s}^{-1}$.¹³⁻¹⁶ This might be due to the hydrophobic character of the C₅₅₄ pocket, where the bound NO would have no opportunity for stabilization by H-bonding from neighboring amino acids. However, k_{off} for NO from Fe^{II}(TPP) (TPP = tetraphenylporphyrin) in toluene has been measured at $4.17 \times 10^{-5} \text{ s}^{-1}$, though other synthetic porphyrin complexes denitrosylate with rate constants as high as 47 s^{-1} in toluene.¹⁶ These results suggest that the factors governing the C₅₅₄ k_{off} value may be complex, and will require further investigation.

4.4.2. The reaction of photo-generated NO with four-electron reduced F156A. As was seen for wild type C₅₅₄⁴⁻, exposure of F156A⁴⁻ to photogenerated NO results in heme oxidation as well as heme II nitrosylation. However, there are important differences between the two cases. First, the nitrosylation rate observed for F156A⁴⁻ was much faster than that observed for the wild type, yet the rate of heme oxidation was comparable. Second, the extent of heme oxidation that followed exposure to NO was substantially greater for the mutant. In the case of C₅₅₄⁴⁻ wild type it was estimated that about 40% of the low-potential heme IV was oxidized at the same time as heme II was being nitrosylated (Sections 3.3.2 and 3.4.2). Efforts to quantify the extent of *c*-heme oxidation after F156A⁴⁻ nitrosylation have thus far been thwarted, because we haven't been able to fit one of the spectra associated with the oxidation events (spectrum Λ_2 , Fig. 4.6b). Nevertheless, it is clear from a visual comparison of Figs. 3.6 and 4.6 that the extent of *c*-heme oxidation is substantially greater for the mutant.

Scheme 4.3 suggests a possible minimal mechanism that could explain the observed results. According to this mechanism, the initial rapid heme II nitrosylation is followed by a series of intramolecular electron transfers (IETs) from ferrohemes IV, III and I to the Fe_{II}-NO

moiety. Each IET event would be fast but unfavorable on its own, but would be coupled to a slow protonation of the bound NO that would drive the reaction forward. After three successive proton-coupled IETs NH₂OH would be released, leaving the protein in a 1-electron reduced state (F156A⁻). This species would then bind NO to once again leave heme II in an {Fe(NO)}⁷ state. According to this mechanism, the difference in reactivity between the wild type and F156A mutant would be explained as follows. First, substitution of Phe by Ala would open up the heme II region to allow more facile access for protons. Second, the heme III and IV midpoint potentials are substantially lower than those of the wild type (Table 2.2), making heme III in particular a stronger electron donor. Though in F156A²⁻ heme I will not reduce nitrosylated heme II, it might effect the final reduction that would allow free NH₂OH to be released; in that case the overall reaction would likely be driven forward by the final re-nitrosylation of heme II in Scheme 4.3.



Scheme 4.3

4.5. Summary

Heme II of the 2- or 4-electron reduced F156A C₅₅₄ mutant has an affinity for NO that is about 400× higher than heme II in the wild type, a difference that is almost exclusively due to a greater *k_{on}* association rate constant. As was the case for C₅₅₄²⁻, the 2-electron reduced F156A mutant will not oxidize in the presence of photogenerated NO. However, rapid nitrosylation of F156A⁴⁻ heme II is followed by substantial oxidation of the remaining C₅₅₄ low-spin hemes,

whereas in the case of wild type C₅₅₄⁴⁻ only partial oxidation of the lowest potential heme IV accompanied heme II nitrosylation. Scheme 4.3 provides a possible minimal mechanistic scheme to rationalize the results, but in future this will have to be backed up with more detailed studies. EPR studies of reactive intermediates, and mass spectrometric analysis of the reaction products, should be particularly useful in this regard.

4.6. References

- [1] Kostera, J., Youngblut, M. D., Slosarczyk, J. M., and Pacheco, A. A. (2008) Kinetic and product distribution analysis of NO reductase activity in *Nitrosomonas europaea* hydroxylamine oxidoreductase, *J. Biol. Inorg. Chem.* 13, 1073-1083.
- [2] Kostera, J., McGarry, J. M., and Pacheco, A. A. (2010) Enzymatic Interconversion of Ammonia and Nitrite: the Right Tool for the Job, *Biochemistry* 49, 8546-8553.
- [3] Wanat, A., Schnepensieper, T., Karocki, A., Stochel, G., and van Eldik, R. (2002) Thermodynamics and kinetics of Ru^{III}(edta) as an efficient scavenger for nitric oxide in aqueous solution, *J. Chem. Soc. Dalton Trans.*, 941-950.
- [4] Chatterjee, D., Mitra, A., Sengupta, A., Saha, P., and Chatterjee, M. (2006) [Ru^{III}(medtra)(H₂O)] (medtra = *N*-methylethylenediaminetriacetate) complex - a highly efficient NO inhibitor with low toxicity, *Inorg. Chim. Acta* 359, 2285-2290.
- [5] Drago, R. S., and Paulik, F. E. (1960) The Reaction of Nitrogen (II) Oxide with Diethylamine, *J. Am. Chem. Soc.* 82, 96-98.
- [6] Maragos, C. M., Morley, D., Wink, D. A., Dunams, T. M., Saavedra, J. E., Hoffman, A., Bove, A. A., Isaac, L., Hrabie, J. A., and Keefer, L. K. (1991) Complexes of NO with Nucleophiles as Agents for the Controlled Biological Release of Nitric-Oxide - Vasorelaxant Effects, *J. Med. Chem.* 34, 3242-3247.

- [7] Purwar, N., McGarry, J. M., Kostera, J., Pacheco, A. A., and Schmidt, M. (2011) Interaction of nitric oxide with catalase: structural and kinetic analysis, *Biochemistry* 50, 4491-4503.
- [8] Cabail, M. Z., Moua, V., Bae, E., Meyer, A., and Pacheco, A. A. (2007) Quantifying the photoinduced release of nitric oxide from N,N'-bis(carboxymethyl)-N,N'-dinitroso-1,4-phenylenediamine. Effect of reducing agents on the mechanism of the photoinduced reactions, *J. Phys. Chem. A* 111, 1207-1213.
- [9] Youngblut, M., Judd, E. T., Srajer, V., Sayyed, B., Goelzer, T., Elliott, S. J., Schmidt, M., and Pacheco, A. A. (2012) Laue crystal structure of *Shewanella oneidensis* cytochrome *c* nitrite reductase from a high-yield expression system, *J. Biol. Inorg. Chem.* 17, 647-662.
- [10] Koebke, K. J., Pauly, D. J., Lerner, L., Liu, X., and Pacheco, A. A. (2013) Does the oxidation of nitric oxide by oxyMyoglobin share an intermediate with the metMyoglobin-catalyzed isomerization of peroxynitrite?, *Inorg. Chem.* 52, 7623-7632.
- [11] Youngblut, M., Pauly, D. J., Stein, N., Walters, D., Conrad, J. A., Moran, G. R., Bennett, B., and Pacheco, A. A. (2014) *Shewanella oneidensis* cytochrome *c* nitrite reductase (ccNiR) does not disproportionate hydroxylamine to ammonia and nitrite, despite a strongly favorable driving force., *Biochemistry* 53, 2136-2144.
- [12] Koebke, K. J., Waletzko, M. T., and Pacheco, A. A. (2016) Direct monitoring of the reaction between photochemically generated nitric oxide and *Mycobacterium tuberculosis* truncated hemoglobin N wild type and variant forms: an assessment of theoretical mechanistic predictions., *Biochemistry* 55, 686-696.
- [13] Laverman, L. E., Wanat, A., Oszejca, J., Stochel, G., Ford, P. C., and van Eldik, R. (2001) Mechanistic studies on the reversible binding of nitric oxide to metmyoglobin, *J. Am. Chem. Soc.* 123, 285-293.

- [14] Hoshino, M., Ozawa, K., Seki, H., and Ford, P. C. (1993) Photochemistry of Nitric-Oxide Adducts of Water-Soluble Iron(III) Porphyrin and Ferrihemoproteins Studied by Nanosecond Laser Photolysis, *J. Am. Chem. Soc.* *115*, 9568-9575.
- [15] Ford, P. C., and Lorkovic, I. M. (2002) Mechanistic aspects of the reactions of nitric oxide with transition-metal complexes, *Chem. Rev.* *102*, 993-1017.
- [16] Wolak, M., and van Eldik, R. (2002) To be or not to be NO in coordination chemistry? A mechanistic approach, *Coord. Chem. Rev.* *230*, 263-282.

Chapter 5

The reaction of the cytochrome *c*₅₅₄ mutant F156H, at various stages of reduction, with photo-generated nitric oxide

5.1. Introduction

The analysis from Chapter 3 showed that 2-electron reduced C₅₅₄ will bind NO but not reduce it, while the 4-electron reduced protein will partially reduce bound NO by transferring an electron from its lowest potential heme. The results from Chapter 4 showed that the 2-electron reduced C₅₅₄ mutant F156A nitrosylates about 400× more rapidly than the wild type in the presence of excess NO, but bound NO is still not reduced, even in the presence of excess reducing agent. On the other hand, the low-spin hemes of 4-electron reduced F156A were oxidized in the presence of excess NO in the span of several minutes. The F156A mutation opened up more space in the vicinity of the heme II vacant site, but left the pocket environment hydrophobic and devoid of protonatable amino acids. This chapter looks at the consequences of replacing Phe 156 with the nearly equally bulky, but protonatable, histidine.

5.2. Materials and Methods

5.2.1. General materials. The provenance of the common chemicals used in this chapter's experiments was as summarized in Chapters 1 – 4.

5.2.2. General instrumentation. The instrumentation available for routine measurements was previously described in Chapters 1 – 4.

5.2.3. Protein handling. The construction of the F156H expression system, as well as the purification protocol for the mutant, were described in Chapter 2. Solutions of partially

reduced F156H were prepared by bulk electrolysis approximately as described in Chapter 3, except that for many experiments the dyes indigo carmine or indigo tetrasulfonate were used in place of hexaammineruthenium(III/II) as electrochemical mediators. The midpoint potential of heme II in the F156H mutant is much lower than that of the wild type (Table 2.2), so the more powerful electron donors (Table 2.1) were required to reduce it. Solutions with F156H at the desired stage of reduction were thus prepared by bulk electrolysis in the presence of the mediator most appropriate for the required applied potential. Subsequent experiments were performed by mixing the reduced protein solution with solutions containing either the NO photoprecursor **1**, or NO generated from DEANO as described in Section 4.2.3. In order to maximize anaerobicity, both solutions of **1** and solutions of DEANO-generated NO were made up in buffers containing the same electrolytically-reduced mediators as were present in the corresponding F156H stock solution. The next paragraph briefly summarizes the specific steps used to make up stock solutions for each type of experiment.

To obtain one electron reduced F156H for experiments with NO coming from DEANO decomposition, a stock solution of 10 mM hexaammine-ruthenium(III) chloride was prepared in 50 mM HEPES, 150 mM NaCl buffer at pH 7.0. For bulk electrolysis this solution was diluted to 200 μ M with the same buffer, and then used to reduce 1 μ M F156H by applying a potential of -50 mV vs SHE. In order to obtain two-electron reduced F156H for similar experiments, a saturated stock solution of indigo carmine was first prepared in 50 mM HEPES, 150 mM NaCl buffer at pH 7.0, and filtered using a 0.22 μ m syringe filter. The actual indigo carmine concentration was then determined to be 0.8 mM by UV/Vis spectroscopy, using the independently known extinction coefficient spectrum of indigo carmine. For bulk electrolysis, the filtered indigo carmine stock was diluted to 30 μ M and mixed with F156H in 50 mM Hepes,

150 mM NaCl buffer at pH 7.0, giving a final solution that contained 1 μM F156H. This solution was reduced by applying a potential of -150 mV vs SHE. In both cases above the contents of the bulk electrolysis cells were directly mixed with sufficient decomposed DEANO stock solution to give 40 μM NO concentrations for the experiments.

Two sets of photochemical experiments were performed with species **1** as NO precursor. One-electron reduced F156H was first generated by mixing in a bulk electrolysis cell 25 μM potassium indigo tetrasulfonate and oxidized protein stock, then applying a potential of -70 mV vs SHE. Species **1** stock was prepared independently by dissolving a minimal amount of the solid in 25 μM potassium indigo tetrasulfonate, pre-reduced by bulk electrolysis at an applied potential of -70 mV vs SHE, in standard HEPES buffer with 150 mM NaCl. The solutions for the laser experiments were made by mixing the one-electron reduced F156H with the solution of **1** in the reduced indigo tetrasulfonate buffer. Four-electron reduced F156H for laser-initiated time resolved spectroscopy was prepared as described in Chapter 3, whereby Zn powder was the reducing agent, and 3 μM methyl viologen acted as a mediator.

In all experiments the concentrations of F156H, as well as the extent of the protein's reduction, were assessed by UV/Vis spectroscopy using the independently obtained extinction coefficient spectra of the protein at various stages of reduction (see Chapter 2).

5.2.4. Experiments with DEANO-generated NO. Samples with one and two-electron reduced F156H were prepared in the glovebox, in 1 cm pathlength quartz cuvettes (Starna). Spectral changes that followed exposure to NO were monitored with a Cary 50 spectrophotometer (Varian).

5.2.5. Laser-initiated time-resolved spectroscopic experiments. Samples for laser-initiated time-resolved experiments were prepared in the glovebox and data were collected with the Olis RSM-1000 spectrophotometer in rapid-scanning average mode 1, as described in Chapter 3.

5.2.6. Data analysis. Data analysis strategies were similar to those used in Chapters 3 and 4, as described in more detail below.

5.3. Results

5.3.1. Net reaction of NO with two-electron reduced F156H. Figure 5.1 shows the spectral changes seen upon mixing a solution initially containing 1 μM F156H electrochemically reduced with 30 μM indigo carmine with 40 μM nitric oxide. The black trace in panel (a) shows the protein spectrum in the absence of NO, and the red one shows the effect of adding NO. Figure 5.1b shows the difference spectrum obtained by subtracting the black trace from the red.

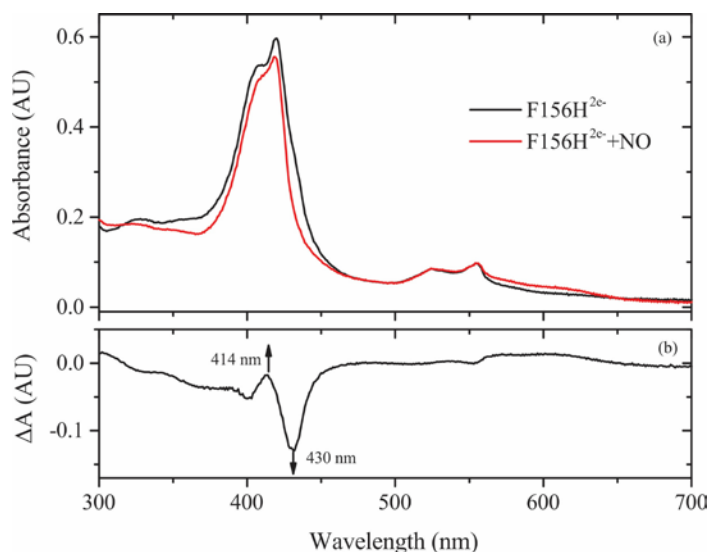


Figure 5.1. (a) Black trace: spectrum of 1 μM F156H reduced by two electrons with 30 μM indigo carmine; red trace: after the two-electron reduced F156H is exposed to 40 μM NO. (b) The difference spectrum obtained by subtracting the black trace from the red trace from (a).

The solution was reduced by applying a potential of -150 mV vs SHE, and under these conditions the two higher potential hemes of F156H (hemes I and II) are reduced, while the low potential hemes (III and IV) remain mostly oxidized (see Table 2.2). The Fig. 5.1b difference spectrum gives the peaks characteristic of heme II nitrosylation seen for wild type and F156A (Chapters 2 and 3): an absorbance decrease at 430 nm, and an increase at 414 nm.

5.3.2. Net reaction of NO with one-electron reduced F156H. Figure 5.2 shows the spectral changes seen upon mixing a solution initially containing 1 μM F156H electrochemically reduced with 200 μM $\text{Ru}(\text{NH}_3)_6^{2+}$ with 40 μM nitric oxide. The black trace in panel (a) shows the protein spectrum in the absence of NO, and the red one shows the effect of adding NO. Figure 5.2b shows the difference spectrum obtained by subtracting the black trace from the red. The solution was reduced by applying a potential of -50 mV vs SHE, which would only be low

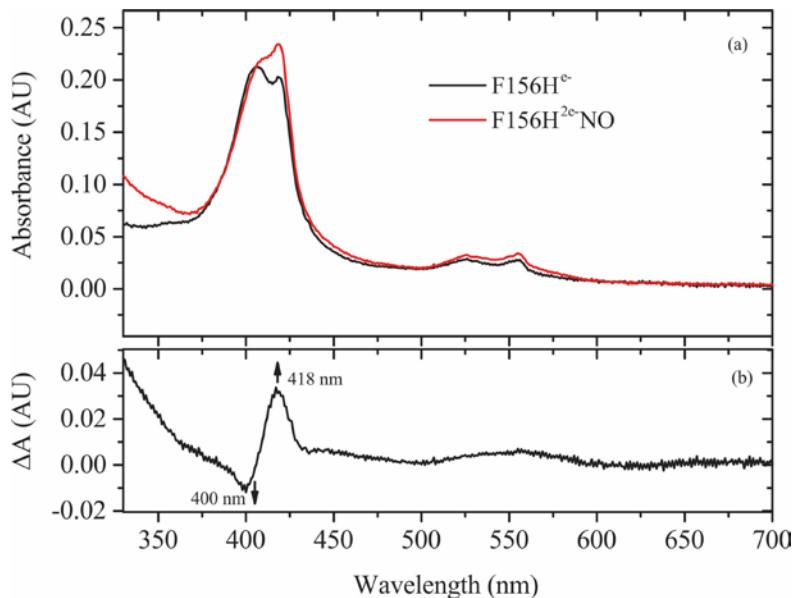
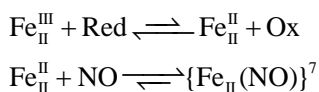


Figure 5.2. (a) Black trace: spectrum of 1 μM F156H reduced by one electron with 200 μM $\text{Ru}(\text{NH}_3)_6^{2+}$; red trace: after the one-electron reduced F156H is exposed to 40 μM NO. (b) The difference spectrum obtained by subtracting the black trace from the red trace from (a).

enough to reduce heme I in F156H (see Table 2.2). Now the Fig. 5.2b difference spectrum shows an absorbance decrease at 400 nm and an increase at 418 nm. The decrease at 400 nm would normally be taken as evidence of c-heme reduction; however, no concomitant absorbance increase is seen at 554 nm, meaning that the oxidation states of the low-spin hemes I, III and IV remain unchanged. We therefore attribute the observed difference spectrum to simultaneous reduction and nitrosylation of heme II, by the process outlined in Scheme 5.1. This scheme allows for partial reduction of heme II by the mediator even at -50 mV vs SHE, as represented by the equilibrium in the first step. This equilibrium will lie well to the left; however, if ferrous heme II binds NO to make an $\{\text{Fe}(\text{NO})\}^7$ species (second step in Scheme 5.1), that is expected to shift its midpoint potential dramatically higher,¹ thus shifting the equilibrium to the right.



Scheme 5.1. Red is the reducing agent present in excess, $\text{Ru}(\text{NH}_3)_6^{2+}$ or reduced indigo tetrasulfonate.

5.3.3. The reaction of photo-generated NO with one-electron reduced F156H. Figure 5.3 shows the spectral changes observed after a solution initially containing $25 \mu\text{M}$ indigo tetrasulfonate reduced at -0.07 mV vs SHE, $5 \mu\text{M}$ F156H and 0.3 mM NO generating species **1** was irradiated with a 5 ns, 500 nm laser pulse, which fragments **1** to give NO (scheme 3.1). The raw time-resolved UV/vis spectra were first subjected to singular value decomposition (SVD) to determine the number of spectral components and smooth out noise.^{2,3} The SVD analysis showed that only three components were needed to faithfully reconstruct a noise-reduced absorbance matrix. The SVD-treated data were fit to Eq. 5.1 using a global fitting routine.

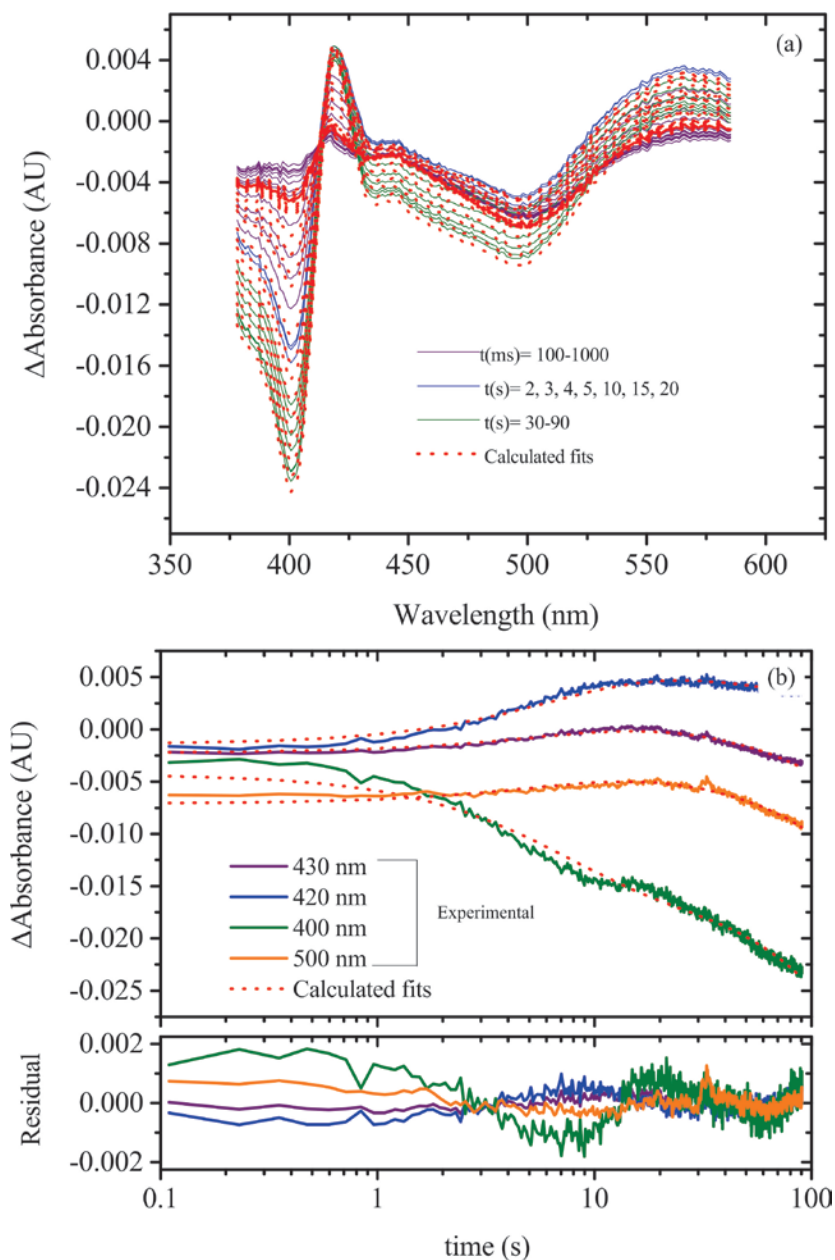


Figure 5.3. (a) Spectral changes observed when a solution initially containing 0.3 mM of the NO generating species **1**, 5 μ M F156H and 25 μ M indigo tetrasulfonate reduced at a potential of -70 mV vs SHE, was exposed to a 500 nm, 5 ns laser pulse which fragments **1** to release NO. The purple traces are representative of the first second, the blue traces are taken at 1-s intervals, and the green ones at 10-s intervals. The red traces are the least-squares best fits using Eq. 5.1. (b) Changes in absorbance vs time at the representative wavelengths stated, with the least-squares best fits using Eq. 5.1 overlaid as red traces.

$$\Delta A_{\lambda,t} = \Lambda_{0(\lambda)} + \Lambda_{1(\lambda)}(1 - e^{-k_{obs}t}) + \Lambda_{2(\lambda)}t \quad (5.1)$$

Equation 5.1 is the same as Eqs. 3.1 and 4.3. It has a component present at t_0 , one that grows in exponentially, and a third that grows in linearly. The fitting routine was the same as that described in Chapter 3.

Figure 5.4 shows the spectral components obtained from the fitting process. The

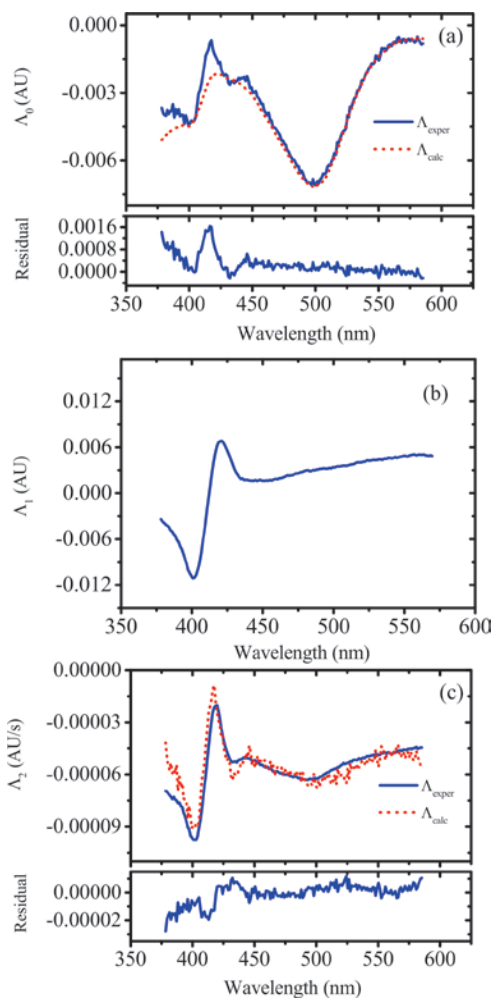


Figure 5.4 The spectral components Λ_0 - Λ_2 generated from the SVD-cleaned absorbance matrix when fit to Eq. 5.1 (blue traces). The red traces in (a) were fit with the known extinction coefficient of species **1**. The red trace in (c) was fit with the known extinction coefficient spectra of species **1** and admixtures of Λ_0 and Λ_1 .

component Λ_0 (Figure 5.5a) arises from the denitrosylation of species **1** within the deadtime of the experiment. This component can be fit with the known extinction coefficient spectrum of species **1** to determine the amount of NO generated by the laser pulse. For Fig. 5.4a the fit revealed that 30 μM NO were generated in the experiment shown. The component Λ_1 (Figure 5.4b) grows in exponentially with a k_{obs} of 0.151 s^{-1} , and is attributed to reduction of the 5-coordinate heme II of F156H as heme II is nitrosylated, as discussed in Section 5.3.2 (scheme 5.1). Finally, component Λ_2 (Figure 5.4c) grows in linearly, and arises from the release of NO from species **1** caused by the spectrophotometer probe beam irradiation during the experiment, as seen in Chapters 3 and 4. The Λ_2 component was fit using the independently known extinction coefficient spectrum of species **1**, with an admixture of component Λ_1 .

5.3.4. The reaction of photo-generated NO with four-electron reduced F156H.

Figure 5.5 shows the spectral changes observed after a solution initially containing 3 μM F156H, 0.1 mM of the NO generating species **1** (Scheme 3.1), and 3 μM of methyl viologen reduced by zinc powder (see Section 5.2.3), was exposed to a 500 nm, 5 ns laser pulse, which fragments **1** to release NO (Scheme 3.1). Under these conditions all of the F156H hemes are initially reduced. SVD analysis of the data showed that three components were needed to faithfully reconstruct a noise-reduced absorbance matrix. As with the 1-electron reduced data, the SVD-treated data of Fig. 5.5 could be fit to Eq. 5.1 (red traces, Fig. 5.5).

Figure 5.6 shows the spectral components obtained from the fitting process. As with the 1-electron reduced case, the component Λ_0 (Fig. 5.6a) arises from the denitrosylation of species **1** within the deadtime of the experiment, and could be fit with the known extinction coefficient spectrum of species **1**. This revealed the amount of NO generated by the laser pulse to be 10 μM . The component Λ_2 (Fig 5.6c) that grows in linearly is once again attributed primarily to the

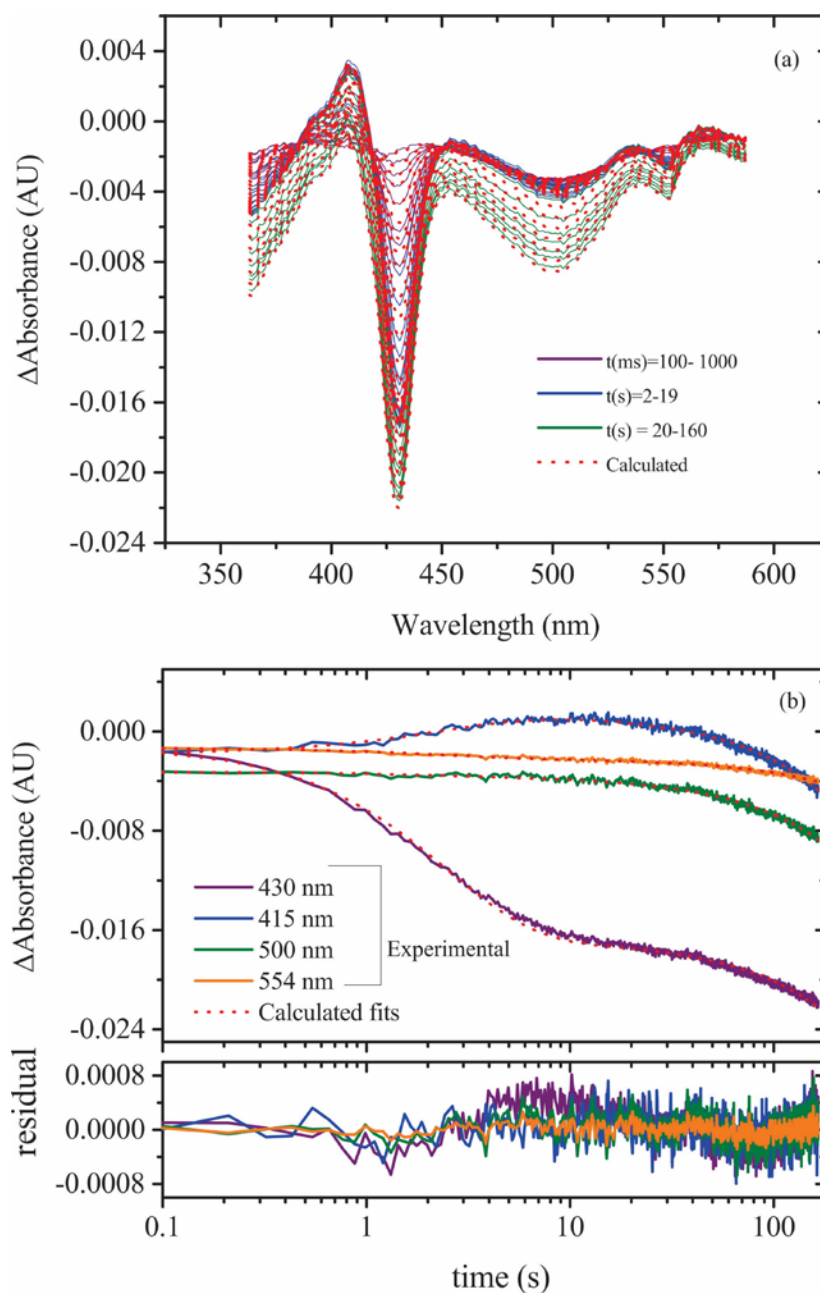


Figure 5.5. (a) Spectral changes observed when a solution initially containing 0.1 mM of the NO generating species **1**, 3 μM F156H and 3 μM of Zn-reduced methyl viologen was exposed to a 500 nm, 5 ns laser pulse which fragments **1** to release NO. The purple traces are representative of the first second, the blue traces are taken at 1-s intervals, and the green ones at 20-s intervals. The red traces are the least-squares best fits using Eq. 5.1. (b) Changes in absorbance vs time at the representative wavelengths stated, with the least-squares best fits using Eq. 5.1 overlaid as red traces.

spectrophotometer probe-beam induced nitric oxide release from species **1**., though the negative features at 554 nm and 425 nm indicate that a slow low-spin ferroheme oxidation is also taking place. The final component Λ_1 (Fig. 5.6b), which grows in exponentially with a k_{obs} of 0.5 s^{-1} ,

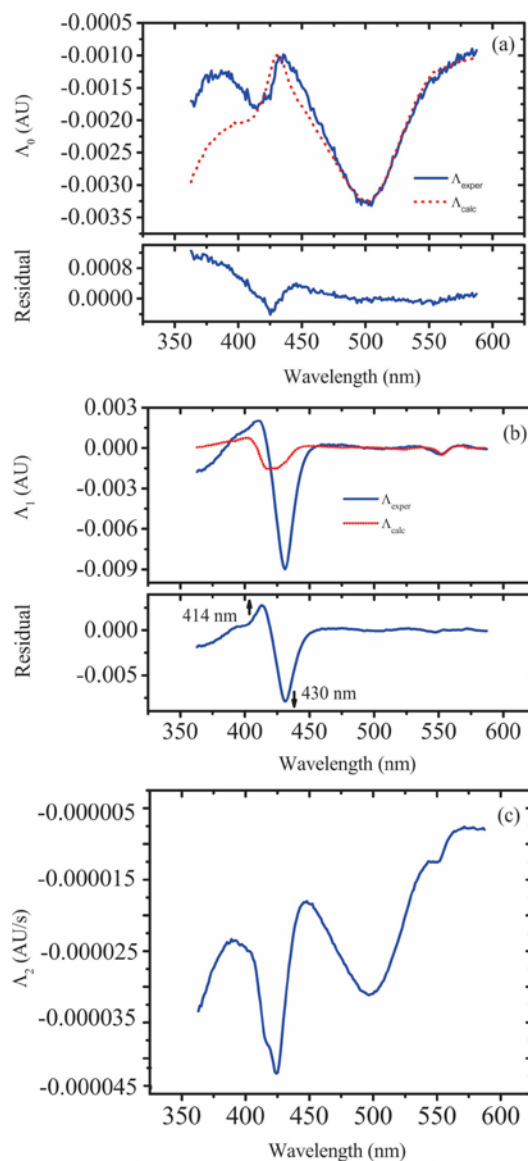


Figure 5.6. The spectral components Λ_0 - Λ_2 generated from the SVD-cleaned absorbance matrix when fit to Eq 5.1 (blue traces). The red trace in (a) is a fit with the known extinction coefficient of species **1**. The red trace in (b) is a fit with 4-3 electron reduced extinction coefficient spectrum obtained by UV/Vis spectropotentiometry (Chapter 2).

exhibits features characteristic of changes at the F156H *c* hemes that are reminiscent of those seen after exposure of 4-electron reduced wild type C₅₅₄ to NO (Chapter 3). As with the wild type, subtraction of a contribution from a small amount of heme IV oxidation (~0.11 μM), determined by zeroing out the 554 signal, left behind the signals at 414 and 430 nm characteristic of heme II nitrosylation (Fig. 5.6b).

5.4. Discussion

5.4.1. The reaction of NO with one and two-electron reduced F156H. The Chapter 2 analysis showed that the F156H heme II midpoint potential is shifted dramatically to the negative (to -111 mV) compared to the heme II midpoint potentials of wild type C₅₅₄ and the F156A mutant. This made it more challenging to find a reducing agent that could poise F156H in its two-electron reduced form for laser experiments, but wouldn't react directly with NO. Fortunately, the indigo dyes were found to react only slowly with NO, and indigo carmine has low enough potential to reduce F156H by two electrons. Solutions of two-electron reduced F156H mixed with DEANO show evidence of heme II nitrosylation only, with a characteristic increase at 415 nm and decrease at 430 nm in the UV/Vis spectrum.

Laser experiments to obtain kinetics were still complicated by the slow reaction of the indigo dyes with NO. For example, in the experiment with one-electron reduced F156H (Figs. 5.3, 5.4) the Soret region of component Λ_1 is nicely fit with reduction of heme II, but the region where indigo tetrasulfonate absorbs (500-600 nm) shows a change that is not readily fit with the known extinction coefficient spectra of the oxidized and reduced dye. This may be due to an additional interaction of the dye with NO. Notably, though spectral changes in the Soret region that accompanied nitrosylation of the 1-electron reduced protein were characteristic of heme

reduction, there was no accompanying change at 554 nm that is characteristic of low spin heme reducing. We attribute the aggregate spectral changes to concomitant heme II nitrosylation and reduction, and it appears that reduced and nitrosylated heme II does not exhibit the characteristic peak at 554 nm. When 2-electron reduced F156H is nitrosylated, the spectral change is completely analogous to that seen for wild type and F156A nitrosylation (Fig. 5.1).

A k_{obs} was obtained from the laser-initiated nitrosylation experiments with one-electron reduced F156H. This rate constant was attributed to coupled nitrosylation and reduction of heme II as shown in Scheme 5.1. It is in the same order of magnitude as the nitrosylation rate obtained for 2-electron reduced wild type C₅₅₄, showing that NO access to the active site is hindered to a comparable extent. Future studies will be needed to establish the dependence of k_{obs} on [NO] but we expect this dependence to be very comparable to that seen in the wild type.

5.4.2. The reaction of photo-generated NO with four-electron reduced F156H. The interaction of NO with four-electron reduced F156H gives results comparable to those seen in the wild type experiments (Chapter 3), though notably the rate constant obtained for F156H (0.5 s^{-1}) is much higher for the amount of NO produced by the laser pulse ($10 \text{ }\mu\text{M}$) than was seen for the wild type. Thus, for 2-electron reduced wild type C₅₅₄ the k_{obs} seen at the highest amount of NO tested ($110 \text{ }\mu\text{M}$, Fig. 3.3) was 0.35 s^{-1} , while the rate constant obtained when four-electron reduced wild type was exposed to $66 \text{ }\mu\text{M}$ NO was 0.097 s^{-1} . At present, we can't explain the unusually fast nitrosylation rate, but it may point to a role in His156 stabilizing a bound NO^- , possibly through hydrogen bonding. More complete studies will be needed in future to determine histidine's role in increasing k_{obs} .

5.5. Summary

Heme II of F156H²⁻ and F156H⁴⁻ is seen to have similar reactivity with NO as wild type C₅₅₄. As with wild type, two-electron reduced F156H will not oxidize upon exposure of photogenerated NO. Interestingly, when F156H is poised in a one-electron reduced state and exposed to NO, the nitrosylation of heme II is coupled to its reduction. Further investigation of F156H⁴⁻ interaction with NO will be needed to explain the higher nitrosylation rate constant observed for the mutant. EPR and pH-dependence studies of F156H and its reduced forms, with and without NO, should be particularly valuable in future investigations of this C₅₅₄ variant.

5.6. References

- [1] Stein, N. (2014) Spectroscopic and electrochemical studies of shewanella oneidensis cytochrome c nitrite reductase, and improving c-heme expression systems, In *Department of Chemistry and Biochemistry*, University of Wisconsin-Milwaukee.
- [2] Press, W. H., Teukolsky, S. A., Vetterling, W. T., and Flannery, B. P. (2007) Numerical Recipes the art of scientific computing, 3rd ed., pp 65-75, Cambridge University Press, New York, NY.
- [3] Henry, E. R., and Hofrichter, J. (1992) Singular Value Decomposition: Application to Analysis of Experimental Data, In *Meth. Enzymol.* (Brand, L., and Johnson, M. L., Eds.), pp 129-192, Academic Press, San Diego.

Chapter 6

Conclusions and suggestions for further study

A re-investigation of the interaction of C₅₅₄ with NO has shown that the 5-coordinate heme II of the 2-electron or 4-electron reduced protein will nitrosylate reversibly. The nitrosylation process is first order in C₅₅₄, first-order in NO, and second-order overall. The rate constant for NO binding to the heme was determined to be $3000 \pm 140 \text{ M}^{-1}\text{s}^{-1}$, while the rate constant for dissociation was $0.034 \pm 0.009 \text{ s}^{-1}$; the degree of protein reduction does not appear to significantly influence the nitrosylation rate. In contrast to a previous report, [Upadhyay, A. et al. (2006), *J. Am. Chem. Soc.* 128, 4330-4337] this study turned up no evidence of C₅₅₄-catalyzed NO reduction, either with C₅₅₄²⁻ or with C₅₅₄⁴⁻. Some sub-stoichiometric oxidation of the lowest potential heme IV is detected when C₅₅₄⁴⁻ is exposed to an excess of photogenerated NO, and this could in principle be part of a process that yields N₂O, though alternative explanations are equally plausible, as discussed in Chapter 3. Further studies will be needed to test for N₂O formation directly.

The vacant heme II site of C₅₅₄ is sterically crowded by three non-bonding hydrophobic amino acids, Thr 154, Pro 155 and Phe 156. Replacing Phe156 with a protonatable but still bulky histidine residue did not significantly alter the reactivity of the F156H mutant with NO, though the binding rate appears to increase 10-fold. On the other hand, when Phe156 was replaced with the smaller but still hydrophobic alanine, the 6-coordinate low-spin hemes of the 4-electron reduced mutant oxidized over the course of several minutes after exposure to NO. Two-electron reduced F156A²⁻ nitrosylated, but did not oxidize, upon exposure to NO. Notably, the nitrosylation rate for F156A²⁻ and F156A⁴⁻ was about 400× faster than for the wild type or

for the F156H mutant, though the rate of the reverse denitrosylation process was almost the same for the three C₅₅₄ variants.

The midpoint potentials of C₅₅₄, and of the F156A and F156H variants, were determined for all the hemes in these tetraheme proteins, using spectropotentiometric analysis. The heme II midpoint potential of F156H was profoundly altered from the wild type value, shifting about 170 mV to the negative. This is taken as evidence that the histidine ligand in the variant binds to the erstwhile vacant ferric heme II, thus stabilizing the oxidized state. Consistent with this interpretation, the UV/Visible spectrum of fully oxidized F156H has increased absorbance at 409 nm relative to the wild type, which suggests that the protein now has 4 low-spin ferrihemes, rather than three low-spin and one high-spin as seen in the wild type. Upon reduction of heme II though, the spectrum of F156H exhibits a band at 430 nm characteristic of high-spin ferrohemes, which suggests that His 156 dissociates from the heme when this reduces.

In contrast to the case with F156H, the midpoint potentials of hemes I and II in F156A are only slightly shifted relative to the wild type. On the other hand, the midpoint potentials of the low-potential hemes III and IV are shifted about 100 mV to the negative by mutating Phe156 to Ala, whereas mutation of Phe156 to His has minimal impact on these hemes. It appears that the substitution of bulky Phe by the small Ala significantly alters the conformation of the protein backbone, which in turn affects the environment of distant hemes enough to substantially alter their midpoint potentials. The lower heme III and IV midpoint potentials of F156A, together with the increased solvent access to the heme II vacant site in this variant, may work together in changing its reactivity to bound NO. The more strongly reducing hemes could more readily reduce bound NO, while increased solvent access could now allow protonation to accompany reduction of the bound nitrogen moiety.

While C₅₅₄ itself is now shown not to catalyze NO reduction, the experiments with the F156A and F156H mutants show that this protein could be a useful model system for determining the minimal requirements of an NO reducing catalyst. Thus, opening up the vacant heme II site in F156A appears to make the 4-electron reduced protein competent to reduce bound NO, which in addition binds to the protein much more rapidly. Changing Phe156 to His did not appreciably change F156H's reactivity towards NO in the experiments tried so far; however, to accelerate NO reduction a histidine would probably have to be protonated in order to facilitate coupled proton-electron transfer. Thus, an obvious future experiment should be to determine the His pKa in F156H, and then investigate the reactivity of F156H with NO as a function of applied pH.

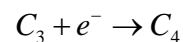
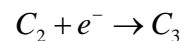
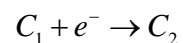
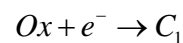
In addition to studying the pH-dependence of the C₅₄₄ wild type and variant reactions with NO, future studies should focus first on characterizing the various oxidation states of F156A and F156H by EPR and possibly Mossbauer. EPR in particular would be an excellent technique for testing whether or not heme II of F156H is in fact coordinated by histidine as it appears to be from the evidence so far, and also for determining the order of reduction of hemes III and IV in F156A, where this order may have been switched. EPR would also be valuable for determining the nature of the Fe-NO bond in the various nitrosylated species generated for C₅₅₄ and its variants at various stages of reduction. Finally, some methodologies such as GC/mass spectrometry will need to be developed to directly measure what, if any reduced nitrogen species are released when F156A⁴⁻ is exposed to NO.

Appendix 1

Supplementary Material for Chapter 2

A1.1. Spectropotentiometric analysis for a generic four heme system

A1.1.1. Derivation of Equation 2.8. This derivation is analogous to that described in reference 1. Using the terminology presented in Scheme A1.1, we can write the Nernst equations that relate two given heme species C_n and C_{n-1} , as shown in Eqs. A1.1-A1.4.



Scheme A1.1.

$$\varepsilon_{app} = \varepsilon_1^o - \frac{RT}{nF} \ln \frac{C_1}{Ox} \quad (A1.1)$$

$$\varepsilon_{app} = \varepsilon_2^o - \frac{RT}{nF} \ln \frac{C_2}{C_1} \quad (A1.2)$$

$$\varepsilon_{app} = \varepsilon_3^o - \frac{RT}{nF} \ln \frac{C_3}{C_2} \quad (A1.3)$$

$$\varepsilon_{app} = \varepsilon_4^o - \frac{RT}{nF} \ln \frac{C_4}{C_3} \quad (A1.4)$$

In exponential form these equations can be re-written as shown in Equations A1.5 and A1.6,

$$C_1 = Ox \times E_1 \quad (A1.5)$$

$$C_n = C_{n-1} \times E_n \quad (A1.6)$$

where E_n is defined by Equation 2.1c from Chapter 2:

$$E_n = \exp\left[\frac{nF}{RT}(\varepsilon_n^o - \varepsilon_{app})\right] \quad (2.1c)$$

The total concentration of protein, C_T , is defined by the sum of the various species present at any given applied potential (Eq. A1.7). All of the species except Ox can be eliminated from Eq. A1.7 by substituting each C_n value with the expressions A1.5, and A1.6. The result is shown in Equation A1.8.

$$C_T = Ox + \sum_{n=1}^4 C_n \quad (A1.7)$$

$$C_T = Ox\{1 + E_1[1 + E_2[1 + E_3(1 + E_4)]]\} \quad (A1.8)$$

Solving for Ox gives Eq. A1.9, where the term in the denominator has been abbreviated as “*denom*” (Eq. 2.8b from Chapter 2). Finally, by performing successive substitutions into Eqs. A1.5 and A1.6, the C_n species can be rewritten in terms of C_T , as shown in Eq. 2.1a of Chapter 2.

$$Ox = \frac{C_T}{denom} \quad (A1.9)$$

$$denom = 1 + E_1\{1 + E_2[1 + E_3(1 + E_4)]\} \quad (2.8b)$$

$$C_n = \frac{C_T \times \prod E_n}{denom} \quad (2.8a)$$

A1.1.2. Beer’s law for difference spectra. Equation A1.10 gives the Beer’s law expression for a tetraheme system in which each additional added electron results in a distinct spectral change. By solving for Ox in Eq. A1.7 (which yields Eq. A1.11), this term can be eliminated from the Beer’s law expression to give Eq. A1.12. In Eqs A1.10 – A1.12 A_λ is the

$$A_\lambda = \left\{ \varepsilon_{ox\lambda} Ox + \sum_{n=1}^4 \varepsilon_{n\lambda} C_n \right\} \times \ell \quad (\text{A1.10})$$

$$Ox = C_T - \sum_{n=1}^4 C_n \quad (\text{A1.11})$$

$$A_\lambda = \left\{ \varepsilon_{ox\lambda} \left[C_T - \sum_{n=1}^4 C_n \right] + \sum_{n=1}^4 \varepsilon_{n\lambda} C_n \right\} \times \ell \quad (\text{A1.12})$$

absorbance at a given wavelength λ , $\varepsilon_{ox\lambda}$ and $\varepsilon_{n\lambda}$ are the extinction coefficients of the oxidized and n^{th} reduced species at that wavelength, and ℓ is the cell pathlength. In the absence of applied potential the protein is in the fully oxidized form, and Eq. A1.12 simplifies to Eq. A1.13, where $A_{0\lambda}$ is the absorbance of fully oxidized protein at λ . Using Eq. A1.13 to substitute for $\varepsilon_{ox\lambda} C_T$ in Eq. A1.12 we get, after rearrangement, Eq. A1.14. Rearrangement of the summations then yields the desired Eq. A1.15, in which $\Delta A_\lambda = A_\lambda - A_{0\lambda}$ and $\Delta \varepsilon_{n\lambda} = \varepsilon_{n\lambda} - \varepsilon_{ox\lambda}$. Equation 2.9 is analogous to Eq. A1.15, except for a slight modification in notation that emphasizes the

$$A_{0\lambda} = \varepsilon_{ox\lambda} C_T \ell \quad (\text{A1.13})$$

$$A_\lambda = \left(A_{0\lambda} - \varepsilon_{ox\lambda} \sum_{n=1}^4 C_n + \sum_{n=1}^4 \varepsilon_{n\lambda} C_n \right) \times \ell \quad (\text{A1.14})$$

$$\Delta A_\lambda = \ell \times \sum_{n=1}^4 \Delta \varepsilon_{n\lambda} C_n \quad (\text{A1.15})$$

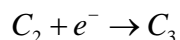
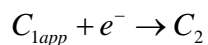
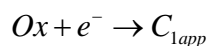
dependence of C_n on the applied potential.

Equations 2.4 – 2.7, which were used to analyze the F156A data, could be readily derived in a manner analogous to the one described in this section. Derivation of expressions to describe the wild type C₅₅₄'s behavior upon reduction required a somewhat different approach, as described in the following section.

A1.2. Special case: wild type C₅₅₄

A1.2.1. Derivation of the Nernstian equations in exponential form. Although C₅₅₄ has four hemes, SVD analysis^{2,3} of the wild type UV/Vis spectra obtained in spectropotentiometric titrations showed that these are linear combinations of just two component spectra (Chapter 2). This result can be attributed to two causes. The first is that the two high potential hemes have identical midpoint potentials, so they reduce simultaneously. This leads to spectral changes that are indistinguishable from those that would accompany one-electron reduction of a single heme. The second factor that reduces the number of components is that the two low potential hemes make identically-shaped contributions to the extinction coefficient difference spectra of the 3- and 4-electron reduced C₅₅₄ species. Thus, although the third and fourth reduction events require two Nernstians to model them, they give rise to a single spectral component. The simultaneous reduction of the two high-potential hemes is tackled in this section, while the reduction of the two low-potential hemes is confronted in Section A1.2.2 below.

To account for the fact that the two high-potential hemes reduce simultaneously, and generate spectral changes that are indistinguishable from those that would accompany one-electron reduction of a single heme, we replace Scheme A1.1 from Section A1.1.1 with Scheme A1.2. In this scheme C_{1app} is the concentration of what appears to be a 1-electron reduced C₅₅₄ species that accumulates as the applied potential is lowered, but is in fact a 2-electron reduced



Scheme A1.2

species. Overall, the reduction of C_{554} appears to take place in three 1-electron Nernstian steps, as summarized in Scheme A1.2. The corresponding Nernstian equations in exponential form are Eqs. 2.1 from Chapter 2. These are completely analogous to Eqs. 2.8, except that there appear to

$$C_n = \frac{C_T \times \prod E_n}{denom} \quad (2.1a)$$

$$denom = 1 + E_1[1 + E_2(1 + E_3)] \quad (2.1b)$$

be only three reduced species, the first being C_{1app} .

A1.2.2. Beer's law for difference spectra. We begin by defining $\Delta\epsilon_{HP}$ as the extinction coefficient difference spectrum of the two high-potential hemes combined, so that the spectral contribution of these hemes to the total absorbance change at a given wavelength and applied potential will be given by Eq. A1.16, where the value of C_{1app} is specified by Eq. 2.1. If we now

$$\Delta A_{1(\lambda)} = \Delta\epsilon_{HP(\lambda)} \cdot C_{1app} \cdot \ell \quad (A1.16)$$

assume that the two low-potential hemes make identically-shaped contributions to the extinction coefficient difference spectra of the apparently 2- and 3-electron reduced species C_2 and C_3 , we can define $\Delta\epsilon_{LP}$ as the extinction coefficient difference spectrum of the two low-potential hemes combined. With this definition, Eqs. A1.17 and A1.18 give the spectral contributions

$$\Delta A_{2(\lambda)} = (\Delta\epsilon_{HP(\lambda)} + 0.5\Delta\epsilon_{LP(\lambda)}) \cdot C_2 \cdot \ell \quad (A1.17)$$

$$\Delta A_{3(\lambda)} = (\Delta\epsilon_{HP(\lambda)} + \Delta\epsilon_{LP(\lambda)}) \cdot C_3 \cdot \ell \quad (A1.18)$$

attributable to the second and third reduction events, respectively. Equation A1.17 takes into account the fact that the two high-potential hemes contribute to the spectrum of the apparent 2-electron reduced species, and the next heme to reduce will contribute half of the total for the two low-potential hemes. The two high-potential hemes similarly contribute to the spectrum of the

apparent 3-electron reduced C₅₅₄, and the lowest potential heme contributes the second half of the total for the low-potential hemes (Eq. A1.18). The observed absorbance change at a given wavelength and applied potential will be the sum of the contributions from the

$$\begin{aligned} \Delta A_{\lambda} &= \Delta A_{1\lambda} + \Delta A_{2\lambda} + \Delta A_{3\lambda} \\ &= \left[\Delta \varepsilon_{HP(\lambda)} \cdot C_{1app} + (\Delta \varepsilon_{HP(\lambda)} + 0.5 \cdot \Delta \varepsilon_{LP(\lambda)}) \cdot C_2 + (\Delta \varepsilon_{HP(\lambda)} + \Delta \varepsilon_{LP(\lambda)}) \cdot C_3 \right] \cdot \ell \end{aligned} \quad (\text{A1.19})$$

1-, 2-, and 3-electron reduced species present in solution, as shown in Eq. A1.19. This equation can be rearranged to Eq. 2.2, used to fit the data in Chapter 2.

$$\Delta A_{\lambda} = \left[\Delta \varepsilon_{HP(\lambda)} \cdot (C_{1app} + C_2 + C_3) + \Delta \varepsilon_{LP(\lambda)} (0.5C_2 + C_3) \right] \cdot \ell \quad \text{Eq. 2.2}$$

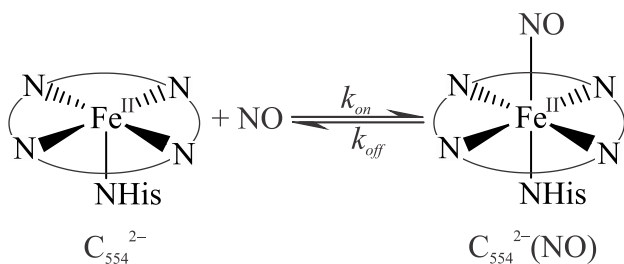
A1.3. References

- [1] Youngblut, M., Judd, E. T., Srajer, V., Sayyed, B., Goelzer, T., Elliott, S. J., Schmidt, M., and Pacheco, A. A. (2012) Laue crystal structure of *Shewanella oneidensis* cytochrome *c* nitrite reductase from a high-yield expression system, *J. Biol. Inorg. Chem.* 17, 647-662.
- [2] Press, W. H., Teukolsky, S. A., Vetterling, W. T., and Flannery, B. P. (2007) Numerical Recipes the art of scientific computing, 3rd ed., pp 65-75, Cambridge University Press, New York, NY.
- [3] Henry, E. R., and Hofrichter, J. (1992) Singular Value Decomposition: Application to Analysis of Experimental Data, In *Meth. Enzymol.* (Brand, L., and Johnson, M. L., Eds.), pp 129-192, Academic Press, San Diego.

Appendix 2

Supplementary Material for Chapter 3

A2.1 Derivation of rate law for C5542- nitrosylation



Scheme 3.2.

$$\frac{d[C_{554}^{2-}NO]}{dt} = k_{on}[NO][C_{554}^{2-}] - k_{off}[C_{554}^{2-}NO] \quad (\text{A2.1})$$

At time t,

$$C_T = C_{554}^{2-} + [C_{554}^{2-}NO] \quad (\text{A2.2})$$

Substitute A2.2 into A2.1,

$$\frac{d[C_{554}^{2-}NO]}{dt} = k_{on}[NO](C_T - [C_{554}^{2-}NO]) - k_{off}[C_{554}^{2-}NO] \quad (\text{A2.3})$$

Rearrange A2.3,

$$\frac{d[C_{554}^{2-}NO]}{dt} = k_{on}[NO]C_T - (k_{on}[NO] + k_{off})[C_{554}^{2-}NO] \quad (\text{A2.4})$$

In these experiments, we set up pseudo first order conditions:

$[NO] \gg [C_{554}NO]$ total generated during the reaction.

So, $[NO]$ will not vary significantly during the reaction.

Define,

$$A = k_{on}[NO]C_T \quad (\text{constant under pseudo first order conditions}) \quad (\text{A2.5})$$

$$k_{obs} = k_{on}[NO] + k_{off} \quad (\text{constant under pseudo first order conditions}) \quad (\text{A2.6})$$

Note that Eq. A2.6 is Eq. 3.2 of main text.

$$\frac{d[C_{554}^{2-}NO]}{dt} = A - k_{obs}[C_{554}^{2-}NO] \quad (\text{A2.7})$$

Rearrange A2.7,

$$\frac{d[C_{554}^{2-}NO]}{A - k_{obs}[C_{554}^{2-}NO]} = dt \quad (\text{A2.8})$$

Integrate A2.8,

$$\int_{[C_{554}^{2-}NO]=0}^{[C_{554}^{2-}NO]} \frac{d[C_{554}^{2-}NO]}{A - k_{obs}[C_{554}^{2-}NO]} = \int_{t=0}^t dt \quad (\text{A2.9})$$

Solve using substitution (page 138),

$$-\frac{1}{k_{obs}} \left[\ln \left(A - k_{obs} [C_{554}^{2-} NO] \right) \right]_0^{[C_{554}^{2-} NO] = t]_0^t} = t \quad (A2.10)$$

Rearrange A2.10,

$$\ln \left(A - k_{obs} [C_{554}^{2-} NO] \right) - \ln A = -k_{obs} t \quad (A2.11)$$

$$\ln \frac{A - k_{obs} [C_{554}^{2-} NO]}{A} = -k_{obs} t \quad (A2.12)$$

$$\frac{A - k_{obs} [C_{554}^{2-} NO]}{A} = e^{-k_{obs} t} \quad (A2.13)$$

$$[C_{554}^{2-} NO] = \frac{A}{k_{obs}} \left(1 - e^{-k_{obs} t} \right) \quad (A2.14)$$

Substitute for A and k_{obs} in the pre-exponential term of A2.14,

$$[C_{554}^{2-} NO] = \frac{k_{on} [NO] C_T}{k_{on} [NO] + k_{off}} \left(1 - e^{-k_{obs} t} \right) \quad (A2.15)$$

Rearrange A2.15,

$$[C_{554}^{2-} NO] = \frac{C_T [NO]}{[NO] + \frac{k_{off}}{k_{on}}} \left(1 - e^{-k_{obs} t} \right) \quad (A2.16a)$$

This is the characteristic exponential equation for a species, here $C_{554}^{2-}NO$ approaching equilibrium. The expression can be written more compactly as follows:

$$[C_{554}^{2-}NO] = Amp(1 - e^{-k_{obs}t}) \quad (A2.16b)$$

Where,

$$Amp = \frac{C_T[NO]}{K_{eq}^{-1} + [NO]} \quad (A2.16c)$$

And,

$$K_{eq}^{-1} = \left(\frac{k_{off}}{k_{on}} \right) \quad (A2.16d)$$

$$k_{obs} = k_{on}[NO] + k_{off} \quad (A2.6)$$

Equation A2.16 can be expressed in terms of absorbance changes using the Beer' law relationship outlined in Appendix 1.

As a reminder of freshman calculus, the integral of A2.9 can be solved by method of substitution as follows:

$$\int \frac{d[C_{554}^{2-}NO]}{A - k_{obs}[C_{554}^{2-}NO]} \quad (A2.9)$$

Start by defining u as,

$$u = A - k_{obs}[C_{554}^{2-}NO]$$

Differentiate u with respect to $C_{554}^{2-}NO$,

$$\frac{du}{d[C_{554}^{2-}NO]} = -k_{obs}$$

Rearrange,

$$d[C_{554}^{2-}NO] = -\frac{du}{-k_{obs}}$$

Now the entire integral can be expressed in terms of u,

$$-\frac{1}{k_{obs}} \int \frac{du}{u}$$

This readily integrates to,

$$= -\frac{1}{k_{obs}} \ln u$$

Back-substitute for u to obtain the integral for the original expression,

$$= -\frac{1}{k_{obs}} \ln(A - k_{obs}[C_{554}^{2-}NO]) \tag{A2.10}$$

A2.2 Derivation of ϵ^0_{cell} for Scheme 3.3

$\Delta\epsilon_{LP}$ corresponds to two low potential hemes changing oxidation state.

$\Delta A = \Delta\epsilon_{LP} \cdot C_T \cdot \text{Frac}$ Frac is the fraction of low potential heme pool oxidized

C_T is the total C_{554} concentration

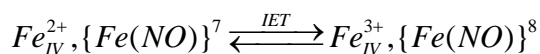
For example, when Frac = 0.5, half of the low-potential heme pool has been reduced, equivalent to one low-potential heme.

In the laser experiment for Section 3.4.2,

$$\frac{\Delta A}{\Delta \epsilon_{LP}} = C_T \cdot frac = 0.8 \times 10^{-6} \text{ M}$$

Where Frac = 0.2, 20 percent of two low-potential hemes are oxidized therefore, 40 percent of first low-potential heme is oxidized where $C_T = 4 \times 10^{-6} \text{ M}$

From Scheme 3.3,



Fit from Figure 3.6d gives,

$$Fe_{IV}^{2+}, \{Fe(NO)\}^7 \quad 60 \% \text{ of } 4.6 \times 10^{-6} = 2.4 \times 10^{-6} \text{ M}$$

$$Fe_{IV}^{3+}, \{Fe(NO)\}^8 \quad 40 \% \text{ of } 4.6 \times 10^{-6} = 1.6 \times 10^{-6} \text{ M}$$

Equilibrium for Scheme 3.3,

$$K_{IET} = \frac{Fe_{IV}^{3+}, \{Fe(NO)\}^8}{Fe_{IV}^{2+}, \{Fe(NO)\}^7} = 0.67$$

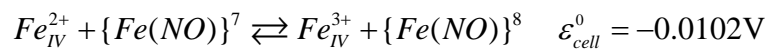
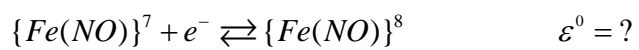
Equilibrium can be related to the ϵ_{cell}^0 for Scheme 3.3,

$$\Delta G = -RT \ln K = -nF \epsilon_{cell}^0$$

Substituting K_{IET} value for Scheme 3.3 into above equation gives,

$$\epsilon_{cell}^0 = \frac{RT}{nF} \ln K = \frac{RT}{nF} \ln 0.67 = -0.0102 \text{ V}$$

Determine the ϵ^0 value for the equilibrium between $\{Fe(NO)\}^7$ and $\{Fe(NO)\}^8$



Solve for ϵ^0

$$\epsilon^0 = -0.260V$$

**Jennifer McGarry
Curriculum Vitae**

Contact Information

2824 North Pierce St.
Milwaukee, WI 53212
414-232-6274
jmcgarry@uwm.edu

Current Position

**Research assistant for Dr. A. Andrew Pacheco in the
Department of Chemistry and Biochemistry at the
University of Wisconsin-Milwaukee**

2009-2017

Education

University of Wisconsin-Milwaukee, Ph.D. Chemistry
August 2017
University of Wisconsin-Milwaukee, B.Sc. Chemistry
2009

Publications

McGarry, J. M.; Van Roo, J; Pacheco, A. A. "Selective binding of nitric oxide by 2- and 4-electron reduced cytochrome *c*₅₅₄ yields a stable protein-ligand complex" In preparation.

McGarry J. M.; Pacheco, A. A. "Perturbing the midpoint potentials and nitric oxide binding properties of cytochrome *c*₅₅₄ via site directed mutagenesis" In preparation.

Purwar, N.; McGarry, J. M.; Kostera, J.; Pacheco, A. A.; Schmidt, M. (2011) "Interaction of nitric oxide with catalase: structural and kinetic analysis" *Biochemistry* 50, 4491-4503.

Pacheco, A. A.; McGarry, J. M.; Kostera, J.; Corona, A. (2011) "Techniques for investigating hydroxylamine disproportionation by hydroxylamine oxidoreductases" *Meth. Enzymol.* 286, 447-463.

Kostera, J.; McGarry, J. M.; Pacheco, A. A. (2010) "Enzymatic interconversion of ammonia and nitrite: the right tool for the job" *Biochemistry* 49, 8546-8553.

Selected Presentations

Jennifer McGarry, A. Andrew Pacheco. "Electrochemical properties of cytochrome *c*₅₅₄

and active site mutants” Fifth Latin American Meeting on Biological Inorganic Chemistry, October 18th-22th 2016, Queretaro, Mexico.

Jennifer McGarry, A. Andrew Pacheco. “Electrochemical properties of cytochrome *c₅₅₄* and active site mutants” Chemistry and Biochemistry Research Symposium, May 21th 2016, University of Wisconsin-Milwaukee, Milwaukee, Wisconsin.

Jennifer McGarry, A. Andrew Pacheco. “The interaction of nitric oxide with cytochrome *c₅₅₄* from *Nitrosomonas europaea*” Metals in Biology Gordon Research Conference, January 25th - 30th 2015, Ventura, California.

Jennifer McGarry, A. Andrew Pacheco. “The interaction of nitric oxide with cytochrome *c₅₅₄* from *Nitrosomonas europaea*” Biophysics Seminar, September 18th 2014, University of Wisconsin-Milwaukee, Milwaukee, Wisconsin.

Jennifer McGarry, A. Andrew Pacheco. “Probing intermediates in ammonia-nitrite interconversion” Chemistry and Biochemistry Research Symposium, April 19th 2013, University of Wisconsin-Milwaukee, Milwaukee, Wisconsin.

Jennifer McGarry, Matthew D. Youngblut, A. Andrew Pacheco. “Kinetic investigation of cytochrome *c₅₅₄* nitrosylation” 15th International Conference on Biological Inorganic Chemistry, August 7th - 12th 2011, University of British Columbia, Vancouver, B. C. Canada.

Jennifer McGarry, Josh Kostera, A. Andrew Pacheco. “Enzymatic interconversion of ammonia and nitrite: the right tool for the job” Chemistry and Biochemistry Research Symposium, April 9th 2010, University of Wisconsin-Milwaukee, Wisconsin.

Biochemistry/Molecular biology experience

Bacterial growth. Extensive experience in growing multiple types of bacteria on small and large scales (up to 100 Liter cultures).

Bacterial cloning/Over-expression systems. Highly proficient in current techniques used for cloning in Gram-negative bacteria. Substantial experience with site-directed mutagenesis. Have designed expression systems for difficult target proteins. Have cloned/overexpressed proteins in the atypical bacterium *Shewanella oneidensis*.

Protein purification. Proficient in protein purification using AKTA FPLC and LPLC with ion exchange, hydrophobic interaction, size exclusion and affinity columns.

Anaerobic techniques. Highly proficient in the use of anaerobic gloveboxes and inert gas Schlenk lines.

Protein Assays. Experienced in optimizing protein assays under aerobic and anaerobic conditions.

Data Analysis/Instrumentation experience

UV/visible spectroscopy. Highly proficient in time-resolved UV/visible spectroscopy experiments using conventional and stopped-flow mixing, as well as nanosecond laser-pulsed initiation.

Time-resolved nanosecond laser-initiated spectroscopy. Substantial experience in using nanosecond pulsed lasers for photo-initiated reactions in protein solutions. Extensive experience in developing methods for poisoning the applied potential in a protein solution for subsequent study of partially reduced proteins with photo-generated substrates. Significant experience aligning laser optics.

Stopped-flow UV/visible spectroscopy. Considerable experience with double mixing stopped flow initiation under anaerobic conditions. Experience with sample preparation in a glovebox and on an inert gas Schlenk line.

Electrochemistry. Proficient in performing spectropotentiometric titrations of proteins with multiple redox-active sites, and analyzing the results. Some experience with performing and interpreting cyclic voltammetry experiments.

Data Analysis. Proficient at designing programs in PTC Mathcad, and using Microcal Origin, for analysis of large datasets.

Protein Crystallography. Have experience with growing protein crystals and collecting diffraction data at the APS facility of Argonne National Laboratory. Some experience analyzing protein diffraction data.

Synthesis

Inorganic synthesis. Some experience with inorganic synthesis under aerobic and anaerobic conditions.

Service, Education, Outreach

Have mentored to 1-5 undergraduate researchers per semester since spring of 2012.

Have mentored students who participated in the American Chemical Society's Project Seed program, which sponsors talented high school students from economically disadvantaged backgrounds to gain experience in a research laboratory for the summer.

Supervised teachers who participated in the NSF's Research Experience for Teachers program, which places K-12 science teachers in a research laboratory for the summer to learn techniques that can be applied in the classroom.